Karlsruhe Institute of Technology

Marc Hippler

3D Laser Lithography of Stimuli-Responsive Hydrogels

2020
Dissertation

3D Laser Lithography of Stimuli-Responsive Hydrogels

Zur Erlangung des akademischen Grades eines
Doktors der Naturwissenschaften
von der KIT-Fakultät für Physik des
Karlsruher Instituts für Technologie (KIT)

genehmigte

Dissertation

von

Marc Hippler, M. Sc.
geboren in Karlsruhe

Tag der mündlichen Prüfung: 06. November 2020
Referent: Prof. Dr. Martin Wegener
Korreferent: Prof. Dr. Martin Bastmeyer

Contents

Publications

Scientific Journals

Parts of this thesis have already been published in scientific journals:

- M. Hippler, K. Weißenbruch, K. Richler, E. D. Lemma, M. Nakahata, B. Richter, C. Barner-Kowollik, Y. Takashima, A. Harada, E. Blasco, M. Wegener, M. Tanaka, M. Bastmeyer, "Mechanical stimulation of single cells by reversible host-guest interactions in 3D microscaffolds", Science Advances **6**, eabc2648 (2020)
- C. A. Spiegel*, M. Hippler*, A. Münchinger*, M. Bastmeyer, C. Barner-Kowollik, M. Wegener, and E. Blasco, "4D Printing at the Microscale", Advanced Functional Materials **30**, 1907615 (2019)
- M. Hippler*, E. D. Lemma*, S. Bertels*, E. Blasco, C. Barner-Kowollik, M. Wegener, and M. Bastmeyer, "3D Scaffolds to Study Basic Cell Biology", Advanced Materials **31**, 1808110 (2019)
- M. Hippler, E. Blasco, J. Qu, M. Tanaka, C. Barner-Kowollik, M. Wegener, and M. Bastmeyer, "Controlling the shape of 3D microstructures by temperature and light", Nature Communications **10**, 232 (2019)

Scientific Conferences

Parts of this thesis have already been presented at scientific conferences (only own presentations):

- M. Hippler, E. Blasco, J. Qu, M. Tanaka, C. Barner-Kowollik, M. Wegener, and M. Bastmeyer, "Controlling the shape of 3D microstructures by temperature and light" (invited talk), 4D Printing and Metamaterials Conference (online conference), May 2020

*These authors contributed equally.

- M. Hippler, K. Weißenbruch, K. Richler, E. D. Lemma, M. Nakahata, B. Richter, C. Barner-Kowollik, Y. Takashima, A. Harada, E. Blasco, M. Wegener, M. Tanaka, and M. Bastmeyer, "Stimuli-responsive 3D micro-scaffolds for single cell actuation", SPIE Photonics West 2020, San Francisco, CA, USA, February 2020

- M. Hippler, E. Blasco, J. Qu, M. Tanaka, C. Barner-Kowollik, M. Wegener, and M. Bastmeyer, "Controlling the shape of 3D microstructures by temperature and light", SPIE Photonics West 2019, San Francisco, CA, USA, February 2019

Additional Publications

Additional related work has already been published:

- N. Silbernagel, A. Körner, J. Balitzki, M. Jaggy, S. Bertels, B. Richter, M. Hippler, A. Hellwig, M. Hecker, M. Bastmeyer, and N. D. Ullrich, "Shaping the heart: Structural and functional maturation of iPSC-cardiomyocytes in 3D-micro-scaffolds", Biomaterials **227**, 119551 (2020)

- S. Yu, B. Fritz, S. Johnsen, D. Busko, B. S. Richards, M. Hippler, G. Wiegand, Y. Tang, Z. Li, U. Lemmer, H. Hölscher, and G. Gomard, "Enhanced Photoluminescence in Quantum Dots–Porous Polymer Hybrid Films Fabricated by Microcellular Foaming", Advanced Optical Materials **7**, 1900223 (2019)

- L. Yang, X. Chen, L. Wang, Z. Hu, C. Xin, M. Hippler, W. Zhu, Y. Hu, J. Li, Y. Wang, L. Zhang, D. Wu, and J. Chu, "Targeted Single-Cell Therapeutics with Magnetic Tubular Micromotor by One-Step Exposure of Structured Femtosecond Optical Vortices", Advanced Functional Materials **29**, 1905745 (2019)

- R. Batchelor, T. Messer, M. Hippler, M. Wegener, C. Barner-Kowollik, and E. Blasco, "Two in One: Light as a Tool for 3D Printing and Erasing at the Microscale", Advanced Materials **31**, 1904085 (2019)

- M. Gernhardt, E. Blasco, M. Hippler, J. Blinco, M. Bastmeyer, M. Wegener, H. Frisch, and C. Barner-Kowollik, "Tailoring the Mechanical Properties of 3D Microstructures Using Visible Light Post-Manufacturing", Advanced Materials **31**, 1901269 (2019)

- S. F. Wondimu, M. Hippler, C. Hussal, A. Hofmann, S. Krämmer, J. Lahann, H. Kalt, W. Freude, and C. Koos, "Robust label-free biosensing using microdisk laser arrays with on-chip references", Optics Express **26**, 3161–3173 (2018)
- R. M. Dörlich, Q. Chen, P. Niklas Hedde, V. Schuster, M. Hippler, J. Wesslowski, G. Davidson, and G. U. Nienhaus, "Dual-color dual-focus line-scanning FCS for quantitative analysis of receptor-ligand interactions in living specimens", Scientific Reports **5**, 10149 (2015)

Chapter 1

1 Introduction

The famous biochemist and noble prize winner Alexander R. Todd summarized in 1980 that he is "*inclined to think that the development of polymerization is perhaps the biggest thing that chemistry has done, where it has had the biggest effect on everyday life*" [1]. Undoubtedly, polymers have been essential materials throughout human history. Although the term is often implicitly connected with synthetic materials, natural polymers like wool, cotton or rubber have been important goods for centuries. Natural biopolymers such as DNA and proteins, on the other hand, are essential for fundamental biological processes and structures. All these polymeric materials have in common that they consist of large macromolecules, which are composed of many repeating sub-units called monomers. Attempts in the chemical modification of polymers date back to the 19th century, likely driven by the economic rise of the rubber industry. Only in the early 20th century, however, researchers began to understand the nature and the structure of polymers which ultimately led to groundbreaking advances in the field known today as polymer chemistry. Since then, myriads of polymer classes have been developed for almost every conceivable application with an unmatched impact on today's life.

A comparatively new approach, which is getting more and more attention in recent decades, is based on the desire to mimic natural materials that can adapt to their environment. These polymers are capable of undergoing conformational or chemical changes upon external signals and are thus termed stimuli-responsive or smart polymers. Such stimuli arise either from changes in the materials' environment like temperature or the chemical surrounding, or can be triggered externally, e.g., by light irradiation or exposure to magnetic fields. Typical applications include sensors and biosensors [2], adaptive surfaces for biology [3] and textiles [4], and controlled drug delivery [5]. Another intriguing idea is to exploit the material response to create artificial

muscles or actuators with the ability to perform remote tasks. This aspect is especially interesting for biomedical sciences in aqueous environments. In this context, soft, hydrophilic polymers with a high water content called hydrogels are a natural choice.

Stimuli-responsive hydrogels have been successfully used in the past to realize soft actuators and devices which respond to external triggers. Here, optical fabrication techniques like UV mask lithography were typically used to structure the hydrogels in a spatially controlled photopolymerization reaction [6]. In recent years, however, the rise of 3D printing techniques such as stereo-lithography has literally opened a new dimension in the design of hydrogels [7]. With these advanced technologies, complex responsive hydrogel structures like actuators and grippers [8] or remote controlled robots with locomotion [9] have been realized. The majority of these examples, however, is still limited to the macroscopic regime and many promising applications that require structures on the micrometer scale remain inaccessible. This gap could be closed by 3D laser lithography, an emerging technique based on two-photon absorption to fabricate polymeric microstructures with sub-micron resolution.

Despite this potential, little research on stimuli-responsive hydrogel microstructures is available [10]. Prominent pioneering examples include a microcantilever which bends under illumination with UV light [11], swelling of asymmetric hydrogel structures as a function of NaCl concentration [12], and multi-material hydrogel pads which respond to changes in pH and temperature [13]. So far, however, the majority of published results are proof-of-concept experiments and clear prospects for applications are missing. Here, two major challenges might hinder a further breakthrough of this method. First, many applications require strong directed actuations which cannot be realized by an isotropic hydrogel swelling. In this context, microstructures with directed and robust responses could enable new routes in research fields like soft-robotics. The second major challenge is related to the bio-compatibility of the stimulation itself. Although the arguably most important application area is situated in the biomedical field, most materials require harsh conditions for the stimulation. Thus, new material systems with physiological stimuli are mandatory to facilitate the successful operation in biological environments. In the scope of this thesis, these pending challenges are tackled to enable new applications of stimuli-responsive hydrogel microstructures fabricated by 3D laser lithography.

Outline of this thesis

In chapter 2, I describe the necessary fundamentals to understand and discuss the results of this work. After introducing the basics of 3D laser lithography, I particularly focus on the specific challenges in the fabrication of stimuli-responsive hydrogels. In the last part of this chapter, I give a brief overview of mechanobiology in the context of the experiments performed in this work. Chapter 3 summarizes the experimental methods for the fabrication and characterization of the stimuli-responsive structures. Furthermore, I provide details on the performed numerical calculations with the finite element method and describe the protocols and workflows for all biological experiments.

Chapter 4 covers the results on temperature-responsive hydrogel microstructures exhibiting large, reversible actuations. After characterizing the material properties, I discuss a gray-tone lithography approach to fabricate bi-material structures from a single photoresist. The strong and directed response can either be triggered globally by temperature changes or locally by exposure with light. The results are complemented by numerical calculations to study the underlying mechanisms and predict the structure response based on the input design.

In chapter 5, I present stimuli-responsive microscaffolds based on novel supramolecular materials. After a general overview of the material response, the multi-material scaffolds are introduced and thoroughly characterized. Numerical calculations further provide a calibration of the microstructures in regard to forces and displacements. In the second part of the chapter, I show results of the application of these scaffolds to study the response of individual biological cells to mechanical stimulation. The experiments are quantitatively analyzed with a large number of cells and discussed in detail. I further describe inhibition and staining experiments to expose the role of myosin II motor proteins in the cellular force generation machinery.

Finally, I summarize and discuss the results of this thesis in chapter 6 and give a brief outlook.

Chapter 2

2 Fundamentals

In this chapter, I introduce the fundamental concepts which are necessary to understand the experiments presented in this thesis. I start with an introduction to 3D laser lithography with a special focus on the radical photopolymerization procedure, the two-photon absorption process, and the achievable resolution. Next, I comment on the fabrication of stimuli-responsive hydrogel microstructures with this technique and discuss the impact of different crosslinking mechanisms in such hydrogels in detail. In the last section, I summarize the basics of mechanobiology in the context of the experiments presented in chapter 5. I introduce the concept of the actin cytoskeleton with actin stress fibers and discuss non-muscle myosin class II motor proteins, which play a crucial role in the scope of this thesis.

2.1 3D Laser Lithography

3D laser lithography, also known as direct laser writing (DLW), is a versatile technique to fabricate 3D structures on the micro- and nanoscale [14, 15]. A femtosecond pulsed laser beam is tightly focused into a photoresist and starts a physical or chemical reaction inside the laser focus. By moving this focus relative to the sample, almost arbitrary 3D structures can be fabricated. As in conventional lithography techniques like UV-mask lithography, positive or negative tone photoresists can be used. In positive tone photoresists, illumination leads to changes in the chemical structure of the material which makes them soluble with an appropriate developer. As a consequence, all illuminated parts are removed during the development procedure. In contrast, negative tone photoresists are typically liquid and the illuminated parts become insoluble. Thus, regions exposed to the laser focus become solid and the remaining photoresist is washed away by application of the

solvent. In this thesis, we applied negative tone photoresists based on monomers and suitable photoinitators to absorb the light and start a radical polymerization reaction.

2.1.1 *Radical Photopolymerization*

Radical photopolymerization is the most common mechanism for negative-tone photoresists in DLW. Mono- and multifunctional monomers are mixed with radical photoinitiators which are chosen according to the excitation wavelength. Absorption of light by these initiators leads to cleavage and formation of radicals. These radicals are highly reactive and start chemical chain reactions, which eventually lead to the formation of a solid, insoluble polymer network. Typically, this process can be described in four stages [16], schematically depicted in Figure 2.1(a):

1. **Radical formation.** Light absorption by photoinitiators (I) leads to excitation of the molecules (I^*), and formation of reactive radical species ($R^\bullet$) by cleavage:

$$I \xrightarrow{h\nu} I^* \longrightarrow R^\bullet. \tag{2.1}$$

2. **Chain initiation.** The generated radical ($R^\bullet$) attacks a monomer (M) to form a monomer radical $RM^\bullet$. This complex acts as the starting point of a polymer chain:

$$R^\bullet + M \longrightarrow RM^\bullet. \tag{2.2}$$

3. **Chain propagation.** The monomer radical ($RM^\bullet$) attacks another monomer (M). This monomer is incorporated into the chain and can again attack further molecules:

$$RM^\bullet + M \longrightarrow RMM^\bullet. \tag{2.3}$$

   In this way, more and more monomers are added to form longer polymer chains:

$$RM_i^\bullet + M \longrightarrow RM_{i+1}^\bullet. \tag{2.4}$$

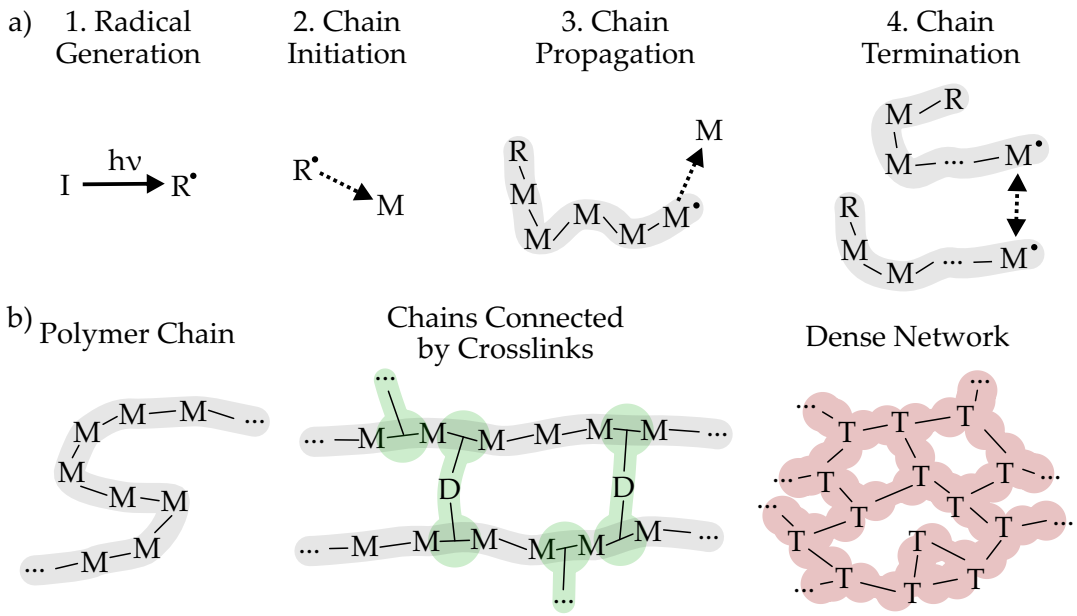

Figure 2.1: Schematic of a radical photopolymerization. (a) Four stages of a radical polymerization. Initiators (I) are cleaved to generate radicals ($R^\bullet$) which attack monomers (M) in the photoresist. These monomers in turn react with new monomers and a polymer chain propagates until two chains combine to a new single chain to terminate the process. (b) Schematics of a single polymer chain of monofunctional molecules (M), two chains connected by crosslinks with dual functionalities (D), and a dense polymer network formed by only tri-functional molecules (T).

4. **Chain termination.** A very common termination process of chain growth in DLW is the bimolecular termination . Two radically active polymer chains $RM_i^\bullet$ and $RM_j^\bullet$ combine to a single chain RM_{i+j} which is no longer able to to attack further monomers:

$$RM_i^\bullet + RM_j^\bullet \longrightarrow RM_{i+j}R. \tag{2.5}$$

Another process, which only becomes relevant for large initiator concentrations and high light intensities, is the primary termination. Here, radical polymer chains ($RM_i^\bullet$) combine with free radicals ($R^\bullet$) to terminate the chain growth:

$$RM_i^\bullet + R^\bullet \longrightarrow RM_iR. \tag{2.6}$$

After the polymer chains reach a certain length, they are no longer soluble in the developer in contrast to the small monomers in the unexposed parts of the photoresist. In the simple scheme above, however, individual polymer chains are independent from each other and although they become physically entangled, the mechanical stability of the resulting structures is typically low. For this reason, conventional photoresist systems in DLW use multifunctional monomers with more than one group that can be attacked by radicals. This leads to the formation of a dense and stable polymer network instead of separated chains. In case the photoresist contains special mono-functional monomers, it is also possible to mix them with multifunctional monomers (often called crosslinkers in this context) to connect the polymer chains with each other. Typical examples are schematically depicted in Figure 2.1(b).

2.1.2 *Two-Photon Absorption*

The unique characteristic of DLW is the nonlinear absorption process which enables the fabrication of complex 3D structures. Although certain underlying processes in the photoresist during the reaction are not yet fully understood [17, 18], most experimentally observed effects can be well explained based on the threshold model and the accumulation model [19].

The threshold model states that polymer networks are washed away during the development procedure if their crosslinking density is lower than a certain gelation threshold. As a consequence, structures are only formed if the exposure dose $D(z)$ is equal or larger than a threshold dose D_{thresh}. On the other hand, all parts of the photoresist which are sufficiently exposed during the fabrication will withstand the development. Thus, introducing a fixed threshold basically digitizes the photoresist response. This mechanism is schematically depicted in Figure 2.2(a), with three spatially separated dose profiles along the x-direction for different exposures. In the case of D_1, the exposure dose is lower than the threshold dose and no stable polymer network is formed based on this model. For D_2 and D_3, the exposure in a spatially confined region of the dose profile is higher than the threshold dose. Thus a stable feature is formed during the polymerization with a widths which corresponds to the filled region of the peak above the threshold value. Based on this model alone, it would be possible to fabricate small features arbitrarily close together, independent whether the absorption process is linear or nonlinear [15, 20].

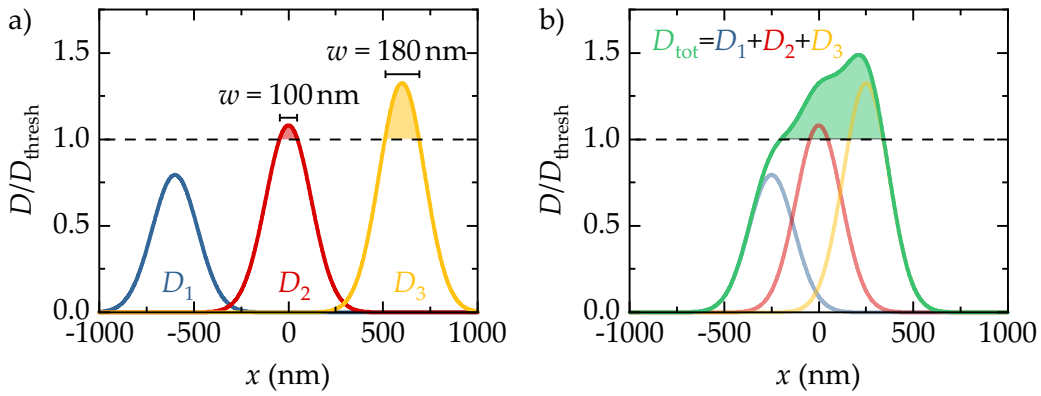

Figure 2.2: Schematic of photoresist behavior. (a) Dose profiles for three exposures with different exposure doses along the x-axis. In the threshold model, the exposure leads to a polymerized feature if the dose is larger compared to the threshold dose of the photoresist (dashed line). The filled area below the curves indicates the width w of the polymerized feature, i.e., the spatial extent of the exposure above the threshold. (b) For multiple exposures, the total exposure is given by the sum of the individual exposures (accumulation model). The resulting polymerized feature is indicated by the green area. Based on Gaussian intensity profiles with FWHM $= 400\,\text{nm}$ and $N = 2$.

This behavior drastically changes by additionally considering the accumulation model which assumes a "memory" for photoresists. Thus, all subsequent exposures at any position in a photoresist are integrated, regardless if the individual exposures are above or below the threshold. The total exposure dose is again evaluated on basis of the threshold model to determine whether a stable polymer network has formed. The implications of both models are depicted in Figure 2.2(b) for the same three exposures but less spatial separation. Based on the accumulation model, the total exposure dose D_{tot} is given as the sum of the individual exposure doses (colored in green). This examples directly demonstrates two important consequences: First, exposure D_1 alone is below the threshold, but it still contributes to the shape of the polymerized feature. Second, even though D_2 and D_3 are spatially separated above the threshold, the resulting feature given by D_{tot} is not. These considerations again lead to two important implications: First, the minimum separation distance between adjacent features is now limited and determined by the Sparrow criterion (see next section). Second, integration over all exposures at different positions makes it impossible to use a linear absorption process for the fabrication of complex 3D structures.

The second statement can be understood by considering the relation between exposure dose and light intensity. For a one-photon absorption (1PA) process, the exposure dose D is given by the linear relation

$$D_{1\mathrm{PA}}(x,y,z,t) \overset{\text{acc. model}}{=} D_{1\mathrm{PA}}(x,y,z) \propto \int I(x,y,z,t)\mathrm{d}t, \tag{2.7}$$

with the light intensity I. Since the accumulation model is applied, all light intensities are integrated and the exposure dose is no longer dependent on time. If the exposure dose is larger than the threshold dose

$$D_{1\mathrm{PA}}(x,y,z) \geq D_{\mathrm{thresh}}, \tag{2.8}$$

the polymer network is sufficiently crosslinked to withstand the development. The laser focus, however, has a Lorentzian shape on the optical axis [21] and the light intensity is not arbitrarily confined. Thus, by exposing a point somewhere in the photoresist, a small portion of the dose is also deposited along the axial direction. And since the photoresist remembers all previous exposures, the dose accumulates over the whole fabrication procedure. The same arguments also hold in the lateral direction, although the effect is less pronounced.

The implications of these arguments become apparent in a simple thought experiment [15, 19]: the peak light intensity $I(z)$ (limited to the axial direction for simplicity) in a laser focus is chosen such that the exposure dose $D(z)$ is just sufficient to reach the threshold dose D_{thresh}. Consequently, the polymer network is sufficiently crosslinked and a stable material is formed. At another position $z + \Delta z$ along the optical axis in the tail of the laser focus, the intensity is only a fraction of the peak value, e.g.,

$$I(z + \Delta z, t) = 0.01 \times I(z,t). \tag{2.9}$$

For 1PA, the exposure dose is directly proportional to this tail intensity:

$$D_{1\mathrm{PA}}(z + \Delta z) \propto \int I(z + \Delta z, t)\mathrm{d}t = 0.01 \times \int I(z,t)\mathrm{d}t. \tag{2.10}$$

With the accumulation model in mind, it becomes clear that the point at position $z + \Delta z$ will also polymerize to a stable network if the laser focus is scanned for 100 times and all the exposure tails add up.

In a two-photon absorption (2PA) process, however, the absorption and thus the exposure dose is proportional to the intensity squared. Thus, even though the light intensity of the tail remains unchanged, the resulting exposure dose deposited in the photoresist is significantly reduced:

$$D_{2\mathrm{PA}}(z+\Delta z) \propto \int I(z+\Delta z,t)^2 \mathrm{d}t = 0.0001 \times \int I(z,t)\mathrm{d}t. \tag{2.11}$$

Even after 100 scans, the exposure at position $z+\Delta z$ is only 1 % of the threshold dose and no stable network is formed. This suppression of intensity tails by exploiting the two-photon absorption is the crucial mechanism of DLW, which enables the fabrication of complex 3D structures.

2.1.3 Resolution and Feature Size

For lithography processes it is important to distinguish between feature size and resolution of a system. The minimally achievable feature size is defined as the spatial extent of the smallest structure that can be fabricated. For DLW, this corresponds to one voxel polymerized in the laser focus with a peak intensity close to the threshold dose. In the simple theoretical threshold model introduced in the previous section, the feature size is not limited at all if the threshold is indeed infinitely sharp to digitize the photoresist behavior. The laser power could be adjusted in such a way that only the peak intensity in the center of the laser focus is above the threshold. This aspect becomes immediately clear in Figure 2.2(a), for an exposure dose yet lower than the depicted example D_2. In experimental settings, however, minimum lateral features sizes are typically around $50-100\,\mathrm{nm}$ for functional 3D structures [22]. Possible explanations between the deviations from the model are diffusion effects in photoresists [17] or statistical fluctuations [23] which eventually lead to broadening of the polymerization threshold. The feature size is only relevant for individual structures sufficiently far apart from each other. In this regard, it can be compared to the localization accuracy of single objects in microscopy.

In microscopy, however, it is typically required to resolve structures very close to each other. Similarly, complex 3D structures are often composed of individual parts in very close proximity, e.g., in photonic crystals [24]. Along this line, the resolution of a lithography system specifies how close

two isolated features can be fabricated to each other. In widefield optical microscopy, the lateral resolution limit to resolve the smallest possible grating period $d_{x,y}$ was formulated by Ernst Abbe [25] as

$$d_{x,y} = \frac{\lambda}{2n\sin(\alpha)} = \frac{\lambda}{2\mathrm{NA}}, \tag{2.12}$$

with the wavelength λ, the refractive index of the medium n, the opening half angle α of the optical system, and the numerical aperture NA. The corresponding formula for the axial resolution limit d_z along the optical axis is given as [15]

$$d_z = \frac{\lambda}{n - \sqrt{n^2 - \mathrm{NA}^2}}. \tag{2.13}$$

Since this resolution limit is a fundamental consequence of the diffraction of light, it is typically referred to as the diffraction limit. In the context of lithography, the grating period corresponds to the minimal distance between two features during parallel exposure. At first glance, the situation seems to be different if two features are written in a sequential process as it is the case in DLW. The accumulation model, however, states that the photoresist remembers all previous exposures. One immediate conclusion from this formula is that the axial resolution in DLW is at least a factor of 2 higher compared to the lateral resolution if only one objective is used. In the ideal case of $\alpha = 90°$, NA is equal to n and the axial resolution is twice the lateral resolution. For this reason, the voxel in which polymerization takes place can be typically approximated as an ellipsoid with an elongated axis in the z-direction.

Another definition of resolution often applied in 3D laser lithography is Sparrow's criterion, which originates from astronomical spectroscopes [26]. In this definition, two fabricated structures are still resolvable if the exposure dose between them has a local minimum. This situation is schematically illustrated in Figure 2.3. Two consecutive exposure doses (blue) lead to the resulting, total exposure dose (green) based on the accumulation model. In panel (a), the distance of both individual dose profiles is $d = 280\,\mathrm{nm}$ and the resulting total exposure dose has a local minimum which can be shifted below the threshold value. As a consequence, it is still possible to resolve both exposures as individual features. In panel (b), the distance was reduced to $d = 240\,\mathrm{nm}$. Now the local minimum is no longer present and the total exposure dose results in a single, large feature.

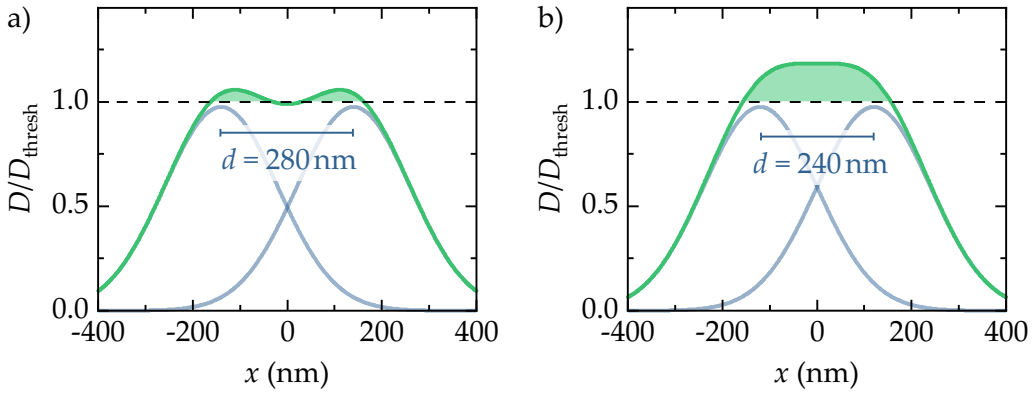

Figure 2.3: Schematic illustration of Sparrow's criterion in 3D laser lithography. The green curve depicts the total exposure dose as a sum of the individual exposure doses, here colored in blue. For a distance of $d = 280\,\text{nm}$ between the exposures (a), the total exposure dose has a local minimum and it is still possible to resolve two individual features. In the case of a reduced distance of $d = 240\,\text{nm}$ (b), the local minimum of the total exposure dose vanishes and only a single, large feature remains. Based on Gaussian intensity profiles with $\text{FWHM} = 400\,\text{nm}$ and $N = 2$.

The resolution limits obtained from such considerations can be approximated by a slight modification of Abbe's formula [15]:

$$d_{x,y} = \frac{1}{\sqrt{N}} \times \frac{\lambda}{2\text{NA}}, \tag{2.14}$$

$$d_z = \frac{1}{\sqrt{N}} \times \frac{\lambda}{n - \sqrt{n^2 - \text{NA}^2}}. \tag{2.15}$$

The additional prefactor $1/\sqrt{N}$ takes the resolution improvement for processes with nonlinearity N into account. For a linear 1PA process with $N = 1$, the original Abbe formula is retrieved. In case of the a 2PA process with $N = 2$ as typically the case in DLW, the resolution decreases by a factor of $1/\sqrt{2}$. For the setup used in this work with $\text{NA} = 1.4$, $\lambda = 780\,\text{nm}$, $n = 1.5$, and $N = 2$, the lateral resolution is around 200 nm and the axial resolution around 600 nm.

2.2 Fabrication of Stimuli-Responsive Hydrogels

The fabrication of stimuli-responsive hydrogels via DLW has several special characteristics compared to conventional materials. In this section, I introduce the most important differences and discuss the crosslinking mechanisms and their implications in more detail.

The composition of photoresists to fabricate stimuli-responsive hydrogels is based on three main components: monomers, photoinitiators, and crosslinkers—all mixed in an appropriate solvent. The stimuli-responsive properties are typically incorporated in the material by selecting adequate monomers. They exhibit a response to external stimuli like pH or temperature which can be either due to the presence of functional groups or due to the general structure of the molecule and its interaction with the surrounding. Additionally, these monomers contain acrylates or acrylamides which are groups that can be attacked by radicals and are thus incorporated in polymer chains during a radical polymerization procedure (see section 2.1.1).

The second important component is a suitable photoinitiator to start the polymerization reaction upon illumination. Here, a high two-photon cross-section (probability for two-photon absorption) at the laser wavelength of the employed setup is desirable to efficiently generate radicals. Furthermore, the photoinitiator has to be soluble in water or polar solvents as typically used for hydrogels. This requirement is more difficult to fulfill since research in this direction has only emerged in the last years [27–29] and most commercial products are designed for unpolar solvents. For applications in the biomedical field, a low cytotoxicity is yet another crucial constraint which has to be considered. One very promising candidate to fulfill all these aspects is LAP[1] [30], a water-soluble photoinitiator with a high biocompatibility which recently became available as a commercial product. LAP has a local one-photon absorption maximum around 380 nm [30] which fits well to the two-photon excitation wavelength of 780 nm in our setup (see section 3.1). Although the relation of the absorption spectra in 1PA and the initiation efficiency for 2PA is generally not as simple as multiplying the wavelength by a factor of two [31, 32], LAP exhibits a good two-photon absorption at a fundamental wavelength around 800 nm and is now widely applied for applications in aqueous environments [33–36].

[1] Lithium phenyl-2,4,6-trimethylbenzoylphosphinate

2.2.1 *Impact of Different Crosslinking Mechanisms*

Most stimuli-responsive monomers have only one reactive group which can be attacked during radical polymerization. As discussed in section 2.1.1, this leads to the formation of individual polymer chains which are not covalently connected to each other and thus an insufficient stability. For this reason, additional, non-responsive crosslinkers with more than one reactive group are added to the photoresist. They serve as links between individual polymer chains and enable the formation of networks which are sufficiently stable to withstand the development procedure (see Figure 2.1(b)). For the fabrication of non-responsive, static structures, a high mechanical stability and good writing conditions are the most important process parameters to consider. Thus, these photoresists contain only crosslinkers with multiple photopolymerizable groups for a fast and dense network formation. In stimuli-responsive hydrogels, however, the amount of additional unfunctional crosslinkers in relation to functional monomers is critical. The external stimulation of these systems typically leads to swelling or shrinking of the hydrogel. But this effect is strongly suppressed if the polymer network is too stiff and rigid. As a consequence, an increased mechanical stability directly opposes the desired functionality and the ratio between stabilizing crosslinkers and functional monomers is a delicate balance. Thus, one of the most important tasks is the development of a photoresist composition which enables the fabrication of the desired structures while still maintaining a maximum functionality of the material. This principle is schematically depicted in the scheme in Figure 2.4 for a covalently crosslinked hydrogel which swells upon stimulation.

The direct relation between crosslinking density and material response can also be turned into an advantage to fabricate different materials from the same photoresist. Variation of the laser intensity and thus the exposure dose during fabrication leads to changes in the crosslinking density of the material. The density of the polymer network in turn has direct implications on the material properties. This technique called gray-tone lithography basically enables the tuning of material parameters as a function of the exposure dose. Here, the experimental reality is more complex than the simple threshold model introduced in section 2.1.2 which digitizes to "material" and "no material" after development. Several studies in the past have shown that a stronger exposure during fabrication increases the stiffness of the fabricated structures [37, 38]. In another work by Qu. et al., different

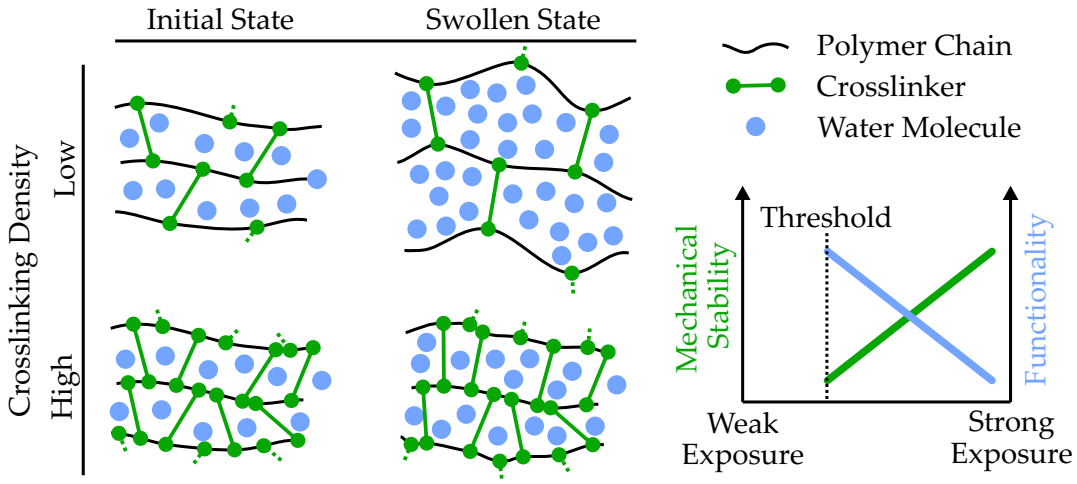

Figure 2.4: Schematic stimuli-response of covalently crosslinked hydrogels. The crosslinking density of the polymer network directly affects both, the mechanical stability and the functionality. For an exposure dose close to the threshold, the mechanical stability is low but the material shows a strong response to the external stimulation. By increasing the exposure dose, the structures become more stable but the functionality gradually decreases.

exposure doses in a conventional photoresist led to slight changes in the thermal expansion coefficient [39]. The resulting materials were combined to fabricate a metamaterial with an effective negative thermal expansion [39].

Although the basic mechanism is the same, the implications of gray-tone lithography on stimuli-responsive hydrogels are significantly larger. First, it enables the control over the active response of structures to external stimulation instead of merely passive material properties. Second, the tuning window of the crosslinking density and thus the material parameters is significantly larger. Polymer networks in hydrogels are generally less dense compared to conventional photoresists since the amount of crosslinkers is kept small. During fabrication, the liquid photoresist immediately swells the polymerized parts which in turn provides new material to trigger and continue the radical reaction. Consequently, a large exposure dose gradually increases the crosslinking density whereas an upper limited is quickly approached in conventional resists. As a result, the material properties in these systems can be effectively tuned from “non-responsive” to “strongly

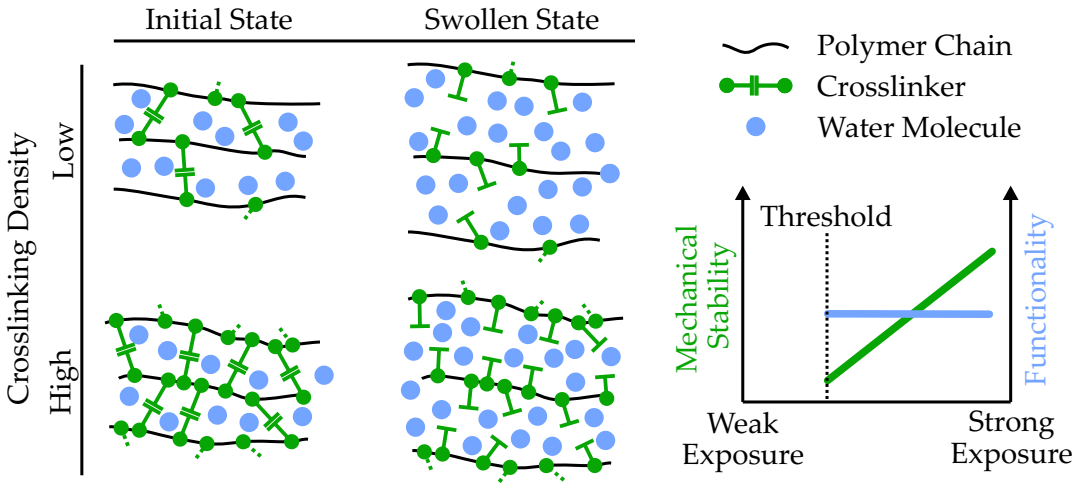

Figure 2.5: Schematic stimuli-response of hydrogels crosslinked by non-covalent interactions. External stimulation disrupts the interactions and opens the connections between polymer chains. Increasing the crosslinking density increases the mechanical stability, whereas the functionality remains mostly unaffected.

responsive" by variation of the exposure dose in a single resist. This toolbox in combination with an responsive material system offers vast opportunities for interesting applications, as I present in detail in chapter 4 of this thesis.

Most stimuli-responsive photoresist systems are based on functional monomers and non-functional crosslinkers. A second interesting approach is the incorporation of functionality directly in non-covalent crosslinks which basically reverses all advantages and disadvantages discussed so far in this section. The schematic image in Figure 2.5 shows the implications of this modification. Most importantly, the crosslinking density and the responsivity of the material are no longer opposing each other. Thus, it is possible to increase the mechanical stability while the strength of the stimuli-response remains mostly unaffected. On the other hand, for the same reason it is no longer possible to apply the gray-tone technique. While this approach might be generally favorable, it is inherently difficult to find suitable functional monomers with multiple acrylate or acrylamide sites for the formation of polymer networks. In chapter 5 of this thesis, I demonstrate the capabilities of a novel material system with crosslinks formed by host-guest complexes, which can be externally manipulated to change the properties of the fabricated microstructures.

2.2.2 *Challenges in Hydrogel Fabrication*

Aside from the important effects of the crosslinking mechanisms, some general properties have to be considered in the fabrication of stimuli-responsive hydrogels by 3D laser lithography. The density of the polymer network is typically low compared to conventional materials. This aspect is imperative since water or other polar solvents have to diffuse into the material, but it brings some significant disadvantages. The material swells during both, the fabrication as well as the development procedure. Thus, the achievable resolution is not only determined by the voxel size and the polymerization kinetics, but also by the material swelling. As a result, the minimum resolution is significantly larger than the typical values for conventional materials given in section 2.1.2. Furthermore, the fabrication of isolated lines is challenging because the mechanical stability is often so low that individual lines will not survive the development procedure, even though the network formation is clearly observable during writing. This aspect is also connected to the possible detachment of structures during swelling in the development procedure. To circumvent this problem, silanization of the glass substrate to covalently attach the fabricated structures is even more important compared to conventional materials (see section 3.1.2 for details). Yet another implication of swelling is the variation of the actual structure shape from the initial design during fabrication. In conventional DLW, this problem exists in the reverse way as shrinkage during the drying process. Compared to typical shrinkage factors of few percents [40], however, the post-fabrication swelling in hydrogels can be in the order of 100 %, depending on material, crosslinking density and solvent. Here it is important to remember, that hydrogels are kept in an aqueous environment at all times, whereas conventional structures are typically dried after development. Thus it is crucial to already consider post-fabrication swelling in the initial design.

Further technical challenges are related to polar solvents in the hydrogel photoresists, which are typically based on water. The low refractive index of water around $n = 1.33$ makes it difficult to match it with the refractive index of glass. Since oil-immersion objectives are by far the most commonly used lenses in DLW systems, the refractive index mismatch leads to a distortion of the laser focus while it travels through the photoresist. As a result, the structure quality degrades along the z-direction which ultimately limits the maximum height along with the working distance of the objective. This can be circumvented by using water-immersion objectives, although a sequential fabrication with conventional materials gets more time consuming in this

case. The low refractive index also makes it more complicated to use the option of dip-in lithography, a technique to directly dip the objective inside the liquid photoresist [41].

The challenges mentioned in this section apply certain limits to the fabrication of stimuli-responsive hydrogels. Most importantly, special care has to be taken in the design to account for the significant swelling of the structures during and after fabrication. Nonetheless, 3D laser lithography of hydrogels offers a great inherent flexibility and provides routes to structures for applications which were previously inaccessible with other fabrication techniques.

2.3 Basics of Mechanobiology

One of the most promising areas of application for stimuli-responsive hydrogels is the biological and biomedical field, e.g., cell biology. In chapter 5, I present our results on stimuli-responsive scaffolds to study the cellular response upon mechanical stimulation in tailored 3D environments. To provide a basic understanding of the underlying biological processes, I give a short general introduction to mechanobiology and specifically focus on the actin cytoskeleton and the role of myosin class II motor proteins. The discussion follows the PhD thesis of Kai Weißenbruch [42] as well as the reviews of Vogel et al. [43] and Blanchoin et al. [44].

The field of mechanobiology deals with the mechanism on how mechanical properties of cells and their surrounding tissue contribute to fundamental biological processes. As schematically depicted in Figure 2.6, cells are in a constant interaction with their surrounding. Mechanical inputs like compression, stretching, or the material stiffness define and change the cellular environment. Cells are able to sense and respond to these signals, a process generally termed mechanotransduction. In this context the focal adhesions of cells play a critical role, because they are directly linked to the extracellular matrix (ECM). Forces in the extracellular surrounding can lead to the extension of proteins. This extension reveals previously inaccessible binding sites which induce further intracellular signals and processes. The cellular reaction to these cues leads to an active adaption of their mechanical properties, like the cell shape or the actomyosin contractility, which are discussed in detail in the following sections.

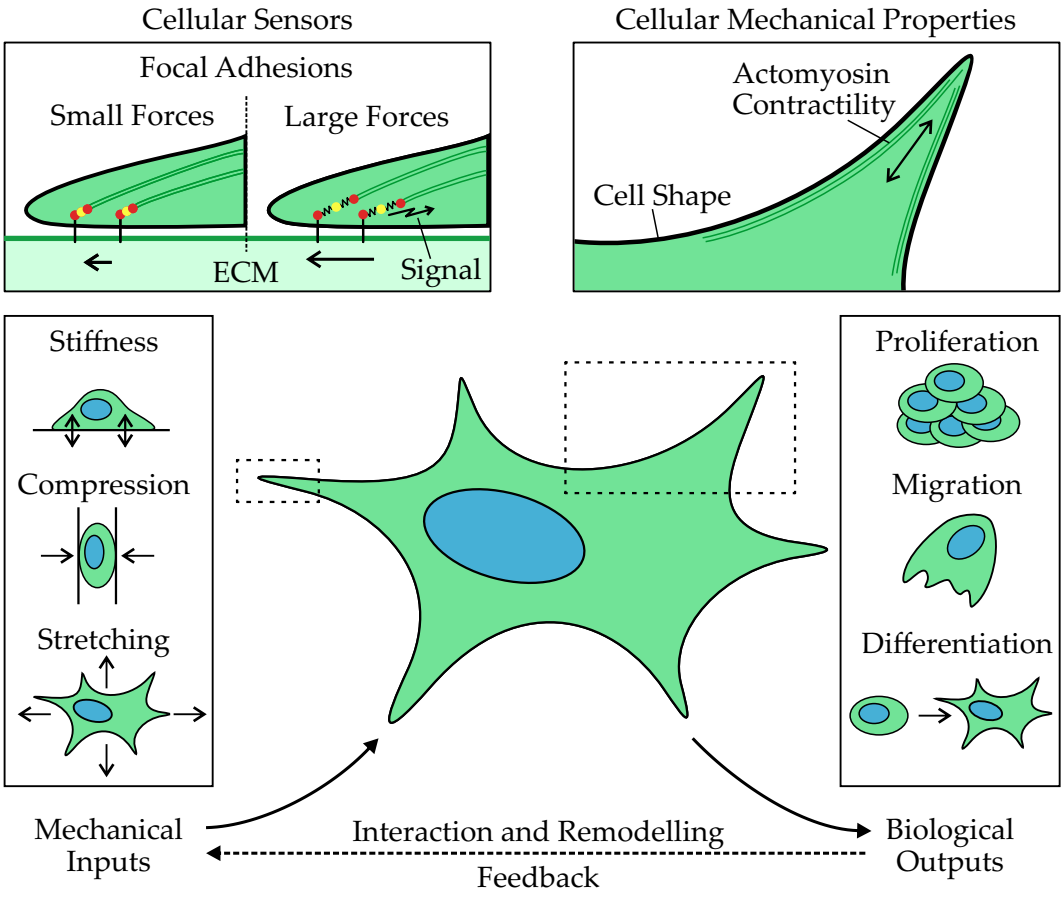

Figure 2.6: Schematic overview of mechanobiology. External mechanical inputs like stiffness changes of the substrate, compression and stretches are analyzed by cellular sensors. A typical example are focal adhesions as the contact sides between the cell and the extracellular matrix. Forces in the surrounding are transmitted by the extension of proteins which trigger further intracellular signals. Changes in the extracellular surrounding as well as the cellular mechanical properties directly influence biological processes like proliferation, migration and differentiation. In a feedback loop, cells are also able to interact with their environment and to remodel their cytoskeleton. Based on a figure by Dr. Sarah Bertels (KIT).

Ultimately, the mechanical inputs can trigger and guide fundamental biological processes like proliferation, migration and differentiation [45]. Moreover, this interaction is mutual and the biological mechanisms in turn influence the mechanical properties. Cells actively remodel their environment like the extracellular matrix and rearrange their cytoskeleton to adapt their shape and contractility. In the following sections, I mainly focus on the cellular generation of forces by actomyosin contractility.

Animal cells have the fundamental ability to generate intracellular forces, which are the basis for the contraction of muscle-tissue. Research in the last decades has revealed, however, that these forces are also crucial for many processes in non-muscle cells. This includes important dynamic processes like cell adhesion, migration, division, and the adaption to changes in the cellular environment [46–48]. To fulfill all these tasks, the force generating machinery has to provide a high degree of stability and flexibility simultaneously. The basis of this machinery is a complex cytoskeleton with three main components: actin, microtubules, and intermediate filaments. From a biomechanical point of view, actin is the most important component since it is strongly connected to the cellular adaption to its environment. In combination with the actin-associated myosin II motor proteins the system acts as both, a passive, intracellular scaffold as well as an active, force-generating unit.

2.3.1 Actin Cytoskeleton

Actin is one of the most common proteins in animal cells. Globular actin monomers (G-actin) polymerize in a non-covalent manner to actin filaments (F-actin) with a structural polarity. The mechanical properties of these filaments can be compared to a flexible cable which tolerates strain as well as compression [49]. This behavior is important to provide a basic stable network for the cell body with yet sufficient flexibility to rapidly adapt to changes in the extracellular environment [50]. The generation of intracellular forces by the actin cytoskeleton can be divided into two categories: First, compression forces can by generated by a specifically targeted actin polymerization close to the cellular membrane. This leads to the formation of protrusions, e.g., in the context of cellular migration. The second process known as actomyosin contractility is the establishment of contraction forces by the interaction of actin filaments and myosin II motor proteins [51]. In this thesis, we studied cells in tailored 3D environments

during the application of defined mechanical stimulations. The adhesion sites for these cells are restricted to normalize the cellular morphology and to prevent cells from migrating. Furthermore, cells respond by increasing their contraction forces to counteract the external stretch. Thus, I discuss the underlying mechanisms behind the actomyosin contractility in the following sections in more detail.

The prerequisite for the interaction of actin filaments and myosin motor proteins is the establishment of higher-order structures which are regulated by multiple proteins that bind to actin [52]. A typical example is the actin cortex, a loose actin network crosslinked by filamin proteins. In this work, however, we focus on actin stress-fibers which are a very important structure in non-muscle cells.

Actin Stress Fibers

Actin stress fibers consist of 10-30 actin filaments which are clustered by α-actinin in an anti-parallel arrangement [53, 54]. Furthermore, they are strongly associated to non-muscle myosin motor proteins of class II (NM2) [50]. A schematic image of an actin stress fiber with actin filaments, myosin II motors and α-actinin is depicted in Figure 2.7. NM2 proteins connected to several of these filaments are responsible for the contraction forces by pulling the respective elements towards each other. Importantly, the stress fibers are directly connected to the focal adhesions which anchor the cell to the extracellular matrix. Since they span through the cell body, stress fibers connect multiple focal adhesions and further subcellular compartments. Thus, they stabilize the cell body and maintain the cellular morphology. Furthermore, the direct connection of stress fibers to the extracellular matrix enables them to sense mechanical inputs and to transform them to biochemical signals. This process, known as mechanotransduction, is essential for the interaction of cells with their environment and adaption to external cues. For instance, cells cultivated on substrates with different degrees of stiffness develop thicker and more bundled stress fibers in stiffer environments [55]. The direct correlation between the mechanical properties of the extracellular matrix and stress fibers highlights their function in a physiological context. Cells in tissue which are subjected to large stresses also build up a large amount of stress fibers. Prominent examples of this behavior are the establishment of stress fibers in myofibroblasts during wound healing [56] and in endothelial cells as a function of the hydrostatic pressure in vessels [57, 58].

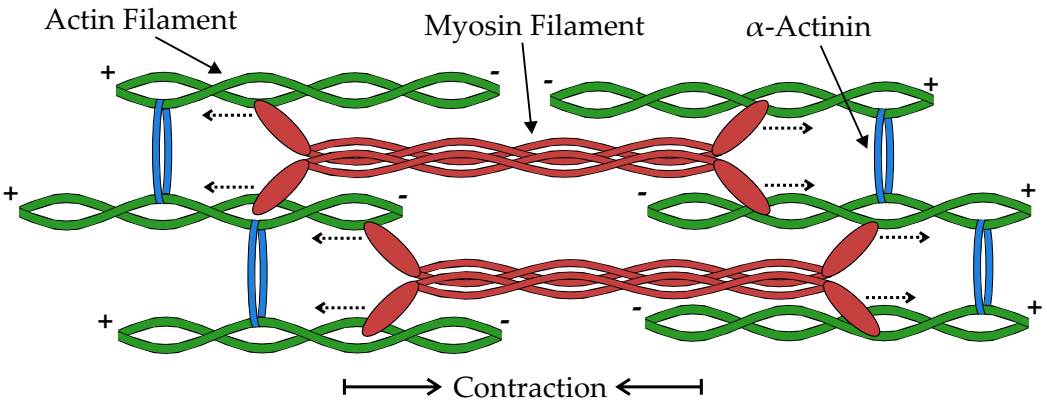

Figure 2.7: Schematic depiction of a stress fiber in non-muscle cells. Actin filaments (green) are arranged in an anti-parallel manner and connected with each other by α-actinin (blue). The polarization is indicated by the "+" and "-" signs. Myosin filaments (red) assemble between the α-actinin molecules. Movement of the myosin heads towards the "+" side of the actin filaments leads to an effective contraction of the stress fiber. Figure based on [42].

2.3.2 *Class II Myosin Motor Proteins*

Myosins are a group of motor proteins associated to actin which can be separated in 18 different classes. The common ability of these proteins is the conversion of chemical energy into a directed motion along the polarity of actin filaments [59]. The individual classes are typically distinguished by their functions, e.g., myosins coupled to the membrane (class I and class VI) [60] or cargo-transporting myosins (class V) [61]. For this thesis, however, I limit the discussion to myosins of class II which are mainly responsible for the generation of intracellular forces.

Myosins of class II have a hexamer structure with a head and a tail region with different binding domains. Electrostatic interactions between different parts of the protein lead to a combination of multiple of these hexamers to a myosin filament [62]. Since these hexamers arrange in an anti-parallel manner, the resulting filament is bi-polar with head regions at both ends. These head regions are attached to the actin filaments in stress fibers as depicted in Figure 2.7. Conversion of chemical energy in form of adenosintriphosphat hydrolysis leads to conformational changes in the head region and a subsequent movement of the heads along the actin filaments. The sequence of conformational changes to achieve this behavior is described as the cross-bridge cycle [63]. The myosin heads always move towards the

"+" side of the polarized actin filament whereas the tail regions connect the heads with each other. Thus, only an anti-parallel arrangement of actin fibers effectively leads to a contraction.

Myosins of class II can be further subdivided into four different groups. However, since the results presented in chapter 5 are based on non-muscle cells, I focus on the subgroup of non-muscle myosin II.

Non-Muscle Myosins of Class II

NM2 motor proteins are the main driver of actomyosin contractility in non-muscle cells. The general hexamer structure of NM2 is similar to class II myosins in muscle cells, but size, contractile output, and dynamics vary considerably. Non-muscle myosins incorporate about ten times less hexamers per filament compared to myosins in muscle cells [64]. The number of hexamers which can be added to a filament is restricted by steric hindrance, limiting the ability to bind actin and generate forces [65]. Furthermore, NM2 filaments show significantly faster dynamics by continuous cycles of polymerization and depolymerization [66]. This ability enables the filaments to quickly adapt the contractility on a sub-cellular level.

As of today, three different myosin isoforms labeled as NM2A, NM2B, and NM2C are known in literature. Most cell types express multiple NM2 isoforms at the same time, although NM2A is almost always present. Previous studies have also shown that cells are able to adapt the expression of individual isoforms during different cellular transitions [67]. While NM2A and NM2B are rather well studied, little is known about NM2C. All three isoforms can assemble to bipolar filaments and contract actin stress fibers by hydrolysis of adenosintriphosphat. The sequence of conformational changes, however, is significantly faster in NM2A which leads to a 2-3 times faster movement along the actin filaments compared to the other isoforms [68, 69]. NM2B on the other hand, has a high duty ratio, which describes the timescale when the myosin is stably bound to the actin filament. Consequently, NM2B can withstand higher stresses and sustain contraction forces over longer periods of time [69, 70]. Although extensive kinetic information about NM2C is not available yet, previous studies suggest that the movement along actin fibers is similar to NM2B and thus significantly slower than NM2A [71].

The differences in kinetic properties between the myosin isoforms lead to the conclusion that they perform specialized tasks in cellular processes. Several studies on the impact of different isoforms have shown, however, that processes like cell adhesion or migration are strongly affected by NM2A

whereas the effects of NM2B and NM2C are more subtle. The important role of NM2A can also be observed in knock-out cells lacking this isoform. These cells show strong defects in the organization of the actin cytoskeleton and actin stress fibers, along with a striking cell phenotype change to a round and flat morphology with long protrusions [72]. In particular, knock-out of NM2A shows drastic effects on the actomyosin contractility. Even though the other isoforms are still present, NM2A knock-out cells lose $60 - 100\,\%$ of their contraction forces [73, 74]. In summary, NM2A has a crucial role to maintain the structure of the actin cytoskeleton and to generate contraction forces. NM2B on the other hand has a more stabilizing function and can maintain larger stresses over prolonged time periods [42].

3 Chapter 3 Methods

In this chapter, I describe the most important experimental methods which have been used throughout this work. The first section summarizes several aspects about 3D laser lithography from the fabrication setup and photoresist compositions to writing strategies of specific microstructures. Afterwards, I discuss the application of atomic force microscopy and laser scanning microscopy for sample characterization in the context of this thesis. The subsequent section contains details on the finite element calculations which have been used to model the structural response. Finally, I describe the methodical aspects and protocols of the cell biological experiments.

3.1 3D Laser Lithography

3D laser lithography is the technique we used for the fabrication of all samples which are presented throughout this thesis. While the fundamentals of the underlying two-photon polymerization have been discussed in section 2.1, I focus here on the more technical aspects. I start with a description of the fabrication setup and the required workflow for sample preparation. Next, I introduce all photoresist compositions which are used throughout the experiments presented in this thesis. In the last two subsections, I explain the fabrication procedures for both stimuli-responsive material systems in detail and discuss the most important aspects as well as limitations.

3.1.1 Fabrication Setup

All samples shown in the scope of this thesis were fabricated with the commercially available Photonic Professional GT (Nanoscribe GmbH) system. A schematic overview of the setup with its most important components is

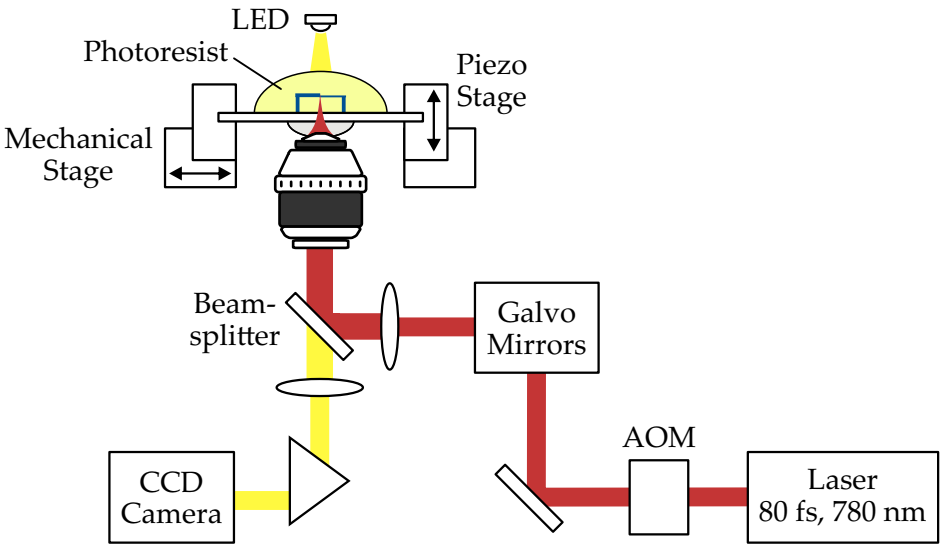

Figure 3.1: Schematic illustration of the Photonic Professional GT (Nanoscribe GmbH). A femtosecond pulsed laser is tightly focused into the liquid photoresist to start the radical polymerization. The laser power can be controlled by the acousto-optical modulator (AOM). Two galvanometric mirrors enable fast lateral scanning of the laser beam. Motion along the axial direction is achieved with a piezoelectric stage on which the sample is mounted. The fabrication process can be observed live by a CCD camera.

shown in Figure 3.1. It is based on a frequency doubled erbium fiber laser with a center wavelength of 780 nm and a pulse width below 100 fs at a repetition rate of 80 Mhz. Since the probability to initiate the polymerization is a function of the laser intensity squared, it is favorable to send very short pulses with high peak intensities (see section 2.1.2). Thus, femtosecond pulsed lasers are a natural choice for 3D laser lithography. Wavelengths around 800 nm are often used since the photoresists are typically transmissive in the near infrared and suitable two-photon initiators are available for this region.

The laser beam is first guided through an acousto-optical modulator (AOM) to control the transmitted laser power electronically. Typical laser powers at the back focal plane are between 10–50 mW. Two galvanometric mirrors enable fast scanning of the laser beam in the lateral plane with speeds up to 10 cm/s. The actual fabrication speed, however, is typically lower and strongly depends on the photoresist composition. After the laser beam passes an objective lens with a high numerical aperture it is tightly focused into a

liquid photoresist on top of a glass slide. The size of the accessible scanning field depends on the objective lens. For the 25×, NA = 0.8 objective lens used in chapter 4, it has a diameter of up to 400 µm, for the 63×, NA = 1.4 objective lens used in chapter 5, a diameter of about 200 µm. The glass slide is fixed to a holder in a piezo stage which moves along the axial direction during fabrication. The piezo stage is in turn attached to a mechanical stage which is used for coarse lateral movements, e.g., to change to a different position on the sample.

In the normal fabrication configuration, the laser beam travels through immersion oil, the glass substrate and finally the photoresist. The structures are written layer by layer from the glass substrate to the top. The galvanometric mirrors are used to scan along all designated lines in a plane. Afterwards, the piezo stage moves the sample in z-direction by a defined distance (typically referred to as slicing distance) and the process is repeated. The two major disadvantages of this so-called "normal configuration" are limited structure heights due to the working distance of the objective and distortions of the laser focus by traveling through already polymerized material and photoresist with an unmatched refractive index. The alternative is the so-called "dip-in" configuration where the objective is directly immersed into the liquid resist [41]. This technique, however, is only applicable for particular combinations of photoresist with an adjusted refractive index fitting to the objective. For all structures fabricated during this thesis we used the normal configuration as schematically depicted in Figure 3.1. To find the correct axial position between the glass substrate and the photoresist, a so-called "interface finder" is implemented in the setup. The underlying mechanism, however, is based on the reflection at the interface of both materials and thus only yields reliable results if the refractive index contrast is sufficiently strong. The setup also includes a CCD camera which enables live observation of structures during the writing procedure by illumination with a LED from the top.

3.1.2 Sample Preparation

For the fabrication of all structures presented in this thesis we used glass cover slides with a thickness of 170 µm. The working distance of the employed objectives subtracted by the thickness of the substrate thus limits the maximum structure height that can be achieved. All substrates were thoroughly cleaned with acetone and 2-propanol using a paper towel and

finally blown dry with a nitrogen gun. In the next step, the glass surface was activated in an air plasma for 20 min to generate hydroxyl groups on the surface [75]. Afterwards, the substrates were immersed for 1 h in a 1 mM solution of 3-(trimethoxysilyl)propyl-methacrylate in toluene. Trimethoxysilyl forms covalent bonds with the hydroxyl groups and anchors the molecules on the glass surface. The methacrylate groups, on the other hand, can be attacked by radicals and are thus incorporated in polymer chains during a radical polymerization process (see section 2.1.1). As a consequence, polymer networks which are generated during the fabrication are covalently linked to the substrate. This process, typically referred to as silanization, improves the adhesion of the fabricated structures to the substrate and prevents possible detachment, e.g., during development. This is especially important in the context of hydrogels which experience significant post-fabrication swelling during the transfer from photoresist to the developer and storage solutions.

3.1.3 Photoresist Compositions

In this thesis, we used several photoresists with different properties. In the following section, I list all compositions along with additional information on their preparation.

PETA Photoresist

The PETA resist was prepared by adding 20 mg of the photoinitiator Irgacure 819 to 980 mg of the tri-functional monomer pentaerythritol triacrylate (PETA). The mixture was ultrasonicated for about 2 h until the initiator was completely dissolved. To record fluorescent image stacks, Irgacure 819 was replaced by 5 mg of 7-diethylamino-3-thenoylcoumarin (DETC). DETC exhibits a strong fluorescence and is also an efficient two-photon initiator. For fabrication by 3D laser lithography, a droplet of the resist was placed on the coverslip. Structures were developed in a 1:1 v/v mixture of isopropanol and methyl isobutyl ketone (MIBK).

TPETA Photoresist

The TPETA resist was prepared in a similar way by adding 20 mg Irgacure 819 to 980 mg of the tri-functional monomer trimethylolpropane ethoxylate triacrylate (TPETA) with an average molecular weight of $M_n \approx 692$. The

resist was mixed in an ultrasonic bath for about 2 h until the photoinitiator was dissolved. A droplet of the photoresist on top of a coverslip was used for the fabrication by 3D laser lithography. Structures were developed in a 1:1 v/v mixture of isopropanol and MIBK.

pNIPAM Photoresist

The pNIPAM resist contains 400 mg of the thermo-responsive *N*-isopropylacrylamide (NIPAM), 40 mg of the crosslinker *N*,*N'*-methylenebis(acrylamide) and 15 mg of the water soluble photoinitiator lithium phenyl(2,4,6-trimethylbenzoyl)phosphinate (LAP). All components were dissolved in 450 µl of ethylene glycol. Additionally, 4 mg of acryloxyethyl thiocarbamoyl rhodamine B was added for fluorescent imaging. The rhodamine with an acrylate group enables the covalent integration of a fluorescent dye in the polymer network. In this way, we were able to record 3D image stacks of the fabricated structures.

Host-Guest Photoresist

The host-guest resist was prepared by adding 36 mg β-cyclodextrin acrylamide (βCD-AAm, host) and 6.6 mg of adamantane acrylamide (Ad-AAm, guest) to 200 µl water and 300 µl 2-propanol. The molar ratio of 1:1 between host and guest molecules facilitates the development of non-covalent interactions. This mixture was kept in an ultrasonic bath at 60 °C for about 1 h until all components are dissolved and the solution appears transparent. In the next step, the resist was cooled down to room temperature and 68 mg of Acrylamide (AAm) were added along with 5 mg of the photoinitiator LAP. After another 5 min in the ultrasonic bath at room temperature, the final resist was obtained. Importantly, the resist has to be pre-processed on a hotplate and a direct fabrication in the liquid form is not possible. A detailed description of the procedure is given in section 3.1.5.

With the assumption of 100 % polymerization yield and negligible swelling after development, the final concentration of host-guest complexes is about 60 mM. This value is three times higher compared to the maximum soluble concentration of 20 mM of competitive 1-AdCA guest molecules. The association constant of free host or guest molecules, however, is more than ten times larger compared to the association constant between host or guest molecules linked to polymer chains [76]. Thus, the comparatively low concentration is still sufficient to induce a significant swelling in the polymerized hydrogels.

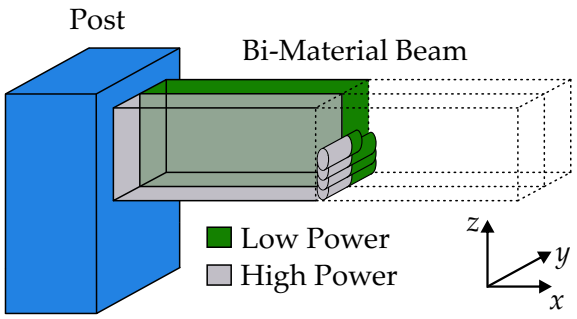

Figure 3.2: Fabrication strategy for bi-material beams. The laser powers for the fabrication of both sides of the beam are indicated in green (low power) and gray (high power). After fabrication of the post, lines are scanned in y-direction perpendicular to the beam. All lines in z-direction next to already polymerized parts are written first, before the next segment along the beam in x-direction is started.

3.1.4 *Fabrication of pNIPAM Bi-Material Beams*

For the fabrication of the pNIPAM bi-material beam structures presented in chapter 4, we used the commercial setup introduced in section 3.1.1, equipped with a 25×, NA = 0.8 oil immersion objective. A droplet of pNIPAM resist was added to a small ring of PDMS and sealed on top to prevent solvent evaporation during the process. Since the monomer in the resist is responsive to changes in temperature, it is important to maintain a controlled environment during the fabrication to avoid unwanted side-effects. Exceeding temperatures of about 30 °C leads to precipitation of NIPAM and even temperature changes of $2-3$ °C around room temperature already have significant effects (see discussion in chapter 4).

Unless stated otherwise, we fabricated the bi-material beams with laser powers at the back focal plane of 30 mW and 37.5 mW for the less and more crosslinked side of the beam, respectively. The hatching distance (lateral distance between lines) and slicing distance (axial distance between layers) were both fixed to 0.5 µm. For the post of the beam, we further increased the power to 40 mW to enhance the mechanical stability while suppressing the stimuli-response (see section 2.2.1). In all experiments with pNIPAM bi-material beams shown in chapter 4, the scanning speed was kept constant at 1 mm/s. The writing strategy was chosen as depicted in Figure 3.2, with a scanning direction along the y-axis perpendicular to the bi-material beam.

Furthermore, all lines along the z-axis next to already polymerized parts of the structure were fabricated first, before the next lines along the beam direction were started. This strategy ensures a maximum connection between new lines to already polymerized material and thus provided the sufficient mechanical stability to fabricate elongated beams as shown in section 4.4.4. The drawback, however, is a slower fabrication due to an excess of axial movements by the piezo stage.

After fabrication, the structures were rinsed with acetone and transferred to water for further development and storage. The hydrogel samples fabricated in this way have to be kept in an aqueous environment for all further experiments.

3.1.5 Fabrication of Responsive Host-Guest Scaffolds

The stimuli-responsive host-guest scaffolds presented in chapter 5 were fabricated in three consecutive steps with the commercial setup introduced in section 3.1.1. For all processes, we used a 63×, NA = 1.4 oil immersion objective. First, the TPETA resist was used to fabricate the passivation layer on the substrate, the alignment markers for the following steps, and, most importantly the walls of the scaffolds. We adjusted the scanning direction to be always parallel to the walls in their respective orientation to minimize variations of the thickness or network density due to the fabrication procedure. Typically, a laser power of 40 mW at the back focal plane and a scanning speed of 2 mm/s were used as process parameters. The hatching and slicing distance were both fixed to 0.5 µm. After development in a 1:1 v/v mixture of MIBK and 2-propanol, the samples were dried and stored for further usage. TPETA surfaces are hydrophilic and thus repellent to biological proteins. As a consequence, cells cannot properly attach to the structures fabricated with TPETA.

In the second step, we used the PETA resist to fabricate the beams on top of the scaffolds. To find the correct lateral position we used the alignment markers fabricated with TPETA. Furthermore, we used the alignment markers to calculate a coordinate transformation to correct small rotations of the sample during assembly and disassembly in the holder for development. Axial positioning was achieved with the built-in interface of the device and a fixed offset determined by the initial design. Typically, a laser power of 30 mW at the back focal plane and a scanning speed of 2 mm/s were used for the fabrication. The hatching and slicing distance were both

fixed to 0.5 µm. After this process, the samples were developed in a 1:1 v/v mixture of MIBK and 2-propanol and stored in developer solution until the last fabrication step was performed. Drying leads to capillary forces and subsequent partial attachment of the walls. We found, however, that this effect is reversible if the photoresist used in the third step is applied within a few minutes after the sample was removed from the developer. Although critical point drying could circumvent this problem entirely, it would add another time-consuming processing step to the procedure.

Surfaces of structures fabricated with the PETA resist have hydrophobic properties. Proteins in a an aqueous solution adsorb to these structures and remain in a functional configuration. At these positions, they provide anchor points for cells to build up adhesions and mimic the extracellular matrix. Combination of both, TPETA and PETA photoresist for the fabrication of composite structures thus provides a powerful tool to spatially control the protein coating and thus cellular attachment. This differentiation is the basis for the defined 3D microenvironments of cell scaffolds.

In the third step we used the host-guest photoresist to fabricate the stimuli-responsive hydrogel blocks inside of the scaffold. An amount of 5 µl of the resist were drop cast in a PDMS ring on the previously fabricated structures. Next, we put the coverslip on a hotplate for $1 - 2$ min at 50 °C to partially evaporate the solvent. The timing of this procedure is critical and also depends on the humidity in the room. If too much solvent evaporates, the remaining resist crystallizes and further processing is not possible. On the other hand, no suitable fabrication windows exists if the amount of solvent is still too high. After removing the sample from the hotplate, we fixed it in the sample holder in a sealed environment to prevent further evaporation of solvents during the fabrication. Similar to the PETA resist, we achieved a lateral alignment and the necessary coordinate transformation with the markers fabricated in the first fabrication step. For the axial alignment, however, it was no longer possible to use the built-in interface finder of the device. Most likely, the layer thickness of the resist is too thin in this configuration to yield a sufficiently strong signal. To circumvent this problem, we first used the built-in interface finder to determine the interface for 15 positions in a circle around the photoresist droplet. At the interface between glass and air, the refractive index contrast is sufficiently strong to determine the position with high accuracy. Next, we fitted a plane through these points to calculate the tilt of the coverslip in x- and y-direction. In the last step, we manually searched the interface at the first fabrication position and used the calculated angles to determine the necessary offset for every structure.

Typical fabrication parameters were a laser power of 40 mW in the back focal plane and a scanning speed of 5 mm/s. Furthermore, we fixed the hatching distance to 0.25 µm and the slicing distance to 0.5 µm.

Before we used the sample for further experiments, we immersed it for at least two days in a solution of 20 mM 1-AdCA in water. The solution leads to a swelling of the hydrogel which promotes the removal of unpolymerized material like monomers or photoinitiators from the polymer network. These residues can be cytotoxic and thus reduce cell viability in the structures. Additionally, we observed differences between the swelling behavior of the hydrogel during the first contact with 1-AdCA compared to all further experiments. We attribute these effects to initial tensions in the polymer network which are released after one initial swelling-shrinking cycle.

3.2 Atomic Force Microscopy

In the scope of this thesis, we used the commercial AFM NanoWizard (JPK Instruments) to mechanically analyze samples and to record height profiles. The device is designed for biological applications and thus well suited for measurements in aqueous environments as required for hydrogels. Samples are fixed in conventional petridishes, covered with the respective solvent, and inserted into the device. Furthermore, a heating unit is included in the AFM which allowed us to perform experiments at different temperatures without further modifications of the setup.

For all characterizations involving hydrogels, we used soft silicon nitride cantilevers (MLCT, Bruker) with a nominal spring constant of 0.03 N/m and a pyramidal shaped tip with a tip radius of $20 - 60$ nm. These cantilevers have reflective coatings on the backside to improve the signal on the photodiode. For experiments with varying temperature, however, silicon nitride cantilevers with an additional metallic coating act as bi-metallic stripes. The differences in thermal expansion coefficients lead to a distinct bending and thus false signals. For this reason, we used a variation of these cantilevers with the same spring constant but without the reflective coating on the backside (MLCT-UC, Bruker) for all temperature-dependent experiments in chapter 4. To determine the Young's moduli of TPETA and PETA we used All-In-One-AI cantilevers (BudgetSensors) with nominal spring constants of 7.4 N/m and 40 N/m, respectively (see section A.3). Although these materials are no hydrogels, we still performed the characterizations in water to mimic the experimental conditions as close as possible.

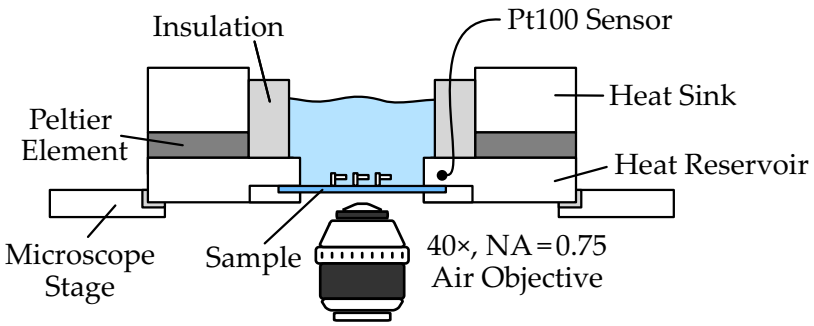

Figure 3.3: Schematic illustration of the designed Peltier chamber. The sample is fixed in the insulated chamber filled with water and connected to the heat reservoir. Depending on the configuration, the round Peltier element with a central hole heats or cools the bottom reservoir and thus the water bath around the sample. A Pt100 sensor records the temperature and feeds it into a feedback loop of the controller. The whole chamber can be integrated in an inverted microscope and is insulated against the microscope stage. The designs of the chamber and the associated electronic controller were developed together with Michael Hippe and Johann Westhauser (both KIT).

The nominal values for the spring constant of cantilevers stated upon delivery typically have high variances and an additional calibration step is necessary if they are used for mechanical characterizations. For the calibration, we applied the thermal noise method as implemented in the software of the device [77].

3.3 Confocal Laser Scanning Microscopy

The main tools we used for sample characterization and image acquisition were two confocal laser scanning microscopes. They enabled us to combine optical transmission images directly with fluorescent data and reconstruct 3D shapes of our structures based on the recorded image stacks.

LSM 510 META

To characterize the pNIPAM samples presented in chapter 4, we used a LSM 510 Meta (Carl Zeiss AG). The microscope was typically equipped with a

40×, NA = 0.75 air objective. To enable heating and cooling of samples inside the microscope, we designed a special sample chamber with a built-in Peltier element as depicted in Figure 3.3.

The chamber is designed as a ring with an opening in the center to be able to acquire transmission optical images through sample and water bath. The sample is inserted in the chamber via a bottom plate, which is fixed with screws. In this configuration, both the water bath and the sample are directly connected to the surrounding heat reservoir. The Peltier element is embedded between the heat reservoir and the heat sink on top with an insulation layer towards the water bath on the inside. An external controller regulates the voltage of the Peltier element based on the feedback input of a Pt100 temperature sensor placed inside the heat reservoir. With a PID control loop it is thus possible to approach the set temperature by active heating and cooling. This aspect prevents long waiting times, e.g., for reversibility experiments when the temperature is changed repeatedly.

LSM 800 with Airyscan

The second confocal microscope is a LSM 800 with Airyscan (Carl Zeiss AG) which we used to carry out the biological experiments presented in chapter 5. For live cell experiments as well as the image acquisition of fixed and stained cells, we used a 40×, NA = 1.2 water immersion objective. The microscope body is integrated in an incubation chamber which can be set to a temperature of 37 °C to provide optimal experimental conditions for cells. Furthermore, the microscope is equipped with a motorized stage which can be controlled via the Zeiss software. In this way, we were able to program the stage to cycle through preset positions and thus record time series of multiple cells in a single experiment.

During the live-cell experiments it is necessary to exchange the imaging medium to trigger the stimuli-response of the hydrogel scaffolds. Therefore, we designed a simple and compact microfluidic chamber as schematically depicted in Figure 3.4. The sample cover glass is attached to the chamber by a magnetic bottom plate. At two opposite ends of the chamber, we integrated small metal tubes bent towards the bottom cover glass. Outside of the chamber, flexible tubes are used to connect syringes to both ends. In this configuration, the medium in the chamber can be replaced by first removing the old solution with one syringe and injecting the new solution with the second one. Here it is important to tightly fix the whole chamber

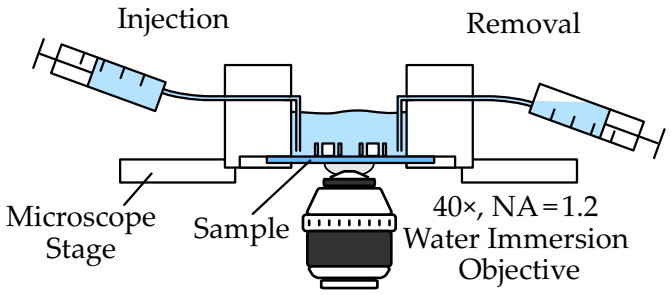

Figure 3.4: Schematic illustration of the designed microfluidic chamber. A magnet holder fixes the sample to the chamber filled with imaging medium. At opposite ends, metal tubes through the wall bent to the substrate. Flexible tubes are attached on the outside and connected to syringes which are used to inject or remove solution from the chamber.

to the microscope stage to avoid sample displacements during the injection procedure. The syringes are also stored inside the incubation chamber to keep all solutions at the same temperature.

3.4 Digital Image Cross-Correlation

The basis for the analysis of the live-cell experiments presented in chapter 5 is the precise tracking of the beam positions over the whole course of the experiment. We used a digital image cross-correlation algorithm programmed in MATLAB (Mathworks) to determine displacements in consecutive optical images of the time series. This method enables a sub-pixel position tracking [78] and has been widely applied in the past, e.g., to measure deformations in mechanical metamaterials [39]. The algorithm applied in this work is based on an open-access software package [79]. It has been used in several publications by members of our groups [39, 41] and was further adapted for the experiments in the scope of this thesis.

The basis of the algorithm is the one-dimensional cross-correlation function between two discrete functions $f(t)$ and $g(t)$:

$$(f \star g)(\tau) = \sum_{t=-\infty}^{\infty} f^*(t) g(t+\tau) \tag{3.1}$$

with τ being the discrete displacement, often referred to as the lag in the context of correlations in time. To apply this function to track the position of features in recorded images, it has to be expanded to two dimensions in space:

$$C(\Delta x, \Delta y) = (f \star g)(\Delta x, \Delta y) = \sum_{x,y=-\infty}^{\infty} f^*(x, y) g(x + \Delta x, y + \Delta y). \quad (3.2)$$

Here, $f(x, y)$ and $g(x, y)$ represent two images with gray values at each position corresponding to one pixel. In the simple case that the whole image $f(x, y)$ is merely translated relative to $g(x, y)$, the displacements Δx and Δy at the maximum of the cross-correlation function $C(\Delta x, \Delta y)$ yield the applied translation vector. However, we are typically interested in the displacement of specific features in the image, e.g., one of the four beams of the scaffold, relative to a reference image. Therefore, we do not calculate the sum over the whole image but only over an area defined as the region of interest (ROI). Furthermore, due to brightness variations, individual images are typically normalized by subtracting the mean value and dividing by the standard deviation.

The cross-correlation process is exemplarily depicted in Figure 3.5. Panel (a) shows a reference image and a ROI image. For simplicity, the ROI image is directly extracted from the reference as indicated by the white box. Panel (b) depicts the normalized two dimensional cross-correlation function $C(\Delta x, \Delta y)$ in a contour profile plot. The central image shows the resulting values in a false color plot with increasing correlation from blue to red. The two plots above and to the right-hand side are profiles through the false color image in x- and y-direction, respectively. They are centered around the red point which indicates the highest correlation in the image. Panel (c) and (d) depict the two profiles around the highest correlation of $C(\Delta x, \Delta y) = 1$. Here it is important to note that the result of the cross-correlation are discretized by the pixels in the image as represented by the individual dots. The function $C(\Delta x, \Delta y)$ has a maximum at $\Delta x = 140$ and $\Delta y = 187$. These two pixels are exactly the position of the top right point of the ROI in the reference image where it has been extracted.

For our application, we want to track the position of beams in a scaffold over time. Therefore, we compare a series of many frames recorded at discrete time points t. Since we are only interested in displacements relative to the starting point of the experiment at $t = 0$, it is sufficient to calculate

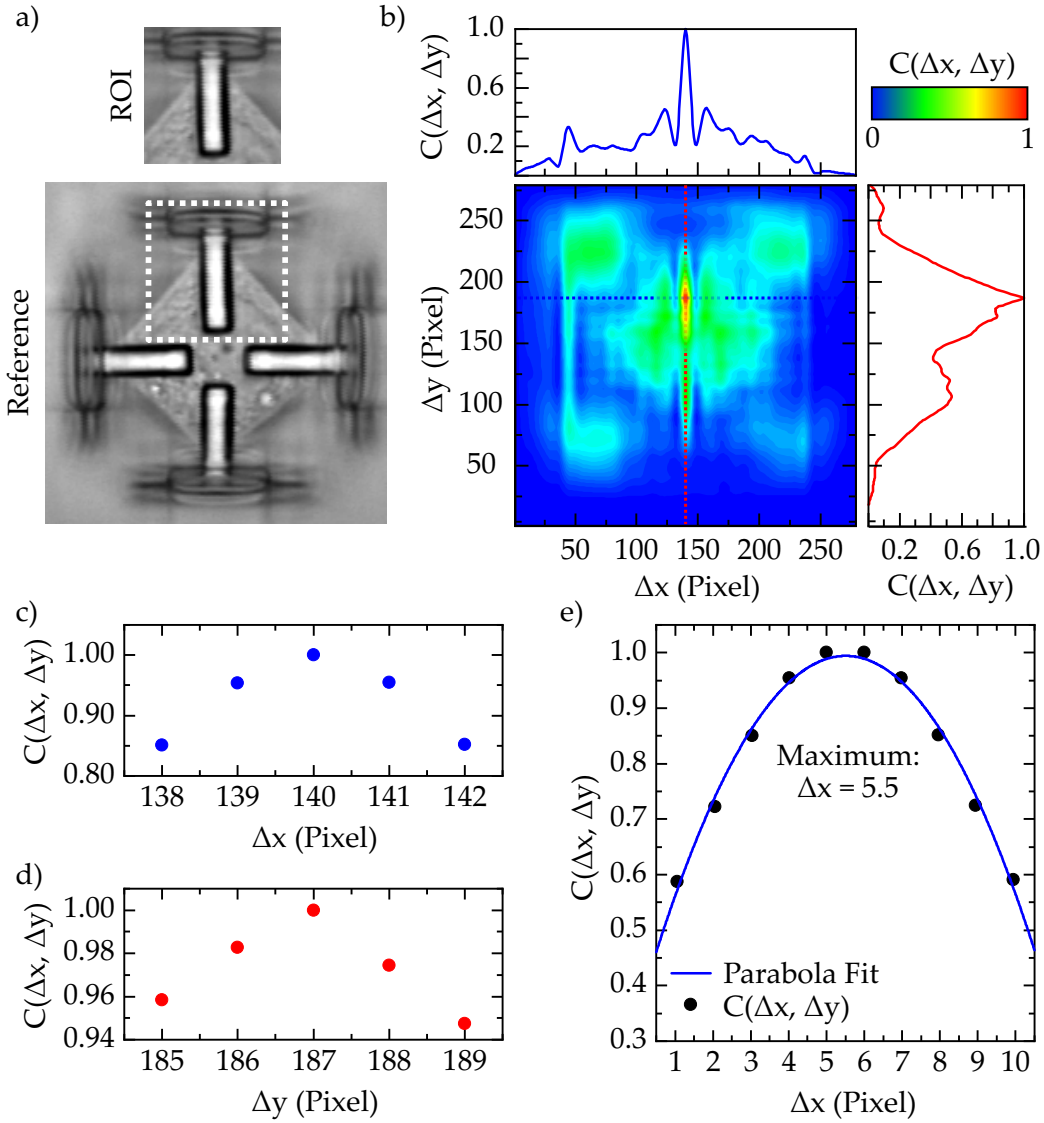

Figure 3.5: Two dimensional image cross-correlation. (a) ROI image which has been extracted from a reference image as indicated by the white box. (b) False-color plot of the normalized cross-correlation function $C(\Delta x, \Delta y)$ of both images with profile plots along x- and y-direction. (c)-(d) Zoom-in of the profile plots close to the maximum correlation value. (d) Exemplary cross-correlation with parabola fit and a maximum between two pixels.

the cross-correlations of all images to the ROI defined in the first frame. The resulting values can again be analyzed to find the displacement vectors for the corresponding time points. Movements of the beam, however, are continuous and not necessarily multitudes of image pixels as in the previous example. But even though the absolute number of pixels and ultimately the achievable resolution of the imaging system is limited, it is yet possible to track features by appropriate fits to the data.

This process is schematically depicted in Figure 3.5(e). The plot shows the results of a cross-correlation discretized by the pixels of the image. One pixel corresponds to 0.195 µm for the parameters used in the image acquisition. Thus, displacements of the observed feature could only be measured in multitudes of these steps. A parabola fit of the data, however, reveals that the maximum of the correlation is actually at position 5.5, exactly between two pixels. Thus, instead of the discretized values of either 0.585 µm (3 pixels) or 0.780 µm (4 pixels) it is possible to calculate the displacement at $\Delta x = 0.683\,\mu\text{m}$ with a much higher accuracy. For the two-dimensional cross-correlation of two images, a 2D parabola is used to fit 3×3 point around the discrete maximum value. With this method it is possible to achieve a significantly higher tracking accuracy compared to the resolution of the optical system which is used to acquire the images. Typical precisions of displacement vectors are at least 1/10 of the image pixels and can even go down to the sub-nm level if noise is sufficiently suppressed and statistics are improved [78].

3.4.1 Tracking of Beam Displacements

To track beam displacements as a function of time, we first calculated the normalized two-dimensional cross-correlation function between the ROI defined in the first image at $t = 0$ and the next image of the time series. Four exemplary optical images of a time series along with the ROI of the right beam are depicted in Figure 3.6. To decrease computational time and increase the accuracy of the results, only a defined region around the initial ROI is compared with the consecutive images. This value is based on the maximum expected displacement between two frames and has to be carefully chosen according to the experiment. Next, a 2D parabola is fitted to the 3×3 points around the discrete maximum of $C(\Delta x, \Delta y)$ to determine the actual maximum with the respective values Δx and Δy for the second image. The resulting displacement vector is now used to update the ROI position before

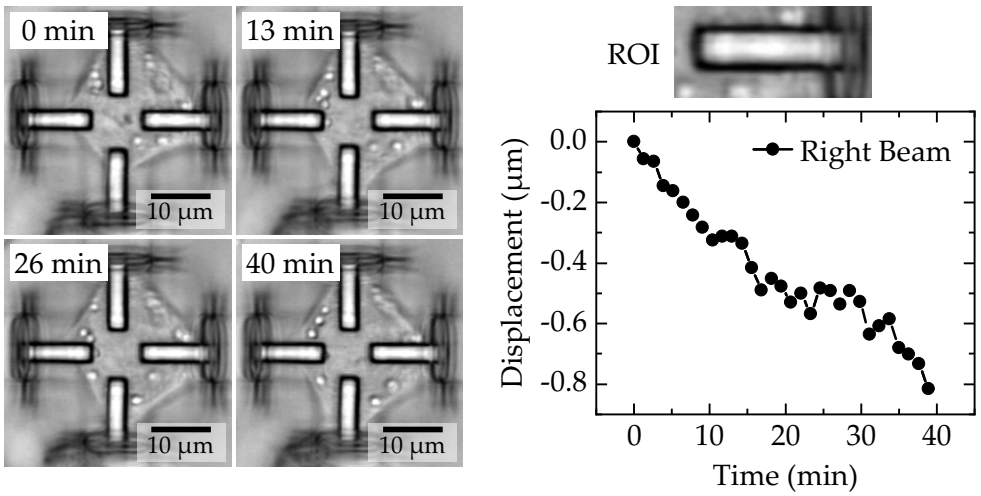

Figure 3.6: Exemplary tracking of the right beam of the scaffold. The ROI shows the selection of the right beam, extracted from the first image at $t = 0$. The optical micrographs correspond to different time points in the track on the right-hand side, obtained by image cross-correlation. The beam displacements between the images are practically invisible for the bare eye but can be tracked accurately by the algorithm.

the cross-correlation is repeated with the next image of the time series. In this way, the region of possible displacements is continuously adapted to enable the tracking of large movements. Typically, we tracked four slightly shifted ROIs for each beam and calculated the average value to further improve the tracking precision.

In the next step, it was necessary to perform a post-processing alignment between individual time points. In the experimental workflow, we record time series of many cells during a single experiment. To achieve this, the mechanical stage of the microscope is programmed to cycle through the respective positions. The re-positioning error of the stage, however, leads to small displacements of the overall images relative to each other which significantly distort the tracking results. To compensate this error, we fabricated additional static markers between the scaffolds. These markers do not move due to the expansion of the stimuli-responsive material or the interaction with cells and can be used to re-align the images with each other. Thus, tracking these markers enabled us to correct all relative displacement caused by the mechanical stage. An exemplary track for the right beam of the depicted scaffold after this correction is shown in Figure 3.6. Since we

are mainly interested in cellular contraction forces, we converted Δx and Δy to a one-dimensional displacement value relative to the center of the scaffold. Here, negative values correspond to a beam which is displaced towards the center of the scaffold. The exemplary track demonstrates how the beam displacement caused by the cellular response can be tracked precisely over the recorded time series. In most of the experiments presented in this thesis, we calculated the overall cellular response and thus the average displacement of all beams. By performing this averaging over the four beams, we effectively subtracted the center of mass of the scaffold and thus implicitly corrected for all external displacements like stage errors.

3.5 Finite Element Calculations

In the scope of this thesis, we applied numerical methods to validate our results, to reveal the underlying mechanisms of the observed effects, and even to predict the outcome of our experiments. In all cases, we applied the finite element method (FEM) in the commercial software COMSOL Multiphysics. A detailed introduction into the technique can be found in literature [80].

The FEM is a numerical approach to solve partial differential equations which describe physical problems like mechanical structural analysis or heat transfer, which can often not be solved analytically. Instead, the complex geometry of the system, e.g., a stimuli-responsive 3D structure, is decomposed into a so-called mesh of small and discrete elements. For the calculations performed in this thesis, we used triangles in 2D systems and tetrahedrons in 3D systems. In the node of each of these simple elements, the partial differential equations are locally approximated by a set of algebraic equations which can be solved analytically. To obtain a solution for the entire geometry, however, additional boundary and continuity conditions between the elements have to be obeyed. Thus, the parameters of the analytical solutions have typically to be found in a numerical iteration procedure. The results of this FEM approach improves in most cases for finer meshes, i.e., a higher number of discrete elements. On the other hand, the computational time significantly increases and a suitable trade-off has to be found. The following two subsections summarize the most important aspects for the application of the FEM method in the respective chapters.

3.5.1 *Thermo-Response of Bi-Material Beams*

In chapter 4, the FEM was applied to study the response of pNIPAM bi-material beams to changes in temperature. Specifically, we used the *structural mechanics* module in COMSOL Multiphysics to solve the linear Cauchy continuum mechanics equations. The temperature-response of the structures was implemented as a volumetric stress and geometrical nonlinearities were accounted for to comprise large bending responses.

We first modeled the simplest case of a bi-material beam with two constituent materials A (less crosslinked) and B (more crosslinked). As introduced in section 3.1.4, these two materials correspond to fabrication laser powers of 30 mW and 37.5 mW at the back focal plane, respectively. As input parameters, we defined the Young's modulus E, the Poisson's ratio ν, and the thermal expansion coefficient α. Since the thermo-response of pNIPAM is highly nonlinear, we only looked at the steady states at 20 °C and 45 °C below and above the lower critical solution temperature (LCST), respectively. Although both material properties can be measured in bulk or larger blocks, the corresponding values for the bi-material beam geometry can differ significantly. Fabrication of two adjacent beams leads to proximity effects and thus complex exposure dose distributions. Moreover, the exposure dose and thus the degree of crosslinking has drastic effects on the material parameters of stimuli-responsive hydrogels as discussed in detail in section 2.2.1.

For this reason, we rather adapted a reverse engineering approach and adjusted the input values for the model in such a way that the results of the numerical calculations closely resembled the corresponding experimental situation. Based on this comparison, we obtained thermal expansion coefficients of $\alpha_A = -1 \times 10^{-2}\,1/\mathrm{K}$ and $\alpha_B = -1 \times 10^{-3}\,1/\mathrm{K}$ and Young's moduli of $E_A = 1\,\mathrm{kPa}$ and $E_B = 11\,\mathrm{kPa}$. The Poisson's ratio was fixed to $\nu_{A,B} = 0.4$ in both cases. For all further calculations with more complex geometries we fixed this set of parameters. In this way, the calculations were able to support the experimental results and provided a powerful tool to predict the structural behavior upon stimulation.

To study the heat dissipation in the photothermal conversion process introduced in section 4.6, we used the *heat transfer* module. We modeled the experimental situation where the base of a bi-material beam is illuminated with a large water bath around it. To save computational time, we chose an adaptive meshing strategy with a fine mesh in the center to sufficiently resolve the details around the central base. In a large distance from the structure, the mesh gets more and more coarse in regions which are less

important for the analysis. The main goal of these calculations was to study the time constants and the effect on adjacent structures which have not been illuminated. Therefore, we fixed the base to a constant temperature of 70 °C to model the photothermal conversion of the absorbed laser light and set the water bath to the room temperature of 24 °C at $t = 0$. The heat transfer from the base to the surrounding water bath led to a gradual temperature increase, which we could reproduce with this numerical approach. To study the cooling period after the laser is switched off, we implemented a new initial situation which corresponds to the last time point of the heating procedure. In this calculation, we lifted the fixed temperature restriction of the central base to allow all heat to dissipate in the water bath. In both cases, we evaluated the temperature profiles after certain time periods and compared the data with our experimental results. The numerical calculation indicate a timescale of 100 ms until the base is sufficiently cooled down (see discussion in section 4.6.2 for details). Here, the numerical calculations provided a deeper insight into the underlying mechanisms of the heat dissipation during photothermal conversion.

3.5.2 Displacements and Forces in Microscaffolds

In the experiments presented in chapter 5, FEM calculations were used to obtain the relation between the experimentally observed beam displacements in scaffolds and the corresponding cellular forces which act on the beams. We used the *structural mechanics* module in COMSOL Multiphysics to model the different material properties as well as the stimuli-responsive behavior upon addition of 1-AdCA.

The scaffolds are composed of three different materials: the bottom layer and walls made of TPETA, the beams made of PETA, and the stimuli-responsive host-guest hydrogel in the center. In a first step, we designed the scaffold in the software and assigned the respective materials to the corresponding parts. To resemble the experimental situation as close as possible, we extracted all geometrical metrics from SEM micrographs instead of the initial fabrication design. Furthermore, we performed AFM nanoindentation experiments (see section A.3) of all involved materials to obtain the Young's moduli $E_{\mathrm{PETA}} = 3 \times 10^6$ kPa and $E_{\mathrm{TPETA}} = 12.7 \times 10^3$ kPa. For the stimuli-responsive host-guest hydrogel, we differentiated between the stiff state $E_{\mathrm{hydrogel}} = 22$ kPa and the soft state $E_{\mathrm{hydrogel}} = 6.5$ kPa.

The hydrogel swelling was modeled as a boundary load on the outer surfaces of the block. The bottom surface was in turn fixed to the substrate to account for the covalent bonds between the hydrogel and the silanized glass surface. After the initial fabrication, the block is not in direct contact with the TPETA walls. During the development, however, the hydrogel block expands and already exerts a small pressure on the walls. Upon stimulation with the competitive guest molecule 1-AdCA, the hydrogel expands even further and bends the walls towards the outside. We implemented this dynamic between hydrogel and wall as a penalty contact which exerts a pressure if one mesh starts to penetrate into another one. The contact pressure penalty factor of $8 \times 10^{11}\,\mathrm{N/m^3}$ was chosen according to the experimental observations. Since the calculation of this penalty is computationally expensive, we exploited the symmetry axes of the system and limited the calculation to one quarter of the scaffold. This method enabled us to model the bending of the TPETA walls and thus the displacement of the PETA beams on top as a function of the hydrogel swelling.

Next, the swelling was fixed at the new equilibrium level. At this point we activated an additional force which acts on the PETA beams and points towards the center of the scaffold to mimic a cell which pulls on the beams. We gradually increased this force and calculated the new steady state position of the beam for every data point. In this way, we obtained the relation between displacements and cellular forces which were required to calibrate the scaffolds for the biological experiments. Importantly, the resulting relation did not significantly depend on the initial bending of the TPETA walls due to the hydrogel swelling. As a consequence, we were able to apply the same conversion factor regardless of the initial stretch.

3.6 Cell Biology

To perform the biological experiments in chapter 5, it was necessary to maintain various cell lines in culture, to seed them on the fabricated scaffolds, and to fix and stain them after the experiments. This work was performed by Dr. Kai Weißenbruch and Kai Richler, both from the group of Prof. Dr. Martin Bastmeyer at the Karlsruhe Institute of Technology. In this section, I first list the cell types we used for our experiments and discuss the culture conditions in general. In the second part, I introduce the protocols we used for the fixation and staining of cells inside the stimuli-responsive scaffolds.

Table 3.1: Overview of the four different cell types used in the scope of this thesis.

Cell-line	Background	Origin
NIH 3T3	Mouse embryonic fibroblasts	ATCC #CRL-1658
U2OS WT	Isolated from human bone osteosarcoma with epithelial phenotype	ATCC #HTB-96
U2OS NM2A-KO	Generated knock-out cell-line from U2OS WT cells, deficit of NM2A	Kai Weißenbruch [42]
U2OS NM2B-KO	Generated knock-out cell-line from U2OS WT cells, deficit of NM2B	Kathrin Stricker [83]
U2OS-TagGFP-Actin	U2OS cell expressing TagGFP labeled β-actin	Marinpharm GmbH

3.6.1 Cell Lines and Cell Culture

In the scope this thesis, we used five different immortalized cell lines which can be kept in culture for an unlimited period of time. An overview over the different cell lines is listed in Table 3.1. NIH 3T3 cells are are originally derived from mouse embryos and have fibroblast characteristics. Fibroblasts are the most common cells of connective tissue in animals and play a critical role in processes like wound-healing. U2OS cells, on the other hand, are isolated from human bone tissue and posses an epithelial character. Epithelial tissues cover the outer surfaces of organs and blood vessels in the body with functions like secretion, protection, and sensing. U2OS cells have a polarized phenotype and a distinct actin cytoskeleton which makes them a model system for the investigation of stress fibers [81, 82]. For this reason we used them in the majority of the biological experiments presented in chapter 5.

We further used three variations of the U2OS WT cells. U2OS NM2A-KO cells are a stable knock-out cell line without the protein NM2A which plays an important role in the generation of contraction forces in cells (see section 2.3.2 for details). This cell line was generated by Dr. Kai Weißen-

bruch by manipulation of the genomic DNA of the target gene with the CRISPR/Cas9 system. Details about the generation procedure as well as the characterization of these cells can be found in his PhD thesis [42]. Similarly, U2OS-NM2B-KO cells lack the isoform NM2B and were generated by Kathrin Stricker [83]. The commercially available U2OS-TagGFP-Actin cell-line is stably transfected with Tag-GFP-Actin. This fluorescent marker labels the human β-actin and makes it possible to perform live cell imaging of the actin cytoskeleton as demonstrated in section 5.9.

All cells were cultured in sterile conditions in a bactericidal incubator at 37 °C with 5 % CO_2 and 98 % humidity. They were passaged three times per week in Dulbecco's modified eagle's medium (DMEM) supplemented with 10 % bovine growth serum. Cells were washed with PBS and treated with 200 µl trypsin and ethylenediaminetetraacetic acid (EDTA) to remove adherent cells from the culture flasks. After 2-3 minutes of incubation time, medium containing serum was added to stop the reaction. The remaining trypsin/EDTA was removed by centrifugation of the suspension at 1000 rpm and the cells were subsequently transferred to new medium.

To functionalize the scaffolds, samples were coated with human plasma derived fibronectin at a concentration of 10 µg/l for 1 h at room temperature. For our experiments, cells were kept in phenol red-free high glucose DMEM containing 25 mM HEPES buffer and supplemented with 10 % bovine growth serum. We typically seeded about 2×10^5 cells on one sample fixed in the microfluidic chamber (see section 3.3) and kept them in the incubator for 3 h. Afterwards we transferred the sample to the incubation chamber in the microscope heated to 37 °C and waited another 30 min before the image acquisition was started. To trigger the hydrogel expansion and thus the mechanical stretch, the medium was completely replaced by medium containing additionally 20 mM of 1-AdCA. Since addition of 1-AdCA to the cell culture medium leads to a significant decrease of the pH value, we prepared the medium in advance and adjusted the pH to 7.0 by addition of NaOH. Furthermore, the solubility of 1-AdCA strongly depends on the pH value and 20 mM can only be solved after continuous adjustments.

3.6.2 Fixation and Staining

To observe the actin reorganization and myosin distribution in cells we followed a fixation and staining protocol. In the first step, we fixed cells by addition of 4 % paraformaldehyde in PBS with 20 mM 1-AdCA. The

Table 3.2: Overview of the staining targets and the respective labels.

Target	Label
NM2A	Primary antibody: rabbit-anti NMHC 2A (BioLegend, Dilution 1:500) Secondary antibody: goat anti-rabbit-Cy3 (Jackson Immunoresearch, Dilution 1:200)
Actin	Phalloidin-Alexa Fluor 488 (Life technologies, Dilution: 1:200)
Cell nucleus	DAPI (Carl Roth, 1:1000)

competitive guest was added to all further solutions to keep the hydrogel expanded and thus maintain the cells in the stretched state. In the next step, cells were washed and permeabilized in PBS containing 0.1 % Triton-X 100 and 20 mM 1-AdCA. This solution was also used for all further washing steps between immunocytochemical labelings. A summary of targets we stained in our experiments along with the respective labels is listed in Table 3.2. All staining steps were performed in a solution containing 1 % BSA in PBS and 20 mM of 1-AdCA. To keep the scaffolds in the stimulated state, all samples were stored and imaged in PBS containing 20 mM of 1-AdCA. Consequently, we also used a $40\times$, NA $= 1.2$ water immersion objective for the image acquisition to minimize focus distortions due to unmatched refractive indices.

Chapter 4

4 Stimuli-Responsive pNIPAM Microstructures

Poly(*N*-isopropylacrylamide) (pNIPAM) is a stimuli-responsive polymer which exhibits drastic changes in its properties around a temperature close to the body temperature of 37 °C. For this reason, pNIPAM based hydrogels have been reported in numerous applications, especially in the biomedical field. Prominent examples are drug release [84, 85], switchable surfaces for cell adhesion [86], and soft robotics [87]. Several reviews discussing the various research areas can be found in literature [88–90].

Depending on the application, various fabrication techniques are employed. In the case of surface coatings it is sufficient to completely cover the substrate via spin-coating [91] or graft pNIPAM chains by thermally initiated radical polymerization [92]. Most applications, however, demand structure on the surface, e.g., patterns with and respectively without pNIPAM. In this case, thermal initiators are replaced by photoinitiators which start the radical polymerization upon illumination with the respective wavelength. A suitable photomask enables the patterning with a high lateral resolution [93]. A typical example from the biomedical field is the release of cells only from certain areas on the substrate which were covered with pNIPAM [94].

For yet more sophisticated applications it is necessary to extend the design to the third dimension. An interesting approach still based on 2D fabrication are material sheets which can fold to 3D structures like grippers or actuators [95]. Even though the 2D patterning offers a large-scale fabrication, design options for structures are rather limited. In contrast, additive manufacturing approaches like stereolithography offer much more flexibility and have successfully achieved large thermo-responses of 3D pNIPAM structures [96]. This technique, however, is restricted to the macroscopic regime and promising applications in microfluidics, microscopic actuators or cell biology

remain inaccessible. First attempts to transfer these approaches to the microscopic regime have already been undertaken [13, 97], but the structures still remain rather simple demonstrations and do not exploit the full potential offered by stimuli-responsive pNIPAM. Thus, the next crucial step is the establishment of complex pNIPAM 3D microstructures with strong, directed responses. Such structures can enable the transition towards applications in research fields like soft-robotics which could vastly benefit from the introduction of stimuli-responsive systems [10].

In this chapter, I present our results on stimuli-responsive 3D microstructures based on pNIPAM. First, I describe the photoresist composition and the initial material characterizations via atomic force microscopy. Subsequently, experimental results on the application of pNIPAM valves in microfluidic systems are shown. In section 4.4, I introduce a method based on gray-tone lithography to fabricate hetero-microstructures from a single resist with vast possibilities to design complex thermo-responses. These results are complemented by numerical calculations in section 4.5 with potential to predict the responsive behavior. Finally, I discuss our results on the local stimulation by two-photon absorption of focused light. Unless specifically stated, all experiments presented in this chapter have been carried out by me.

4.1 Lower Critical Solution Temperature of pNIPAM

Poly(*N*-isopropylacrylamide) (pNIPAM) is a thermo-responsive polymer which is hydrophilic at room temperature but hydrophobic above a lower critical solution temperature (LCST) of around 33 °C [98]. This behavior was first described in 1967 [99] and one year later characterized in more detail [100]. Both cited groups used cloud point measurements to study the precipitation of pNIPAM chains in aqueous solutions. About 20 years later researchers also started to investigate gels of crosslinked pNIPAM chains [101]. These hydrogels undergo large discontinuous volume changes when heated up above the LCST. The polymer has attracted a lot of interest until today, because the observed transitions are abrupt and large and the LCST is close to the body temperature, making applications in the biological and biomedical field especially interesting [89]. In the following section, I discuss the behavior of pNIPAM from a thermodynamic viewpoint by considering the Gibbs free energy upon mixing of polymer and water. First, I explain the underlying mechanisms of polymer chains in solution and afterwards the implications on crosslinked hydrogels.

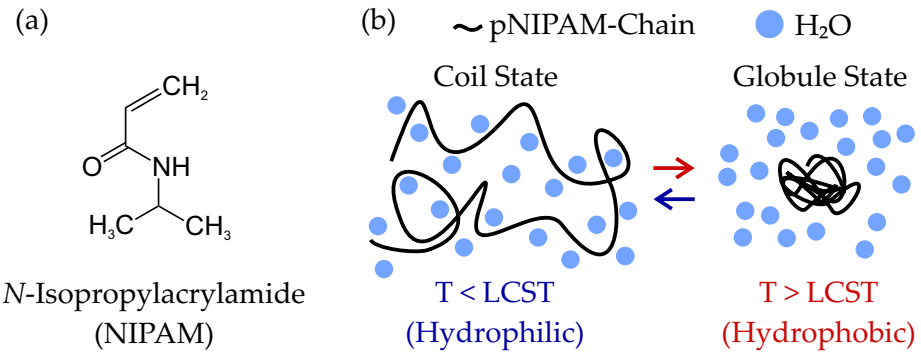

Figure 4.1: Temperature responsivity of pNIPAM chains. (a) Chemical structure of NIPAM. (b) Schematic depiction of pNIPAM coil and globule states below and above the LCST, respectively.

4.1.1 *Coil-to-Globe Transition of Polymer Chains*

Polymer chains of pNIPAM are typically synthesized by radical polymerization of NIPAM [98]. These chains are soluble in aqueous solutions because water molecules form bonds with the polymer, leading to a negative, exothermic enthalpy ΔH. However, the monomer NIPAM (see Figure 4.1(a)) has polar as well as nonpolar regions. In order to form hydrogen bonds, water molecules must reorient around the respective polar regions which leads to a negative entropy ΔS upon mixing [102]. Both effects form a delicate balance which tips in either direction depending on temperature. In a chemical equilibrium, the Gibbs free energy ΔG defined as

$$\Delta G = \Delta H - T\Delta S \tag{4.1}$$

is minimized [103]. At room temperature, ΔG is negative because the enthalpy term ΔH dominates. Thus, reordering of the water molecules to form hydrogen bonds is thermodynamically favorable. Once the temperature increases, however, the entropy term $-T\Delta S$ gets more important and eventually ΔG becomes positive. The consequence is phase separation above a specific temperature, termed as the lower critical solution temperature (LCST).

The thermodynamic view explains the abrupt transition at the LCST but does not give insights in the level of individual polymer chains. This microscopic behavior has been thoroughly studied experimentally [104] and was also confirmed by numerical calculations [105]. The underlying

mechanism is based on a coil-to-globe transition, as schematically depicted in Figure 4.1(b). Below the LCST, the polymer chain is coiled and has formed hydrogen bonds with the surrounding water molecules. Above the LCST, phase separation occurs and it is energetically favorable to form a tight globe. Importantly, this process is completely reversible, i.e., the pNIPAM chain returns to the coil state as soon as the temperature drops again below the LCST. The resulting LCST of pNIPAM is around 33 °C but depends on the exact microstructure of the macromolecules [98].

4.1.2 Volume Change in Crosslinked Hydrogels

When a crosslinker is added to the polymerization procedure, pNIPAM chains are linked together and stable hydrogels are formed. This is schematically depicted in Figure 4.2 with crosslinks indicated as green dots. The polymer network can take up to 90 % water at room temperature by formation of hydrogen bonds [106]. When the temperature is increased above the LCST, the same considerations regarding hydrophobicity and hydrophilicity as in the previous sections apply. In this case of hydrogel network, however, the crosslinks anchor the polymer chains to each other and prevent the transition to compact globules. As a result, each segment of the pNIPAM chains between two crosslinks partially curls up and water is expelled from the network. This leads to an isotropic shrinkage of the hydrogel. When the temperature is decreased, water again penetrates the network to form hydrogen bonds and the hydrogel expands to its initial state. Thus, this effect is completely reversible and can be precisely controlled as a function of temperature. Even though there is some controversy over the classification in hydrophilic and hydrophobic [107], I use these terms for simplicity in the rest of this work to describe the two pNIPAM states below and above the LCST, respectively.

It is important to note that the changes in volume are accompanied by changes in the mechanical properties. At room temperature, the hydrogel is in the hydrophilic state and has taken up significant amounts of water. As a result, the polymer network is expanded and mechanically soft. In contrast, shrinkage of the hydrogel above the LCST leads to a compact and mechanically stiff polymer network with little water inside.

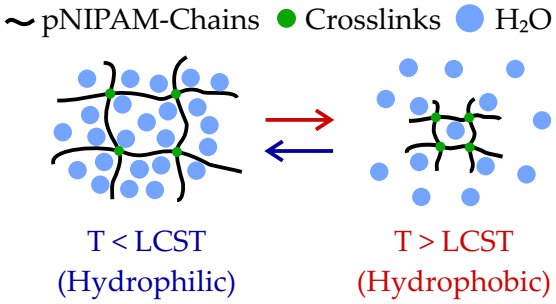

Figure 4.2: Schematic image of the hydrophilic and hydrophobic hydrogel states below and above the LCST, respectively. In the transition to the hydrophobic state, water is expelled from the system and the polymer network shrinks and stiffens.

4.2 3D Laser Lithography of pNIPAM Microstructures

So far, I have discussed the general mechanism of the thermo-response as well as its implications on the material parameters. Based on these considerations, we developed a photoresist which can be used in 3D laser lithography to fabricate sophisticated 3D pNIPAM microstructures. In this section, I first introduce the photoresist composition with its main components and discuss their impact on the resulting material. In the second part, I show our results of the mechanical characterization of fabricated microstructures to determine volume changes as well as changes of the Young's modulus.

4.2.1 Photoresist Composition

The first step towards the fabrication of pNIPAM microstructures via 3D laser lithography is the development of a suitable photoresist. Here, three main components are required: NIPAM as the stimuli-responsive monomer, *N*,*N*'-Methylenebisacrylamide (Mbis) as a crosslinker, and lithium phenyl-2,4,6-trimethylbenzoylphosphinate (LAP) as a two-photon photoinitiator. The corresponding recipe for the preparation can be found in section 3.1.3.

The crosslinker Mbis is a crucial component in the system since it generates connections between pNIPAM chains which are necessary to form stable hydrogels. For the bulk polymerization of pNIPAM gels, only small amounts of this crosslinker are necessary and the impact on the resulting thermo-response is limited. To fabricate complex and yet stable 3D structures, however, it is necessary to add a significant portion of Mbis to the

photoresist, leading to substantial changes in the material parameters [108, 109]. The general mechanism for different types of stimuli-responsive hydrogels is discussed in section 2.2.1 in more detail. In the case of pNIPAM, the thermo-response is strongly reduced if more crosslinks are present in the polymer network. As a result, the fabrication properties and the functionality are directly connected to each other which has positive and negative implications that I discuss in the following sections.

The third important ingredient is a two-photon photoinitiator. Since hydrogels like pNIPAM are based on aqueous environments, typical efficient candidates like the Irgacure series [110] are unsuitable due to their limited water-solubility. Research in the field of water soluble two-photon initiators has only been evolving in the last two decades [27] due to increasing interest in 3D laser lithography for biological applications [111] and only recently, first suitable products have been made commercially available. Here, LAP turned out to be an ideal candidate for our purpose due to its superior water solubility in combination with a high two-photon efficiency at the fabrication wavelength of 780 nm [30]. Furthermore, the cytotoxicity of this initiator is low, which is an important aspect for applications in the biological and biomedical area [30].

We additionally added acryloxyethyl thiocarbamoyl rhodamine B (RhodB) as a fluorescent dye to the photoresist. Due to its acrylate group, it is included in the hydrogel network and enabled us to record 3D fluorescence image stacks of the fabricated pNIPAM structures. All components were solved in ethylene glycol to maximize the portion of polymerizable material which is beneficial for the fabrication properties. We used this photoresist in a commercial Photonic Professional GT system (Nanoscribe GmbH, see section 3.1.1) for the fabrication of all pNIPAM structures in this chapter.

4.2.2 Material Characterization via AFM

Although NIPAM is well known and characterized, the thermo-responsive properties of crosslinked gels are highly dependent on the exact composition and polymerization procedure [108, 109]. Thus, we used atomic force microscopy (AFM) to determine the mechanical properties of the resulting material from our photoresist as a function of temperature. Since pNIPAM is a hydrogel, all experiments were performed in an aqueous environment

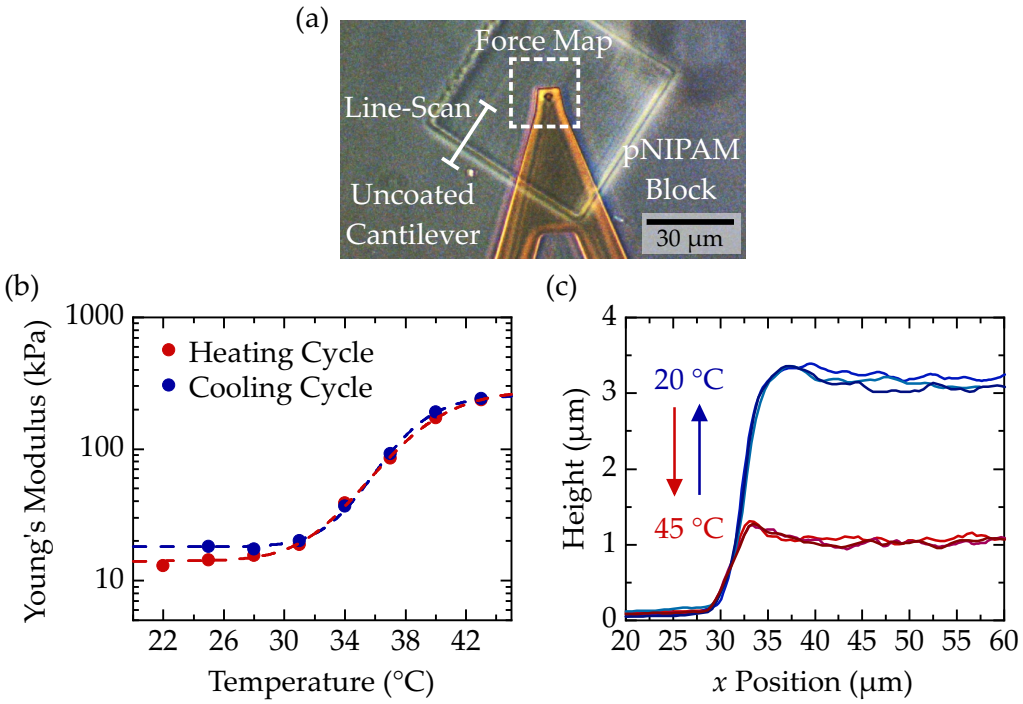

Figure 4.3: Characterization of pNIPAM material properties. (a) Optical image during an AFM experiment with overlaid markers, indicating the positions of force measurements and line-scans. (b) Young's modulus as a function of temperature measured via AFM nanoindentation. The heating from 22 °C to 43 °C and the cooling back to room temperature are depicted in red and blue, respectively. (c) Measurement of the block height via line-scanning from the glass substrate on top of the pNIPAM block. Several cycles of heating and cooling are depicted in red and blue colors, respectively. Adapted from [33].

and non-coated cantilevers were used to avoid bending effects similar to bimetallic stripes during heating or cooling. Further details about the characterization setup and materials are discussed in section 3.2.

We applied 3D laser lithography to fabricate $50 \times 50\,\mu m^2$ blocks with a nominal height of 3 µm as shown in the bright-field optical image in Figure 4.3(a). The Young's modulus as a function of temperature was obtained via nanoindentation measurements in the center of the block, as indicated by the dashed white square. First, the sample was heated from room temperature at 22 °C to 43 °C in steps of 3 °C. At each step, the Young's modulus was calculated as an average of 64 individual data points, summarized as red dots in Figure 4.3(b). By increasing the temperature above

the LCST of pNIPAM, the hydrogel gradually transitions from hydrophilic to hydrophobic and water is expelled from the polymer network (see section 4.1.2 for details). As a result, the hydrogel stiffens and the Young's modulus increases by over one order magnitude from $\approx$ 15 kPa to $\approx$ 300 kPa with the strongest thermo-response between 30 °C and 40 °C. This transition is significantly broader compared to the abrupt change around the LCST in measurements with pure pNIPAM. Furthermore, the measured LCST at around 35 °C is shifted towards higher temperatures. Both effects can be attributed to crosslinks in the polymer network formed by addition of Mbis [108, 109]. In a second step, we cooled the sample down to room temperature and repeated the Young's modulus measurements in the same intervals. The resulting blue data points show a very good agreement compared to the heating, demonstrating the complete reversibility of the material within measurement errors. The following images in this chapter are recorded at 20 °C and 45 °C to capture the experimental conditions below and above the LCST, respectively.

As discussed in section 4.1.2, stiffening of the material as a result of the expelled water is accompanied by shrinkage of the polymer network. To study this effect on the fabricated microstructures, we used AFM to perform line-scanning experiments from the glass substrate to the top of the block, as indicated in Figure 4.3(a). The results are summarized in Figure 4.3(c) with three consecutive cycles between 20 °C and 45 °C in shades of blue and red, respectively. Increasing the temperature above the LCST leads to a shrinkage of the hydrogel block by a factor of three, down to a height of about 1 µm. When the temperature is decreased again, the hydrogel re-swells to its initial height, again demonstrating the reversibility of the process. In this experiment we only observe significant changes in the axial direction, although the swelling or shrinkage is generally isotropic. The reason is the anchoring of the hydrogel block to the glass substrate by silanization (see section 3.1.2 for details), which restricts lateral volume changes close to this interface.

In summary, the material parameters of pNIPAM structures obtained from 3D laser lithography can be drastically altered by changes in temperature around the LCST of about 35 °C. Especially in the interval between 30 °C and 40 °C, even small temperature changes lead to significant effects on the Young's modulus and the volume of the hydrogel.

4.3 Stimuli-Responsive Microfluidic Valves

3D laser lithography is a versatile technique that readily allows the combination of different photoresists to fabricate several materials in a sequential process [112–114]. This is particularly interesting for stimuli-responsive polymers since it enables the combination with conventional, non-responsive structures. Furthermore, pNIPAM hydrogels are typically soft with Young's moduli in the order of 1–100 kPa [115], thus limiting their application if rigid materials are required. As an example with two different materials, we realized a micrometer-scale channel with a responsive valve to tune the open channel area as a function of temperature.

Figure 4.4(a) shows the experimental results of microfluidic valves in 3D reconstructions, obtained via laser scanning microscopy (LSM). In a first step, we fabricated channels with a common photoresist based on pentaerythritol triacrylate (PETA, colored in turquoise). The photoresist composition is described in section 3.1.3. Additional alignment markers were placed on the substrate to enable the lateral positioning during the second writing procedure. Axial alignment was achieved with the built-in interface finder of the setup. After development of the sample, the pNIPAM photoresist was applied and we fabricated the valves as a torus (colored in gray) at the inner wall of the tube. Here, the pNIPAM is covalently attached to the PETA tube since unreacted acrylate groups are still available at the polymer surface.

Fluorescent image stacks were recorded at 20 °C and 45 °C to study the stimuli-response of the valves. To heat and cool our samples inside the LSM to the desired temperatures, we designed a chamber with a Peltier element and a respective controller (see section 3.3 for details). The pNIPAM torus is swollen at room temperature, leading to a small opening in the middle of the channel. When the sample is heated above the LCST, the torus shrinks and the opening widens significantly. Importantly, the tubes fabricated with the PETA resist remain unchanged during this process. Figure 4.4(b) displays a quantification of the open channel area, which increases by more than a factor of 2.5 upon stimulation. Furthermore, over ten cycles of heating and cooling the response of the valve is reversible within measurement errors.

Figure 4.4(c) depicts an alternative design with an additional inner PETA tube and a second pNIPAM torus surrounding it. Both tori are in contact in the swollen state at room temperature, thus closing the microchannel completely. By increasing the temperature, the hydrogel shrinks and the

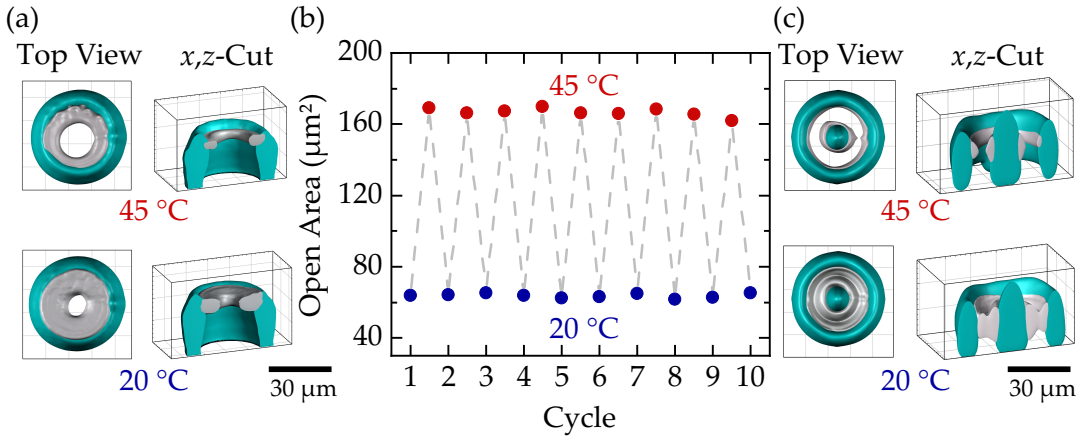

Figure 4.4: Stimuli-responsive microfluidic valves. (a) 3D reconstructions of fluorescent image stacks obtained by confocal laser scanning microscopy. Microchannels were fabricated with PETA and the green fluorescent photoinitiator DETC and valves with pNIPAM and a red fluorescent rhodamine dye. The corresponding iso-intensity surfaces are colored in turquoise and gray, respectively. In the transition from 20 °C to 45 °C the pNIPAM valve shrinks and the opening in the center widens. (b) Corresponding open area in the center of the microchannel for multiple stimulation cycles without significant deterioration. (c) 3D reconstructions of an alternative design with an inner PETA tube. Two pNIPAM tori attached to the respective surfaces enable the complete and reversible closure of the microchannel. Adapted from [33].

microchannel can be opened. Both designs also allow continuous tuning of the channel opening for different temperatures with the strongest response between 30 °C and 40 °C as discussed in section 4.2.2.

4.4 Hetero-Microstructures from a Single Resist

In the previous section, I have discussed the combination of responsive and non-responsive photoresist systems as well as an application with microfluidic valves. The introduced approach, however, has two major drawbacks. First, the pNIPAM hydrogel swells and shrinks isotropically. However, for more complex applications like actuators or grippers, a directional response is required. Second, the sequential fabrication procedure renders the process not only slow but also imposes strict limits on the design options. To fabricate, e.g., multi-material structures with several alternating layers in the axial direction, multiple development and re-alignment steps are necessary [116].

If stimuli-responsive hydrogels like pNIPAM are involved, this sequential approach is even more challenging because the structures have to be kept in an aqueous environment after development. To overcome these limitations, we established a different approach based on gray-tone lithography to fabricate hetero-microstructures with strong, directional responses from a single photoresist.

4.4.1 Directed Response of Bi-Material pNIPAM Beams

The term gray-tone lithography implies the gradual change of material parameters by varying the exposure dose during fabrication [39]. The general method and especially its implications on systems with stimuli-responsive hydrogels are discussed in detail in section 2.2.1. The two main components of the pNIPAM photoresist in this chapter are the stimuli-responsive monomer NIPAM as well as the non-responsive crosslinker Mbis, which is necessary to form a stable polymer network (see section 4.2.1). A denser polymer network contains more crosslinks which reduce the responsivity and make the network more rigid at the same time. However, since the network density can be actively controlled by variation of the exposure dose, this effect can be exploited to tune the stimuli-response of the structures during the fabrication procedure. Combined with the advantages of 3D laser lithography, this offers the ability to program the responsivity in 3D microstructures with high spatial control.

With this technique, we were able to fabricate multi-material microstructures as depicted in Figure 4.5(a) from a single photoresist. Details of the fabrication procedures as well as the writing strategy are discussed in section 3.1.4. A bi-material beam is attached to a central pillar which is anchored to the glass substrate. The rendered image in the back shows the schematic design of the beam with two different materials in green (lower crosslinking density) and gray (higher crosslinking density). The two structures in front are the corresponding 3D reconstructions of experimental data, obtained by LSM. This configuration exploits the bi-material effect, where two materials with different responsivities are in contact with each other [117]. When the temperature is increased from $T = 20\,^{\circ}\mathrm{C}$ to $T = 45\,^{\circ}\mathrm{C}$, the green material with the lower crosslinking density and thus larger thermo-response shrinks significantly. In contrast, the gray material with the smaller thermo-response only shows a minor change after the stimulation. Since both materials are connected at the interface, the beam considerably bends to the left-hand side.

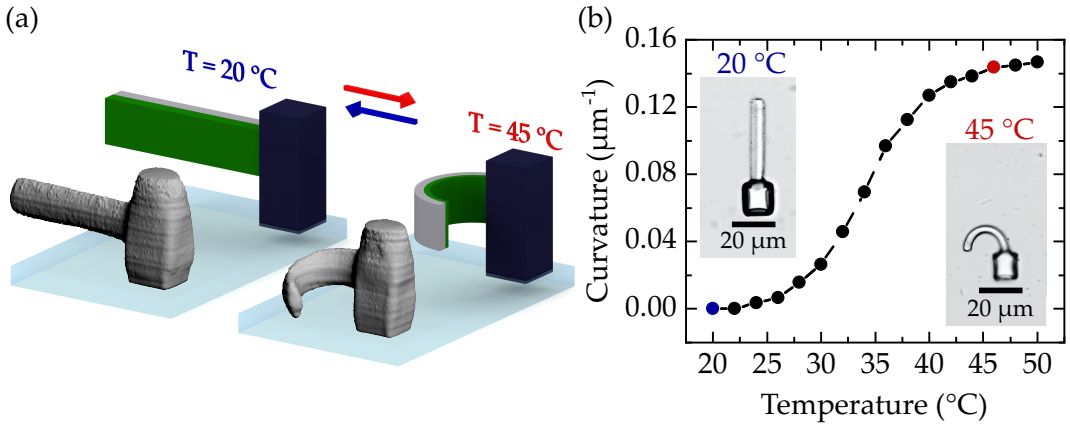

Figure 4.5: Bi-material hetero-microstructures based on pNIPAM. (a) Back: schematic of bi-material beam structures, fabricated with lower (green) and higher (gray) exposure dose. Front: corresponding 3D reconstructions obtained from fluorescence image stacks measured by LSM. The beams significantly bend after the transition from $T = 20\,°C$ to $T = 45\,°C$. (b) Curvature of the depicted bi-material structure versus temperature, obtained by circles fitted to the experimental data. The two optical images correspond to the highlighted data points. Adapted from [33].

This architecture allowed us to transfer the isotropic swelling and shrinkage of the hydrogel to a directional response, thus opening new possibilities for more sophisticated applications.

In the next steps, we characterized this response in more detail. Figure 4.5(b) shows the quantification of the curvature, i.e., inverse radius of the beams, as a function of temperature. The two insets display optical images for the respective highlighted data points at 20 °C and 45 °C. At room temperature, the two segments of the beam become apparent with the lower and higher crosslinking density on the left and right side of the beam, respectively. The less crosslinked beam takes up more water and therefore has a weaker optical contrast due to the reduced refractive index difference with the surrounding media. To quantify the bending, we fitted circles to the optical images for each temperature point and calculated the curvature. Clearly, the response of this hetero-structure shows the same trend compared to the homo-structures in Figure 4.3(b) with the strongest response between 30 °C and 40 °C and a corresponding LCST in between of around 35 °C.

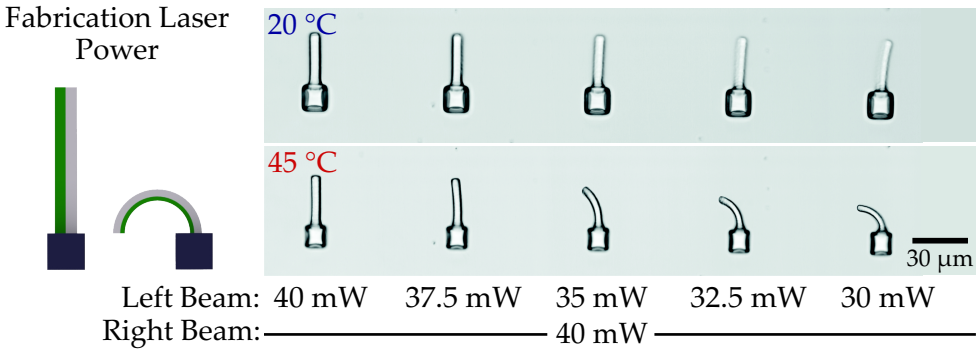

Figure 4.6: Gray-tone lithography of bi-material beams. The structures are fabricated with varying exposure doses for the left (green) and right (gray) side, as indicated on the bottom. By increasing the difference in exposure dose between the two sides of the beam, the difference in temperature-response also gradually increases and the bending to the left-hand side is more pronounced. Adapted from [33].

4.4.2 *Continuous Parameter Tuning*

As the term "gray" already implies, the fabrication is not limited to two materials with the binary choice between low and high crosslinking densities. It is rather possible to continuously tune the responsivity as a function of exposure dose and thus access a multitude of materials with different properties. To demonstrate this aspect, we fabricated five bi-material structures with different exposure doses next to each other, as depicted in Figure 4.6. The labels below indicate the respective fabrication laser powers for the left and right beam of each structure. We fixed the laser power at 40 mW for the right beam (gray) and gradually decreased it from 40 mW to 30 mW for the left beam (green). The fabrication speed was fixed to 1 mm/s for all experiments. The results can bee seen in the optical images recorded at 20 °C and 45 °C.

The first structure on the left side was fabricated with equal laser powers for both beams. Increasing the temperature to 45 °C leads to an isotropic shrinkage of all parts of the structure. As a result, the thickness of the bi-material beam decreases but no bending to either side is observable. Moreover, even the isotropic shrinkage is relatively weak because of the small thermo-response for high exposure doses. This behavior drastically changes when the difference in exposure dose between the two sides of the

beams increases towards the right-hand side of the image. The left side of the beams gets gradually more responsive, significantly shrinks above the LCST, and pulls the whole bi-material beam to the left-hand side.

At this point it is important to highlight that the difference between material properties is responsible for the bending and not the absolute values. A bi-material structure fabricated with 30 mW on both sides indeed shows a large thermo-response and thus a significant isotropic shrinkage, but still no bending. Consequently, to achieve a strong bending one aims to make the difference in responsivity between both beams as large as possible. At the same time, boundary conditions of the fabrication process like the polymerization thresholds and general stability of structures limit the available parameters. The data in Figure 4.6 depicts only a small fraction of the available parameter space which was analyzed. Ultimately, we found laser powers of 37.5 mW and 30 mW for the weak and strong crosslinking density, respectively, as the best compromise between structural stability and a strong directional thermo-response. The base for the bi-material beam was fabricated with a laser power of 40 mW to obtain a good stability and small response. These parameters were fixed for the remaining experiments in this chapter, but it is also possible to combine several bi-material structures with different behaviors to achieve a desired stimuli-response.

4.4.3 Robust and Reversible Response

A crucial step from mere demonstrations towards actual applications is the reliable control over the stimuli-response, which includes two important aspects that have to be fulfilled. First, nominally identical structures have to respond in the same way, i.e., the fabrication process has to be reproducible and robust. To validate this aspect we studied 3×3 bi-material structures during changes in temperature as depicted in the optical images in Figure 4.7(a). The beams are straight at room temperature and all of them show the same distinct bending towards the left-hand side when the sample is heated to 45 °C. Second, the behavior of the structure has to be reversible and thus independent of previous stimulations. We quantified this aspect in Figure 4.7(b) by measuring the curvature of the beams for twelve consecutive heating and cooling cycles. The results illustrate the complete reversibility of the process with no deterioration, similar to the homo-structures discussed in section 4.3.

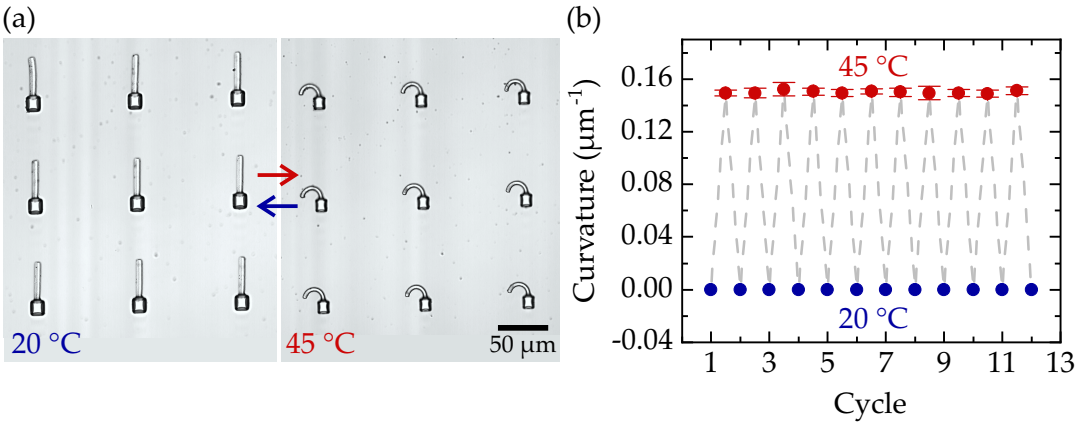

Figure 4.7: (a) Bright-field optical images of 3×3 nominally identical bi-material structures. The indistinguishable temperature responses demonstrate the reproducibility of this approach. (b) Measured curvature (inverse radius) for twelve heating and cooling cycles between 20 °C and 45 °C with no deterioration. The data shows average values of multiple measurements with standard deviations. Adapted from [33].

4.4.4 *Influence of Beam Geometry*

To achieve maximum control over the response it is mandatory to study not only the material properties but also effects of the beam geometry. Here, particularly the aspect ratio has a significant impact on the bending, as one expects based on the comparison to bimetallic stripes [117]. Figure 4.8 shows optical images from bi-material structures with different beam lengths L from 30 µm to 60 µm as well as an extreme case of $L = 120$ µm. These long beams are initially bent towards the right-hand side (more crosslinked) at 20 °C. This effect can be attributed to the development in water after fabrication. During this step, the sample is transferred from the photoresist based on ethylene glycol to the developer solution. Water, however, is a slightly better solvent for the polymerized hydrogel. Furthermore, the different crosslinking densities between the left and right side of the beam lead to different degrees of swelling. As a result, the less crosslinked side (left) undergoes a stronger expansion which leads to the slight bending of the bi-material beam to the right-hand side at room temperature. This effect is already visible for small beam lengths (see also Figure 4.6) but becomes more pronounced if the aspect ratio increases.

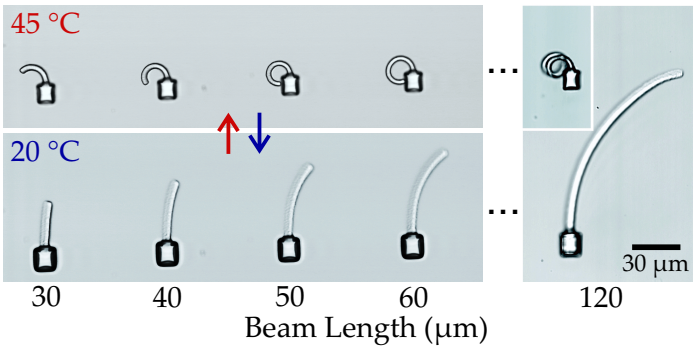

Figure 4.8: Bright-field optical images show the temperature response as a function of beam length for five bi-material structures. Adapted from [33].

Above the LCST, the structures show a large amplitude bending towards the left, less crosslinked side. For $L = 50\,\mu m$ this bending is already sufficiently strong for the beam to touch its central pillar and for $L = 120\,\mu m$ the beam is even convolving several times to form a spiral. Despite these large amplitudes, the process is completely reversible and all structures return to their initial positions upon cooling the sample back down to room temperature. Fabricating free-hanging structures with these lengths and no additional support is only possible due to the hydrogel characteristics of this material. The beams contain a high percentage of water and thus have a similar density to the surrounding media. As a result, the beams swim in the water bath and do not bend downwards due to gravity.

4.4.5 Potential Applications

The structures demonstrated so far can be understood as basic building blocks with large, directed actuations. An especially interesting direction for applications is the field of soft robotics which deals with robotic components from similar materials to those found in living organisms [118]. Typical examples are actuators and grippers with the ability to hold, release and even move objects on demand [119]. Along this line, we designed two demonstrators based on the insights from previous experiments.

Figure 4.9(a) shows optical images of a microgripper based on pNIPAM. Two bi-material beams with opposite crosslinking densities are connected to a mutual base. In this particular design both arms touch each other on the top, thus keeping the gripper in a closed configuration at 20 °C. When the temperature is increased to 45 °C, each arm bends outwards and the gripper

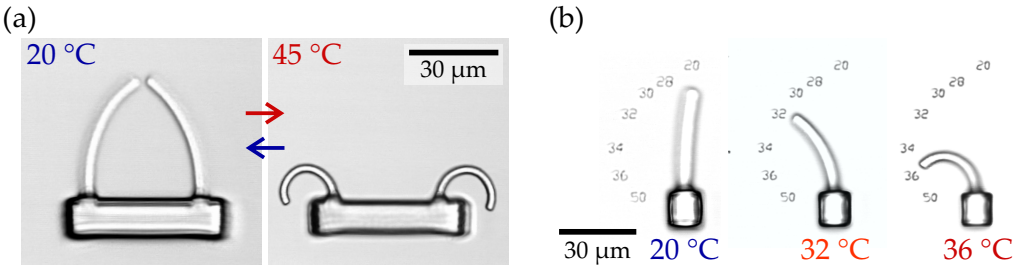

Figure 4.9: (a) Microgripper based on two bi-material beams with opposite crosslinking densities. In this configuration, the gripper is closed at room temperature and open at elevated temperature. (b) Microthermometer with one bi-material beam, which points to the corresponding temperature written as text on the substrate below. Part (a) adapted from [33].

transitions to an open configuration. In this manner, objects are trapped between the two arms and released on demand. Similar to the previously shown experiments, this behavior is completely reversible. In regard to the design flexibility, it is equally possible to switch these two states, such that the gripper is open at room temperature and closed at elevated temperatures.

In the second example, we exploited the excellent reproducibility of the fabrication procedure to design a remote microthermometer, as depicted in Figure 4.9(b). First, we studied the bending behavior of the bi-material beam as a function of temperature, similar to Figure 4.5(b). This time, however, we analyzed in which direction the beam points for a given temperature . In a second step, we fabricated a new sample with a nominally identical bi-material beam and added the temperature information from the previous experiment as text on the substrate. An approach like this is only applicable for a robust fabrication process and negligible sample to sample variations. If these conditions are fulfilled, it is only necessary to experimentally study a given design once and transfer the values to future experiments. The exemplary optical images show the operation of the microthermometer which analogously points towards the current temperature of the surrounding water bath. The comparison with the set values indicated below shows a very good agreement. Based on the thermo-responsive characteristics of pNIPAM, the thermometer is very sensitive in the region between 30 °C and 40 °C, albeit not above and below this interval. This behavior could lead to interesting applications in life sciences, e.g., in cell biology to remotely track the temperature of culture media during live cell imaging.

4.5 Complex Responses and Numerical Predictions

While the presented building blocks with bi-materials beams are sufficient for structures like grippers, advanced applications require even more complex responses. At the same time, more sophisticated designs lead to larger parameter spaces and challenging fabrication procedures. Thus, it is highly desirable to estimate the response of a given design before the fabrication to reduce the number of experimental iteration steps. In this section, I present our results on stimuli-responsive hetero-structures which transform into different shapes and discuss how numerical calculations enable the validation and ultimately guide the design by predicting the expected response.

With the bi-material beams shown so far we did not yet exploit the potential to locally control the exposure dose and thus the degree of responsivity to its fullest extent. In the next step, we fabricated hetero-microstructures with multiple sections as depicted in Figure 4.10. The figure shows optical images of fabricated structures (a) next to designs from numerical calculations which are color-coded for the material properties (b). Similar to the previous figures, green and gray indicate the sides of the beams with the lower and higher crosslinking densities, respectively. The first structure on the left represents a basic bi-material beam as discussed in the previous sections. For the following structures towards the right we split the beam in two, three, and four segments and altered the exposure dose between left and right side of the beam after each segment. As a result, the structures exhibit an increasingly complex response when the temperature is increased to 45 °C. For the second beam with two segments, the lower half bends towards the left-hand side whereas the upper half bends towards the right-hand side to form an s-shape. More segments lead to even more complex shapes, demonstrating how the stimuli-response can be programmed into the structures with high spatial resolution.

In practice, such structures are required to perform tasks, e.g., exerting pressure on a specific spot, and need specific responses to achieve it. This typically involves significant prototyping and testing until a suitable design is found. For this reason, it is important to develop a simple theoretical model with the ability to predict the behavior of these hetero-structures. Although general theoretical descriptions of bi-layered pNIPAM hydrogels are available [120, 121], the material properties resulting from this photoresist system under varying exposure doses have not been studied so far. Therefore, we used a finite element analysis in the commercial software COMSOL

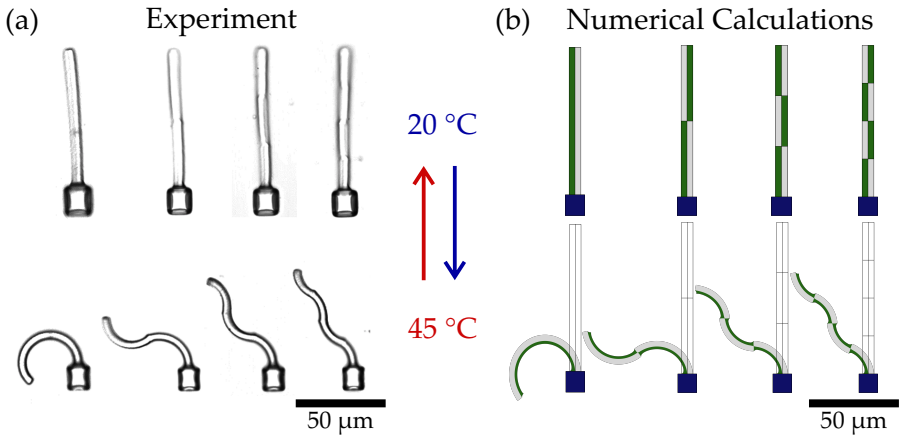

Figure 4.10: Hetero-microstructures with complex thermo-responses. (a) Bright-field optical images of fabricated structures. (b) Corresponding numerical calculations of stimuli-response. For both (a) and (b) the first structures on the left are based on the bi-material design shown previously. In the following structures towards the right-hand side, the exposure dose (and thus the thermo-response) alternates $N = 2, 3, 4$ times, respectively. As a result, the structures undergo an increasingly complex response upon temperature change. Adapted from [33].

Multiphysics and established a reverse engineering approach using linear Cauchy elasticity. Details about the numerical calculations are discussed in section 3.5.1.

In a first step, we fixed the input parameters in such a way that the numerical calculations for the simplest bi-material beam are in accordance to the experimental results (see Figure 4.10(b)). Based on these calculations, both, the thermal expansion coefficient and the Young's modulus, differ by one order of magnitude between the less and the more crosslinked side of the beams. Next, we modeled the three increasingly complex structures with the same equations and material parameters and compared the results with the experimental data. In all three cases, the numerical calculations show an excellent agreement and are able to reproduce the complex behavior of the hetero-structures. Consequently, this model can even be used to predict the response of microstructures for different designs and assess the results based on the desired pattern for the application.

4.6 Two-Photon Induced Local Stimulation

In all experiments so far, we triggered the stimuli-response by global temperature changes. As discussed in the previous sections, the responsivity of structures can be well controlled and several designs with different behaviors can easily be integrated on the same substrate. For applications which require a simultaneous response of all structures on a sample, this global stimulation is particularly suitable. Good examples are stimuli-responsive cell scaffolds as discussed in chapter 5, where hundreds of scaffolds with different properties are triggered at the same time. Other applications, however, require localized stimulations of certain parts on the substrate or ideally even of single structures. Furthermore, temperature changes of the water bath with a high heat capacity lead to timescales in the order of seconds, although often faster switching is desired. Both aspects could be achieved with localized stimulations which are not directly linked to the temperature of the surrounding water bath. This kind of stimulation is, e.g., interesting for microfluidic valves as discussed in section 4.3. Here, a local stimulation would enable a fast opening and closing of individual valves in a complex microfluidic system. In this section, I present our results on the localized stimulation of pNIPAM microstructures via photothermal conversion, induced by two-photon absorption of focused light.

To study the localized response, we fabricated an array of bi-material beam structures with a spacing of 100 µm. Extracts with three of these structures are depicted in the optical images in Figure 4.11(a). In the next step, we illuminated the base of the central structure with the same femtosecond pulsed laser source which is used for the fabrication (see section 3.1.1 for details). After 100 ms, the central structure already shows the same distinct bending to the left-hand side as compared to the results in Figure 4.5(b) with a global temperature increase to 45 °C. The two adjacent structures on either side only show a minor response. When the light is turned off, the beams move back to their initial state within 100 ms. These findings demonstrate the ability for a local and fast stimulation via focused light, opening yet more possibilities for further applications.

This stimulation is based on the photothermal conversion of laser light to heat, an effect with important implications in cancer therapy [122] and drug delivery [123]. The detailed mechanism behind the responses of different structures is revealed by numerical calculations of the temperature distribution in the water bath. Figure 4.11(a) depicts calculated temperature profiles

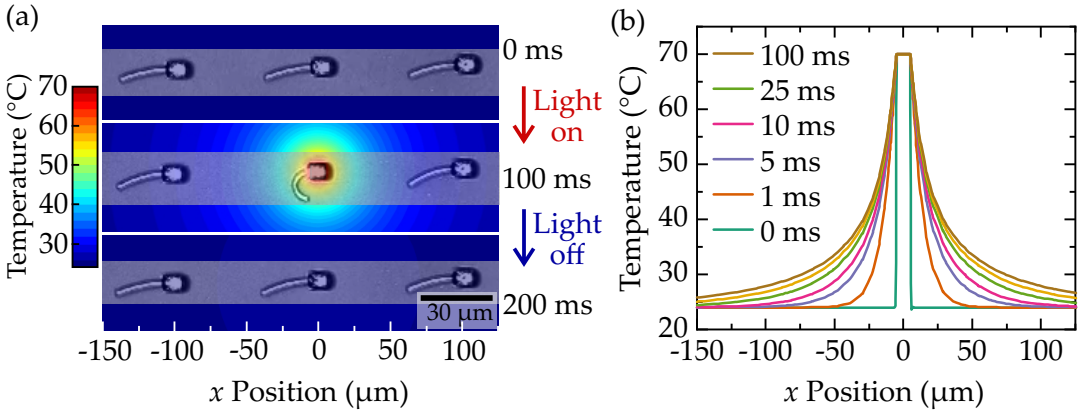

Figure 4.11: Light induced response by photothermal conversion. (a) Bright-field optical images of three bi-material beams with a distance of 100 µm. Focusing a femtosecond pulsed laser on the central base leads to local heat generation by photothermal conversion. The corresponding bi-material beam bends strongly within 100 ms, whereas the adjacent structures in a distance of 100 µm only show a minimal response. After the light is switched off, the beams move back to their original position in a reversible manner. A temperature profile obtained by numerical calculations is overlaid on the optical images, with the corresponding false-color scale on the left side. (b) Corresponding cross-section through the temperature profiles of the central beam after the light is switched on. Adapted from [33].

overlaid on the optical images with the corresponding false-color scale on the left-hand side. The respective cross-section through the temperature profile along the x direction is shown in Figure 4.11(b) with different colors indicating several time points after the heating started. To obtain these results, we modeled the photothermal conversion after switching on the light by assuming a constant temperature for the central base. As a consequence, the temperature of the surrounding water increases over time and heat starts to diffuse away from the center. After 100 ms, the temperature around the central beam increased to over 45 °C, leading to the strong response shown in the optical image. For the adjacent structures with a distance of 100 µm, heat diffusion only leads to an increase from 24 °C to about 27 °C which is still below the regime with the strongest material response around the LCST of 35 °C. For structures yet further away, the response is even smaller.

4.6.1 Photothermal Conversion

To further investigate the photothermal conversion, we conducted an additional experiment with two different photoresists as depicted in Figure 4.12. A pNIPAM bi-material structure is placed next to a small cube made of non-responsive PETA. Illumination of the PETA block leads to a strong bending of the adjacent pNIPAM structure after 100 ms. As soon as the illumination is turned off, the beam returns to its initial position. Primarily, this experiment shows that the pNIPAM response is indeed due to diffused heat in the water bath and not due to additional effects of the focused laser light. The magnitude of the response in regard to the distance of the illuminated spot also fits to the calculated temperature profiles in Figure 4.11. Furthermore, the material characteristics I have discussed in the previous sections, e.g., reversibility, also apply for the local stimulation via light. The second important conclusion from this experiment is that PETA cubes show no measurable response to the illumination. They merely act as absorbers and are not affected themselves by temperature changes. We attribute this absorption to the only common component between the two photoresists, which is a two-photon photoinitiator. To validate this assumption, we performed the same experiment with PETA cubes fabricated without the two-photon initiator, which is possible by excitation of the HOMO-LUMO transition in the resist [124]. Under otherwise similar stimulation conditions, the adjacent pNIPAM structures only display a negligible response, clarifying the role of the photoinitiator in this process.

4.6.2 Numerical Analysis of the Response Time

In the next step, we exploited the numerical calculations to obtain a better insight in the time scale of the stimuli-response. Therefore we studied the cooling process after the light is turned off to see how long it takes for the structure to return to its initial position. Details about the numerical approach can be found in section 3.5.1 The starting point for this calculation corresponds to the end point of the calculation in Figure 4.11(b), after 100 ms of illumination. Figure 4.13(a) depicts the cross-section through the temperature profile for different time points t after the light was turned off at $t = 0$. The temperature rapidly drops in the vicinity of the central structure and already reaches values below 28 °C everywhere after 50 ms. For a closer

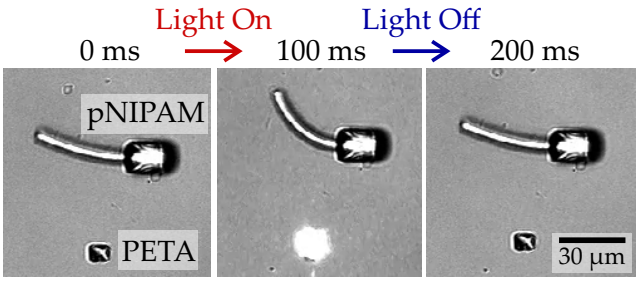

Figure 4.12: Indirect stimulation by heat diffusion from a spatially separated structure. A pNIPAM bi-material beam is fabricated next to a cube of PETA. The locally generated heat from two-photon absorption is distributed through the water bath and leads to a response of the bi-material beam. The PETA cube does not show any measurable structural change or response during this process. Adapted from [33].

look, three specific positions are marked with colored circles in red (center), blue (30 µm distance) and green (100 µm distance) with the corresponding temperatures as a function of time depicted in Figure 4.13(b). The region of strongest material response between 30 °C and 40 °C is highlighted in gray. As discussed in section 4.6, the temperature around structures in a distance of 100 µm stays below 30 °C and thus only a negligible response is observable. For the bi-material beam 30 µm away from the center, the temperature drops below 30 °C within 25 ms and quickly approaches room temperature which was fixed to 24 °C in these calculations. Even though it takes more than 100 ms until the structures completely return to their initial position, the vast majority of the response occurs within 25 ms.

Importantly, this time scale is only valid for the cooling process after the light is turned off. The photothermal heating calculations depicted in Figure 4.11(b) also indicate a time scale of about 30 ms until the temperature around the central bi-material beam is above the strongest response regime. In these calculations, however, we simplified the starting conditions and fixed the base to a constant temperature at $t = 0$, in contrast to the real experimental situation where the base starts to heat up only when the light is turned on. As a consequence the calculated value is an underestimation of the real time scale for the heating process. Nevertheless, the numerical calculations are in good accordance with the experimental results that the dominant response of the structures can be controlled within 100 ms in both directions.

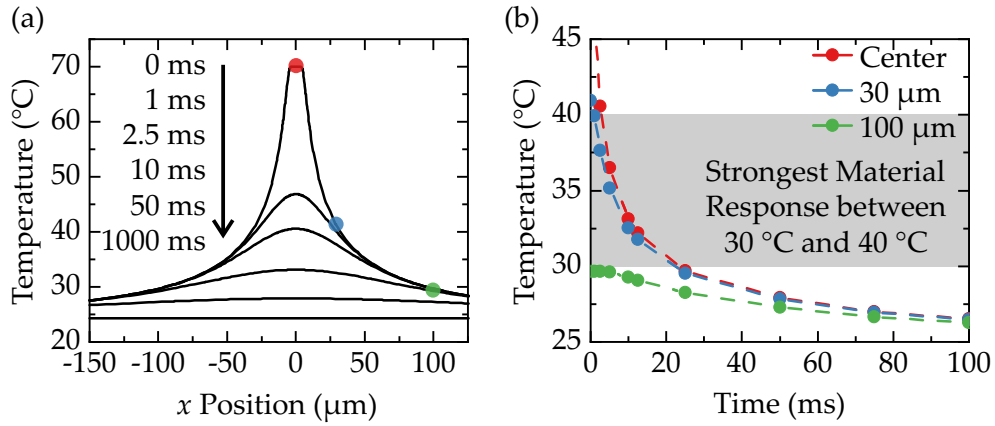

Figure 4.13: Numerical analysis of the response time. (a) Cross-section through the temperature profile of the base inside a water bath. The time $t = 0$ corresponds to $t = 100\,\text{ms}$ in Figure 4.11. Here, the constant temperature restriction of the central base is lifted to observe the cooling behavior over time after the light has been turned off. (b) Corresponding temperature as a function of time at three positions, labeled in the respective colors. The gray area highlights the regime with the strongest material response (see Figure 4.5). Adapted from [33].

In summary, illumination of the bi-material structures with focused laser light leads to strong responses due to photothermal conversion and subsequent heating of the surrounding media. Only beams close to the illuminated spot show strong responses, enabling the defined localized stimulation within an array of fabricated structures. Furthermore, the response time is in the order of 100 ms and thus significantly faster compared to a global heating of the water bath.

4.7 Discussion

In this chapter, I presented our results on pNIPAM microstructures fabricated by 3D laser lithography. By application of a gray-tone approach we were able to locally control the material parameters and thus the stimuli-response in a single fabrication step. The resulting structures showed a directed, large-amplitude response to changes in temperature. Numerical calculations facilitated a deeper understanding of the response patterns and opened the possibility to predict the structural behavior of new designs. Furthermore, I discussed the stimulation of individual structures with focused light as a

tool to locally control the response on a fast timescale. The results in this chapter provide a toolkit with basic building blocks to fabricate and control pNIPAM microstructures. Many of the presented concepts, however, are also applicable to other stimuli-responsive material systems. Subsequent works should pursue two aspects: the further development of this toolkit and the implementation of theses methods on specific applications.

One interesting addition to the system would be a controlled shift of the LCST by modifications of the photoresist composition. Since the LCST is already close to the body temperature of 37 °C, this is particularly interesting for biomedical applications and the idea has already been widely applied for pNIPAM microparticles in the context of drug release [84, 85]. For microstructures, this would open the possibility to trigger responses at a defined level, e.g., when the temperature drops below a certain threshold. Next, it would also be possible to combine structures with different LCSTs on the same sample and thus achieve a cascade of different reactions when certain thresholds are exceeded. Yet another step in this direction could be the integration of polymers with a sharp upper critical solution temperature (UCST) [125]. Polymer networks with an UCST basically display the inverse behavior upon heating, i.e., they take up water and expand when the temperature is increased above this point [126]. The combination of LCST and UCST materials on one sample could enable even more advanced applications like sophisticated pumps to move fluids by alternating expansion and contraction cycles [127].

Regarding the activation via light, it would be important to further study the process and optimize the conditions. So far, we exploited residual photoinitiator molecules as absorbers which is rather inefficient and can lead to irreversible effects for long irradiation times. Here, an interesting route could be the incorporation of gold nanoparticles in the polymer network to exploit the surface plasmon resonance, although the interaction of particles with the laser during fabrication poses additional challenges [128, 129]. Such nanoparticles are very efficient in the conversion of near infrared light to heat and have already been successfully applied in pNIPAM microparticles [130] and pNIPAM gels [131]. On the other hand, the utilization of residual two-photon photoinitiators has the interesting advantage that the absorption is based on a nonlinear process. Accordingly, the intensity profile of the excitation is effectively squared and the accumulation of exposure dose outside the laser focus is strongly suppressed. This aspect is especially important in the axial direction and allows the concentration of the excitation in all three spatial directions (see section 2.1.2). An interesting application

could be the combination of stimuli-responsive valves and the local activation via two-photon absorption to enable the remote control of fluid flows in complex 3D microfluidic systems.

Another generally promising research area is the field of cell biology. Here, the ability to first tailor the cellular microenvironment and then change it on demand has huge potential to study cellular responses [132]. However, more work has to be done to decrease fabrication times of the structures. Biological experiments typically require a large amount of samples with many structures to obtain the necessary statistical confidence and the writing speed in the pNIPAM resist is currently slow compared to conventional photoresists. Thus, further optimization of the resist composition, focused on the specific requirements of applications, could lead to a substantial acceleration of the sample preparation. On the other hand, it is important to note that only the stimuli-responsive parts have to be fabricated with the pNIPAM resist. If the structures are mainly based on non-responsive, mechanically stable materials, conventional resists with high fabrication speeds can be easily integrated in a sequential fabrication procedure as demonstrated in section 4.3. Ultimately, there are many possibilities to use and combine the different approaches I presented in this chapter and they will hopefully help to tackle unsolved challenges in various research areas in the future.

Chapter 5

5 Cell Mechanics in Responsive Microscaffolds

In the recent past, cell biological research has expanded its view from a mostly biochemical perspective towards biophysical cues which influence cellular behavior [45]. A stiffer environment, for example, leads to more polarized and contractile cells compared to softer environments [133]. Depending on the mechanical properties of substrates, cellular migration changes and the differentiation of stem cells into different cell types is strongly affected [134]. Furthermore, cells exploit mechanosensitive modules such as cell adhesion sites, ion channels, and the cytoskeleton to recognize and transduce mechanical stress and strain patterns [135]. All of these mechanical inputs are eventually converted to biochemical signals, which influence a multitude of cellular processes ranging from dynamic rearrangements of actin stress fibers and the actin cortex to the response to soluble ligands and gene expression [136]. In this context, it is particularly interesting to study the response of cells to changes in their physical environment. Here, a promising method is the application of mechanical stretches to cells and subsequent observation of their behavior. However, although several approaches in this direction have been established, it remains challenging to monitor the cellular response to mechanical changes in their microenvironment.

The most common techniques to mechanically stimulate cells rely on piezoeletric [137], pneumatic [138], or electromagnetic [139] deformations of PDMS substrates or thin membranes [140, 141]. Here, cells are confined to a two-dimensional (2D) geometry and adhere in random morphologies which limits the ability to apply locally defined stimulations. On the other hand, approaches such as optical tweezers [142], microplates [143, 144], atomic force

microscopes [145], or micromanipulators [146] offer precise displacements in the local 3D environment of cells. These techniques, however, are hardly scalable to study a large number of cells and a fixation in the stretched state to study subcellular compartments is not possible. Moreover, these methods typically require complex experimental setups to control the stimulation. Several reviews in literature deal with the advantages and disadvantages and give detailed descriptions of the various techniques [147–149]. None of the available methods, however, provides both, the ability to apply locally defined stretches in 3D microenvironments and the necessary scalability to enable the analysis and quantification of biological effects.

In the last decade, 3D laser lithography has emerged as a tool to fabricate cell scaffolds with a tailored geometry and spatially functionalized surfaces [150–154]. This technique offers great flexibility to design the 3D cellular environment. The transition from passive to active scaffolds, however, requires new materials which can change their properties on demand [132]. A number of studies in the past have already applied hydrogels which respond to changes in temperature [155] or pH [156], enzymes [157], or illumination with UV light [158] to dynamically control cellular behavior. For applications in cell biology, it is crucial to apply stimuli under physiological conditions to minimize the impact of the stimulus itself on cells and thus prevent unwanted side effects [159]. In this context, supramolecular polymers based on interactions between host- and guest-molecules [160–162] provide an advantage over the above mentioned materials because appropriate host or guest molecules can be selected depending on the application [163].

In this chapter, I present our results on 3D microscaffolds based on host-guest interactions to mechanically stimulate single cells. I first discuss the photoresist composition and basic characterization of the material. Next, I introduce the composite scaffold design as well as the numerical calculations we used to connect experimental displacements to cellular forces. In the following sections, I show our results on the initial contraction force of cells in the scaffolds and how they react to mechanical stimulations. Furthermore, I highlight how these effects depend on the cellular actomyosin machinery which is strongly reorganized after stretching. In the last two sections, I demonstrate the inherent flexibility of this approach to adapt the scaffold design and introduce initial experiments on fluorescent live cell imaging.

Unless specifically stated, all experiments presented in this chapter have been carried out by me. For the cell-experiments presented in the later parts of this chapter, various cell lines had to be kept in routine culture. This work was performed by Dr. Kai Weißenbruch and Kai Richler, both

members of the group of Prof. Martin Bastmeyer at the Karlsruhe Institute of Technology. During the preparations of the experiments, they applied the protein coating on the prepared samples and seeded cells on the scaffolds. After the experiments, they performed the fixation and immunocytochemical staining procedures to be able to record fluorescent images.

5.1 Microstructures Based on Host-Guest Complexes

In this initial section, I introduce the material mechanism based on host-guest complexes which are the basis for the stimuli-responsive structures fabricated in the scope of this work. I start with a discussion about the photoresist composition and the role of the individual components. In the next step, I show basic characterizations of fabricated microstructures and explain the principle behind the host-guest mechanism.

5.1.1 Photoresist Composition

The first step towards stimuli-responsive microstructures is the development of a suitable photoresist which is compatible with 3D laser lithography. The recipe is based on host-guest complexes which are incorporated as non-covalent crosslinks in polymer networks. A detailed description of all components and the step-by-step procedure to use this resist for 3D laser lithography can be found in section 3.1.3.

Figure 5.1 shows the chemical structure of the photoresist components and the resulting polymer chains after photo-polymerization. The formula is based on a mixture by Harada *et al*. who used a thermal polymerization procedure to fabricate bulk hydrogels based on host-guest complexes [76]. To obtain a photoresist which can be employed for 3D laser lithography, however, it was necessary to significantly alter the composition and preparation protocols. The main elements are β-cyclodextrin acrylamide (βCD-AAm) and adamantane acrylamide (Ad-AAm). Both molecules are linked to acrylamide (AAm) to enable their incorporation in polymer networks and have been synthesized and provided by the Harada group according to previously published protocols [76]. Adamantane (guest) is strongly hydrophobic and fits well into the hydrophilic cavity of β-cyclodextrin (host). As a result, they have a strong affinity to establish a non-covalent interaction in aqueous environments with an association constant of $K_a > 10^4\,1/\mathrm{M}$ [164]. Since both molecules are included in a polymer backbone formed by acrylamide

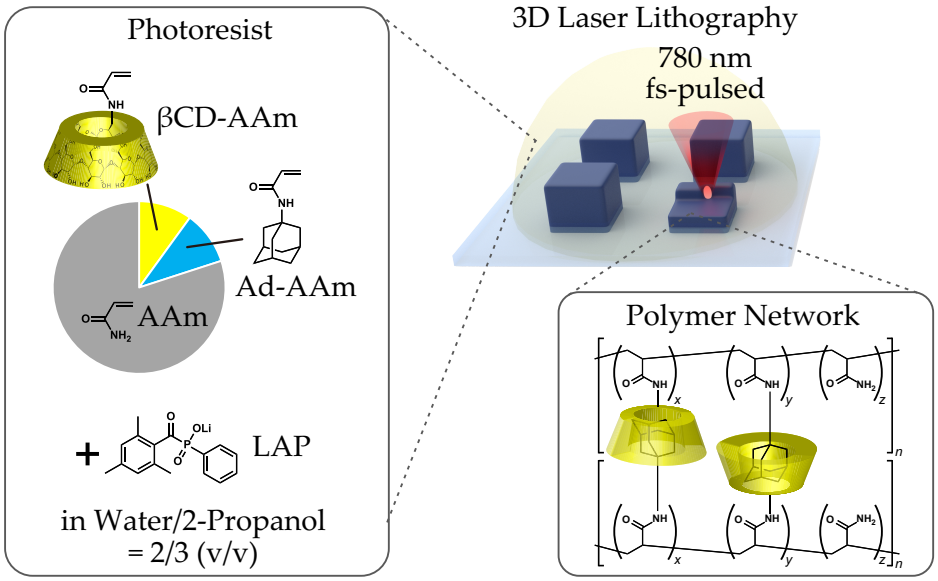

Figure 5.1: Host-guest photoresist for 3D laser lithography. Chemical structure of the main components βCD-AAm (host) and Ad-AAm (guest) together with AAm as the polymer backbone. The resulting network after polymerization consists of polymer chains of these three components which are connected with each other via host-guest complexes. Adapted from [34].

(AAm) molecules, these complexes connect single polymer chains with each other. Thus, they effectively act as crosslinks to form hydrogel networks. The molar ratio in the photoresist is chosen as 1 : 1 so that each host incorporates one guest, although in a real experimental situation not all molecules have suitable counterparts in their vicinity. Another important component is the two-photon initiator LAP, which was already discussed in section 2.2. Here, its most important characteristics are the high two-photon absorption efficiency and low cytotoxicity [30]. All components are solved in a mixture of water and 2-propanol.

This photoresist enables the fabrication of microstructures via 3D laser lithography at a wavelength of 780 nm. In contrast to the previous chapter about pNIPAM microstructures, the stimuli-responsive components are now the crosslinks and not the monomers in the backbone of the polymer chain. The general implications of this aspect are discussed in section 2.2.1 in detail, although the most important difference is that the mechanical stability and the functionality are mostly independent for the host-guest photoresist.

5.1.2 *Material Characterization*

Next, we fabricated an array of blocks via 3D laser lithography to study the stimuli-responsive material properties. These blocks were fixed to the substrate by a prior silanization treatment of the glass surface (see section 3.1.2 for details) and developed in water after the fabrication. For all characterization experiments we transferred the samples to PBS because it is closer to the experimental conditions in cell experiments and additional salts in solution can influence the equilibrium of the host-guest complexes [165]. Figure 5.2 shows two bright-field optical images of blocks with a footprint of $25 \times 25\,\mu m^2$ with and without stimulation. Close to the optical images are schemes of host-guest complexes in the hydrogel network in different phases of the experiment.

The left image depicts the fabricated blocks in pure PBS solution. In this state, β-cyclodextrin and adamantane form host-guest complexes which link the polymer chains together. As a result, the network is stabilized by a large number of crosslinks and the hydrogel is in a stiff and compact state. This equilibrium can be disturbed by addition of the adamantane derivative 1-adamantanecarboxylic acid (1-AdCA) in solution. For all experiments in this chapter, we used 1-AdCA as additional guests because pure adamantane is poorly soluble in water and both have a similarly high affinity to form a complex with β-cyclodextrin. These additional guests are also hydrophobic and act as competitors to bound adamantane molecules for the limited number of available hosts. Since the host-guest complexation is a dynamic equilibrium, an exchange between bound and solved guest molecules takes place. After a transition period, a new steady state is formed where a portion of β-cyclodextrin cavities are occupied by solved 1-AdCA molecules. However, these complexes do not contribute as links between the polymer chains and the overall number of crosslinks in the network is reduced. Thus, the hydrogel becomes mechanically softer and takes up more water. This effect is clearly shown in the right optical image after addition of 20 mM 1-AdCA in PBS. The blocks swell significantly and the image contrast is lower because more water is taken up by the hydrogel, which reduces the refractive index contrast with the surrounding media.

One very important aspect of this system is the reversibility of this process. By rinsing the sample with pure PBS, solved 1-AdCA molecules are removed and only β-cyclodextrin and adamantane linked to the polymer

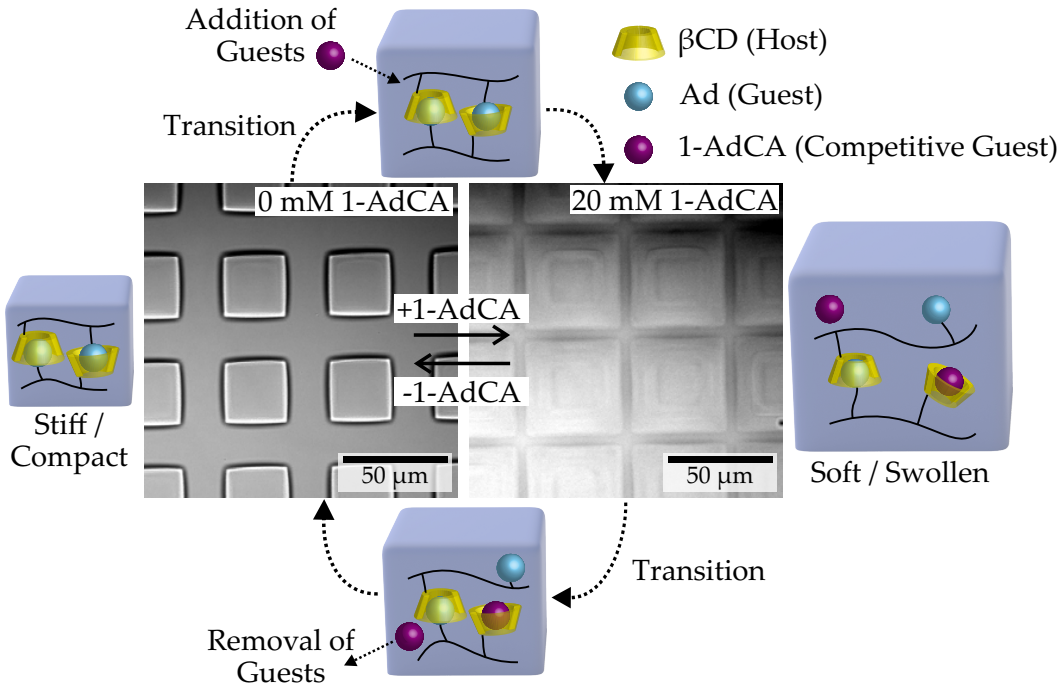

Figure 5.2: Stimuli-response of fabricated microstructures. The center region shows bright-field optical images of blocks fabricated by 3D laser lithography from the host-guest photoresist. Schemes next to the images depict different states of the hydrogel network during stimulation. Addition of 1-AdCA in PBS leads to a competition effect between bound and solved guests and subsequent reduction of crosslinks. As a result, the hydrogel blocks show a significant isotropic swelling. This process is completely reversible and the hydrogel shrinks back to the initial state when the 1-AdCA guest molecules are removed. Adapted from [34].

chains remain. In another transition period, the equilibrium shifts back, crosslinks form again, and water is expelled from the polymer network. As a consequence, the initial stiff and compact state of the hydrogel is restored.

A closer analysis of the swelling behavior is depicted in Figure 5.3 for the block area as a function of time. At 100 s, the solution was exchanged to 20 mM 1-AdCA in PBS, as indicated by the blue region. Immediately, the measured block area substantially increases and stabilizes on a level which is more than two times higher than initially. This new equilibrium is formed about 100 s after the injection. The process, however, is strongly driven by diffusion and solved competitors have to first penetrate the network

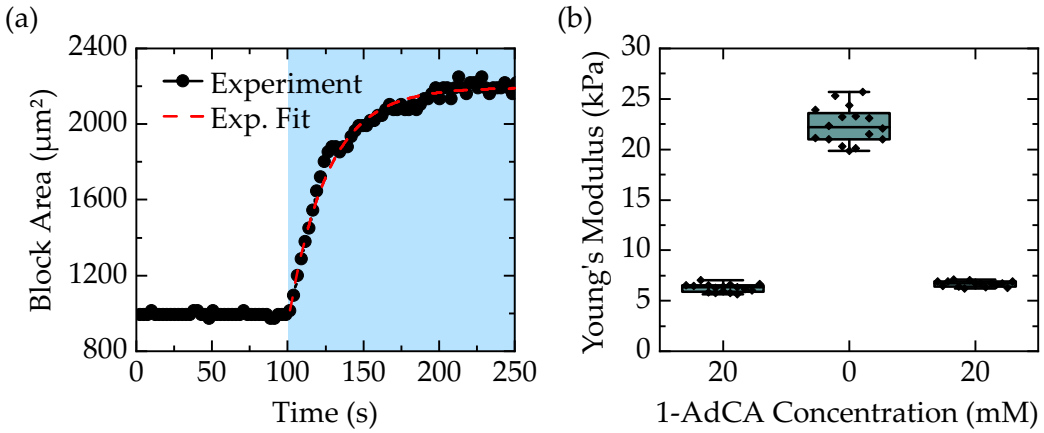

Figure 5.3: Material properties of hydrogel blocks. (a) Measured block area as a function of time. After addition of 1-AdCA in PBS (blue region), the block area strongly increases by more than a factor of two in about 100 s. (b) Young's modulus measured by AFM nanoindentation. In a 20 mM 1-AdCA PBS solution, the hydrogel is swollen and soft. After solution exchange to pure PBS, host-guest crosslinks re-form and the polymer network stiffens considerably. Another addition of 20 mM 1-AdCA in PBS leads to the reversible transition to the soft state. Adapted from [34].

before an exchange with the bound guest molecules can take place. As a consequence, timescales strongly depend on the size and geometry of the given structure (see section 5.2.3).

We also analyzed the mechanical properties of the material by AFM nanoindentation (see section 3.2 for more details). Figure 5.3(b) shows the Young's modulus for a transition through the soft and stiff state. The initial stiffness of 7 kPa in a 20 mM 1-AdCA solution (open crosslinks) increases to 23 kPa after substitution with pure PBS (closed crosslinks). A second exchange back to the 20 mM solution restores the initial value, highlighting the reversibility of the system. This ability to change the Young's modulus has interesting implications for experiments with cells which are very sensitive to stiffness changes in this regime [166]. For this reason, macroscopic host-guest hydrogels based on β-cyclodextrin and adamantane have already been applied to dynamically regulate cell morphology and cytoskeletal ordering of myoblasts [163].

5.2 Composite Scaffolds for Cell Manipulation

So far, I have introduced the basic mechanisms of the host-guest system and the material properties of fabricated hydrogel structures with the developed photoresist. Based on these results, we designed a platform to mechanically stimulate individual cells in defined 3D microenvironments. In this section, I first present our design for multi-material scaffolds based on the combination of the developed supramolecular host-guest material with two conventional photoresists. The second section is dedicated to the analysis of beam displacements which is crucial for all following experiments in this chapter. In the third part, I discuss the characterization of different aspects like the reversibility, the concentration dependence, and the timescale of the process in detail.

5.2.1 Design of Multi-Material Scaffolds

In order to manipulate individual cells in 3D microenvironments, it is necessary to first, guide them to specific positions and second, to apply a defined external stimulation. Therefore, we combined two materials with different surface properties with the stimuli-responsive host-guest hydrogel in a sequential fabrication process as described in section 3.1.5 in detail.

The basic design of the scaffold is schematically depicted in Figure 5.4. The four gray walls connected to the glass substrate are fabricated with a photoresist based on the monomer trimethylolpropane ethoxylate triacrylate (TPETA) which is repellent for proteins. The orange beams, on the other hand, consist of pentaerythritol triacrylate (PETA), a material which allows protein adsorption. The recipe for both photoresists can be found in section 3.1.3. Due to these different surface properties, coating of the scaffolds with the extracellular protein fibronectin only covers the surface of the PETA beams on top. This aspect is crucial to guide the adhesion of cells to the desired positions. The scaffold is complemented by the yellow host-guest hydrogel in the center, which is enclosed by the TPETA walls. As indicated in the schematic, the hydrogel expands when the competitive 1-AdCA guests are added and pushes on the gray TPETA walls. Since they are fixed to the glass substrate, they bend outwards and pull the PETA beams away from the center. Thus, a cell attached to the four beams on top is significantly stretched on all sides.

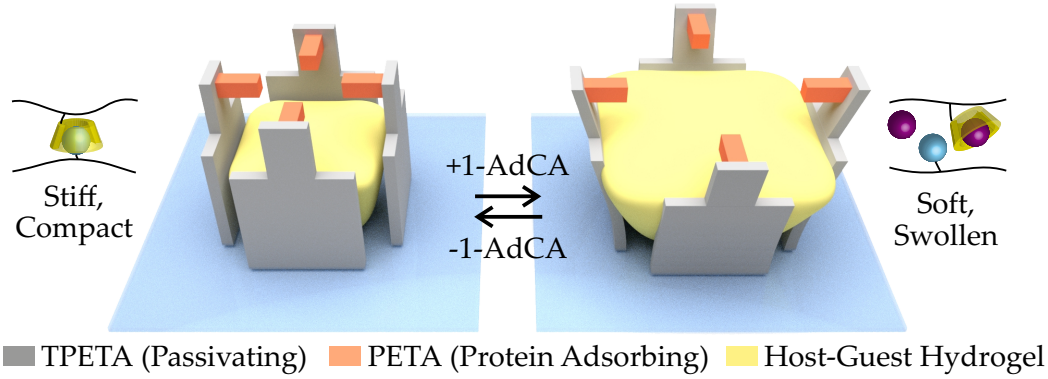

Figure 5.4: Schematic design of stimuli-responsive scaffolds fabricated by 3D laser lithography. Three different materials are used in a sequential fabrication procedure. Addition of 1-AdCA expands the host-guest hydrogel in the center (yellow), leading to an outward bending of the protein repellent TPETA walls (gray). As a result, the protein adsorbing beams of PETA (orange) on top are displaced from the center. Adapted from [34].

This indirect force transmission has several advantages compared to a approach where cells are directly cultivated on responsive materials [163]. First, swelling of the host-guest hydrogel is accompanied by a significant decrease of the Young's modulus as discussed in section 5.1.2. In a direct contact of cell and hydrogel, both effects are superimposed and lead to individual cellular responses which are indistinguishable. To study the mechanisms behind cellular behavior, however, it is mandatory to isolate cause and reaction as much as possible from all further external effects. The second advantage of our indirect approach is the ability to exploit different surface properties to guide cells to specific positions and force them in the desired shape.

In this design, the stimuli-responsive hydrogel has no direct contact to the cell on top. To verify this, we fabricated slightly modified scaffolds with fluorescent materials as depicted in Figure 5.5. The two images show 3D reconstructions of fluorescent image stacks obtained via laser scanning microscopy. The host-guest hydrogel is colored in yellow since we added a rhodamin-acrylate which is covalently included in the polymer network. On top of the non-fluorescent TPETA walls, we fabricated markers containing the fluorescent photoinitiator DETC, here colored in orange. The image stack was recorded in the swollen state of the hydrogel after addition of 1-AdCA. Even though the hydrogel expansion leads to a significant bending of the

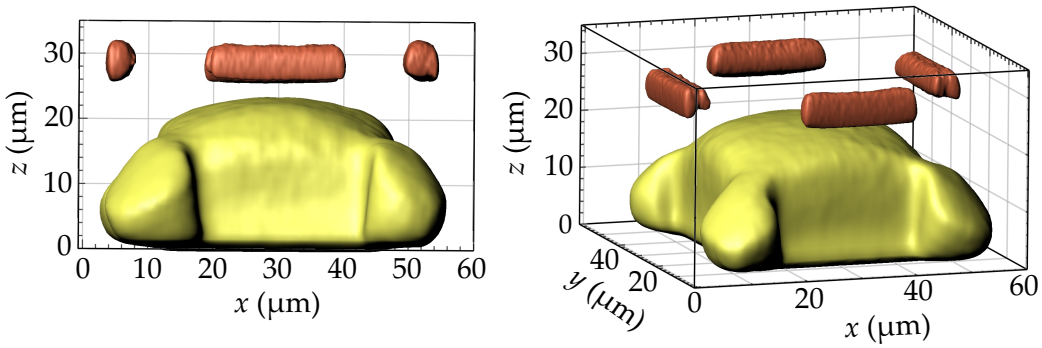

Figure 5.5: Hydrogel expansion inside the scaffolds. Two 3D reconstructions from fluorescent image stacks. The expanded hydrogel (colored in yellow) is not in contact with the PETA markers (colored in orange) on top of the non-fluorescent (and thus not visible) TPETA walls.

TPETA walls, the upper surface is still below the markers indicating the top of the wall. Thus, a cell sitting at the marker position is not in contact with the hydrogel below, even in the swollen state.

5.2.2 *Experimental Analysis of Beam Displacements*

In the next step, we fabricated scaffolds based on this design and characterized the displacements of the beam as a response to the external stimulation. Therefore, we used digital image cross-correlation, which is described in section 3.4 in more detail. This technique enabled us to precisely track displacements of the PETA beams with sub-pixel resolution from a series of optical bright field image [78]. Figure 5.6(a) shows two optical images from a time series during a stimulation experiment before and after addition of 20 mM 1-AdCA. The red arrows in the right image indicate displacements of individual beams after stimulation, scaled by a factor of three for visibility. The corresponding track in Figure 5.6(b) of the figure depicts the average beam displacement for this scaffold as a function of time over the whole course of the experiment. A displacement away from the center of the scaffold is defined as a positive value whereas a displacement towards the center is defined as a negative value. Averaging the resulting displacements of all four beams effectively subtracts the center of mass of the scaffold and thus eliminates external perturbations caused by sample drifts or stage movements.

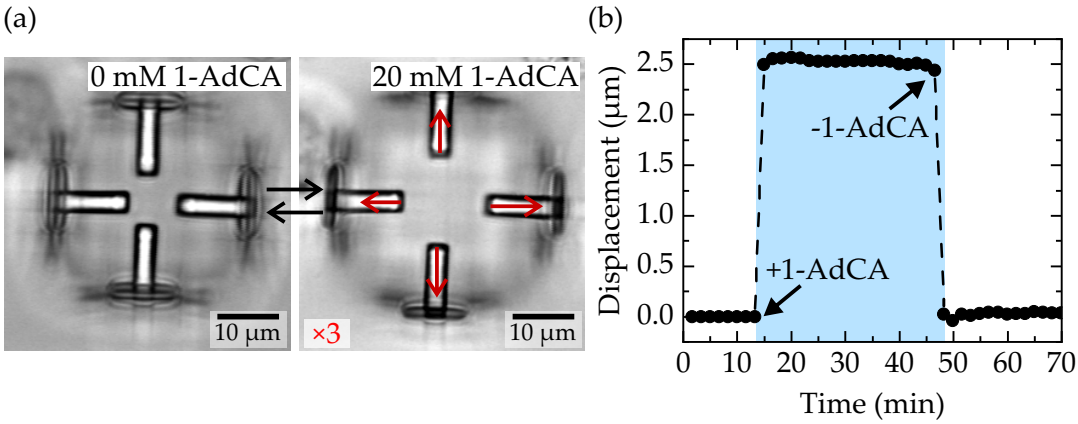

Figure 5.6: Tracking of beam displacements. (a) Bright-field optical images of a scaffold in 0 mM and 20 mM 1-AdCA solution. Red arrows indicate individual beam displacements in the expanded compared to the initial state (scaled by a factor of 3), obtained via digital image cross-correlation. (b) Corresponding average beam displacement relative to the center as a function of time after addition of 1-AdCA at minute 12 and exchange to pure PBS at minute 48. The structure shows a stable response after stimulation and a completely reversible behavior. Adapted from [34].

The depicted track shows the scaffold response to a similar stretch-release cycle which was applied to stimulate cells during the experiments presented in the subsequent sections of this chapter. After 12 min, 1-AdCA is added to expand the host-guest hydrogel. As a result, the four beams move 2.5 µm away from the center and remain on this new level. Only when the competitive guest molecules are removed again by rinsing with pure PBS solution at 48 min, the hydrogel shrinks and the beams move back into their initial position. In this way, it is possible to exert large and reversible equibiaxial stretches to cells adhered to the beams on top of the scaffolds. Furthermore, the high spatial resolution of the digital image cross-correlation enables the precise analysis of cellular mechanical responses to the applied stimulation. To be able to exchange solutions without interfering with the experiment, we designed a compact microfluidic chamber which can be easily integrated in typical inverted microscopes (see section 3.3 for details).

The stimulation triggered by solution exchange leads to a simultaneous response of all structures on a sample which makes the approach inherently scalable. This is a crucial prerequisite for biological applications to obtain the necessary experimental throughput and sufficient statistical confidence in the observed effects. Figure 5.7 shows three scanning electron micrographs

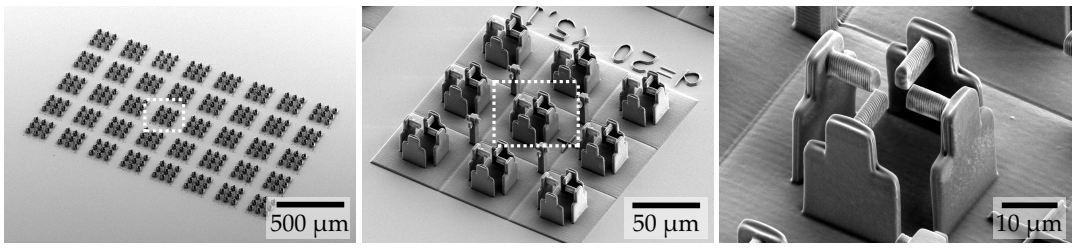

Figure 5.7: Scanning electron micrographs of a typical fabricated sample with increasing magnification from left to right. 5×8 arrays with 9 structures each (without the host-guest hydrogel) are arranged on the substrate. The total number of 360 scaffolds enables a simultaneous analysis of a large number of cells. The scanning electron migrographs were taken by Vincent Hahn (KIT). Adapted from [34].

of a typical sample with increasing magnifications from left to right. The hydrogel is not included in this sample because it has to be dried for SEM preparation which would result in the destruction of the scaffold. The structures are grouped in arrays of 3×3 scaffolds which corresponds to the writing field of about $150 \times 150\,\mu m^2$ for the fabrication via 3D laser lithography. 8×5 of these fields lead to a total number of 360 scaffolds per sample.

The scaffolds are designed to fulfill several criteria regarding the experimental workflow. The size of approximately $25 \times 25\,\mu m^2$ provides sufficient space for the cell types used in this work to spread on the beams coated with fibronectin. Pointing the beams towards the center of the scaffold increases chances for cells to make contact during the seeding procedure and the gaps between adjacent beams are sufficiently small to span across. The central image reveals additional squares of TPETA on the substrate. This layer is necessary to make the surface below each scaffold protein-repellent and thus suppress cell attachment in this area. In this way, unwanted side effects of multiple cells on the scaffold can be prevented.

One of the most critical parameters is the thickness of the walls as it determines the ability of the expanding hydrogel to deflect them. Although a large response is generally desirable, making them too thin leads to mechanical instability. This is especially critical since the TPETA walls are fabricated in the first step of a sequential fabrication process with multiple development steps. Capillary forces during the drying can lead to significant deformations and polymer structures typically stick together once they get in

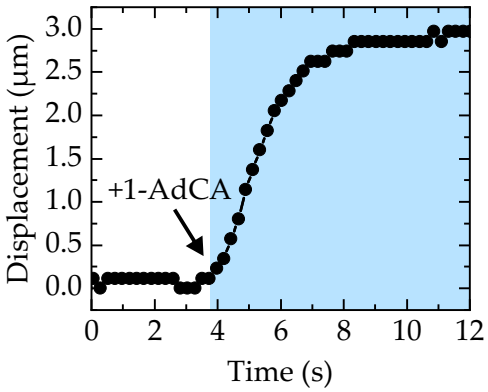

Figure 5.8: Timescale of the material transition. The data shows the average beam displacement as a function of time after addition of 1-AdCA. The response of the hydrogel takes about five seconds to reach the new, swollen equilibrium state. Adapted from [34].

contact with each other, rendering the scaffolds unusable. As a consequence, the design is carefully optimized to enable the largest possible response while still maintaining a robust and reproducible fabrication process.

5.2.3 *Characterization of Stimuli-Response*

Next, we performed a more detailed analysis of different aspects of the scaffold response. In a first step, we looked at the timescale of the transition after stimulation. As discussed in section 5.1.2, the establishment of a new equilibrium level by exchanging bound and free guest molecules is a diffusion driven process and thus strongly depends on size and geometry of the structures. To study this effect, we measured the average beam displacements of a scaffold after the addition of 1-AdCA with a high temporal resolution, as depicted in Figure 5.8. The resulting track shows that the new steady state is already reached after several seconds compared to the timescale in the order of 100 s for larger hydrogel blocks in previous experiments.

We also analyzed the dependency of the scaffold response to the 1-AdCA concentration in solution. As discussed in section 5.1.2, the host-guest complexation is a dynamic equilibrium and presence of competitive 1-AdCA leads to an exchange with adamantane molecules bound to the polymer chain. The magnitude of this exchange and thus the new equilibrium level, however, depends on the number of available 1-AdCA molecules in

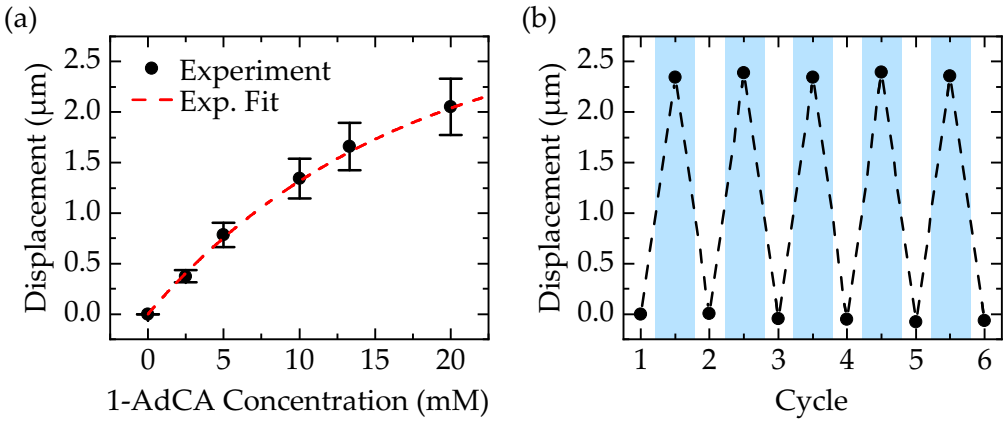

Figure 5.9: Characterization of the scaffold response. (a) Average beam displacement as a function of 1-AdCA concentration. The response can be precisely controlled by the concentration of 1-AdCA molecules in solution. The error bars indicate standard deviations for measurements on multiple scaffolds. (b) Average beam displacement for multiple cycles of solution exchange from 0 mM of 1-AdCA (white regions) to 20 mM of 1-AdCA (blue regions). The response of the structures is completely reversible within measurement errors. Adapted from [34].

solution. This trend is depicted in Figure 5.9(a) which shows the average beam displacement as a function of the 1-AdCA concentration. The data points follow a limited growth function as indicated by the red dashed line with the highest experimentally measured displacement of 2.5 µm for a concentration of 20 mM. Yet larger displacements are limited by the solubility of 1-AdCA in cell culture medium. These results highlight the ability to precisely control beam displacements and thus the cellular stretch by the corresponding 1-AdCA concentration.

Another important aspect is the reversibility of the system for multiple cycles of stimulation, as depicted in Figure 5.9(b). The white and blue regions indicate 1-AdCA concentrations of 0 mM and 20 mM, respectively. The measured beam displacements show no variation of the two levels within measurement errors and thus no deterioration of the stimuli-response of the scaffolds over time.

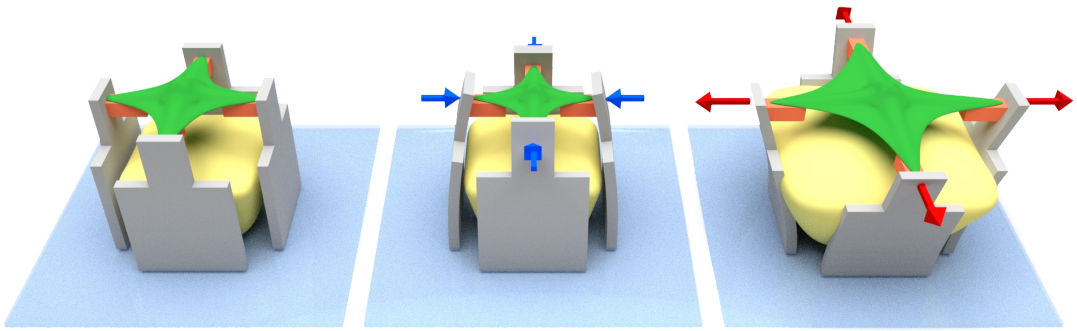

(1) Invasion of Scaffold (2) Initial Contraction Force (3) External Stretch

Figure 5.10: Schematic of the cellular interaction with the scaffolds. After seeding, cells invade the scaffolds and form adhesions on the beams coated with fibronectin. In this process, they build up initial contraction forces which pull the beams inward (blue arrows). The stimulated expansion of the hydrogel stretches cells by displacing the PETA beams (red arrows). Adapted from [34].

5.3 Correlating Displacements to Cellular Forces

In the last section, I have introduced the scaffold design along with characterizations of the stimuli-responsive behavior. As a last step before the application in biological studies, it is necessary to connect the experimentally observable beam displacements to corresponding forces. Thus, I discuss in the next section how we used numerical calculations to model the scaffolds and made the transition to cellular forces.

Initially, it is necessary to discuss how cells interact with the scaffolds. The first phases of the cellular behavior are schematically depicted in Figure 5.10. After seeding cells on the sample, they invade the scaffolds and spread on the four PETA beams coated with fibronectin (1). In this process, they form adhesions on the surface proteins and build up contraction forces which pull the beams towards the center of the scaffold. As a result, the walls bend inward as indicated by the blue arrows (2). After a transition period, a new steady state is reached in which the cells established an initial contraction force. At this point, the expansion of the host-guest hydrogel can be triggered by addition of 1-AdCA and cells are stretched on all sides as indicated by the red arrows (3).

To extract cellular forces from experimental beam displacements we performed finite element method (FEM) calculations in the commercial software COMSOL Multiphysics. The necessary material parameters were obtained

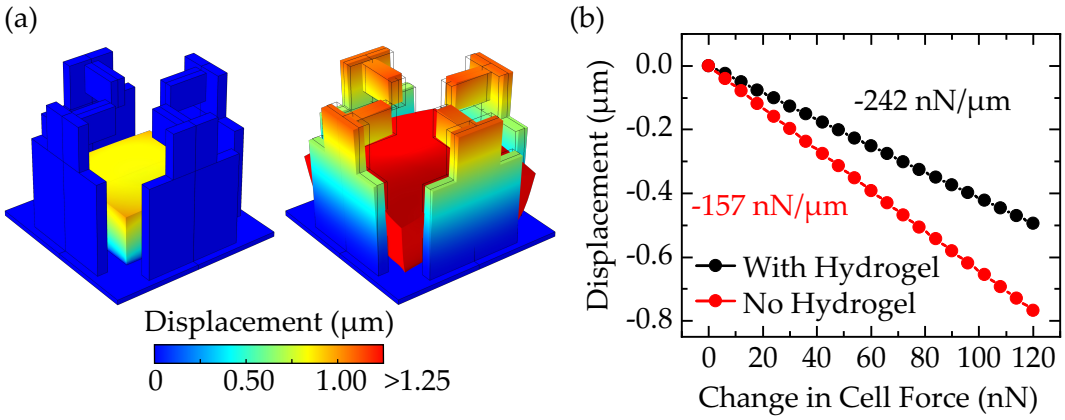

Figure 5.11: Numerical calculations on beam displacements. (a) Exemplary images of two time points before and after expansion of the hydrogel. The color scale below indicates the strength of the displacement of different segments. (b) Displacement as a function of force for scaffolds with and without the hydrogel in black and red, respectively. Negative values are defined to point towards the center of the scaffold. The numbers next to the data indicate the slope of the linear fit. Adapted from [34].

by AFM nanoindenation experiments and the geometrical dimensions were extracted from scanning electron micrographs. A detailed description of the simulation procedure can be found in section 3.5.2. Figure 5.11(a) shows two exemplary images of the calculation before (left) and during (right) expansion of the central hydrogel. The color scale below indicates the strength of displacements for different parts of the scaffold.

In the next step, we calculated the forces which are necessary to displace the beams by defined distances. Thus, we effectively calibrated the deflecting walls as Hooke's springs with a corresponding spring constant. The results are depicted in Figure 5.11(b) with the displacement as a function of the change in cell force. The black and red data points represent the experimental situation with and without the hydrogel, respectively. This discrimination is necessary because both conditions are applied in different experimental contexts and the presence of the hydrogel has a significant impact on the force which is required to deflect the walls inward. In the relevant displacement regime shown here, the relation is in good approximation linear and the corresponding slopes are indicated in the respective colors. The numerical calculations also reveal that initial deflections of the walls by several micrometers do not significantly influence the force which

is necessary to displace them. The data points are merely offset along the y-axis but the slope remains unaltered. As a result, the two conversion factors of $-242\,\mathrm{nN/\mu m}$ with the hydrogel and $-157\,\mathrm{nN/\mu m}$ without the hydrogel are used in the rest of this chapter to directly calculate forces from the experimentally observed beam displacements.

The numerical calculations can also be applied to predict the scaffold behavior and optimize the design based on the desired outcome. This approach is especially interesting to accelerate prototyping, e.g., in case of design changes to achieve other kinds of stimulation or if the system is adapted to other cell types.

5.4 Initial Contraction Force of Cells in the Scaffolds

In the previous section, I have introduced our approach based on numerical calculations to connect the experimentally observed beam displacements to changes in cell force. This essential relationship allows us to relate the results to other methods used to stretch cells in literature and to discuss our observations in the context of mechanobiology. At this point, all the necessary tools are available to study the behavior of cells in the stimuli-responsive host-guest microscaffolds.

As a first step, we analyzed the initial contraction forces of cells. Cells spreading in the scaffolds build up initial forces, similar to traction forces observed on 2D samples like micropost arrays [167] or traction force microscopy [168]. The transition to 3D environments, however, has significant effects on the behavior and the design restricts cells to only form adhesions on the four beams coated with fibronectin. To quantify initial contraction forces, it would be necessary to record time series of scaffolds during the invasion of cells. The beam displacements from empty scaffolds compared to the situation with cells in an equilibrium level could then be used to calculate the corresponding force change. However, as described in section 5.2.2, 360 scaffolds are placed on a single sample to observe multiple cells simultaneously. Thus, it would be required to record images of all these scaffolds with a sufficiently high temporal resolution to capture the cellular behavior. At the same time, only a portion of them are actually invaded by cells which spread on all four beams, so most of the images are not useful in the evaluation. For this reason, we reversed the approach and first incubated cells on the sample for three hours to give them sufficient time to reach their

new steady state. Next, we located all invaded scaffolds and started the image acquisition only for the respective positions. In the last step, we used trypsin to detach all cells from the scaffolds and simultaneously recorded the beam displacements. Since the beams move back to their original position, differences between the two states yield the initial contraction force of cells.

Figure 5.12(a) shows three exemplary bright-field optical images at different time points during such an experiment. Here, the blue arrows indicate beam displacements due to cell detachment, scaled by a factor of 10 for visibility. The corresponding track in panel (b) displays the averaged beam displacement in black along with the force change in green as a function of time. At the beginning of the experiment, the observed cell is in a stable state with small fluctuations in the contraction force. After addition of trypsin at minute 18, the cell is immediately detached from the scaffold. The arrows in the two optical images after the addition indicate a movement of the beams away from the center, which is reflected in by positive displacement. Correspondingly, the cellular contraction force quickly decreases by about 80 nN in the course of several minutes. Since the beams return back to their initial position before the cell was attached, this difference corresponds to the initial contraction force after the scaffold invasion. As no stimulation is required in this experimental setup, we used scaffolds without the host-guest hydrogel to accelerate the fabrication.

We performed several experimental series with two different cell lines, U2OS cells and NIH 3T3 cells. Details about the cell types can be found in section 3.6.1. Figure 5.12(c) shows the quantification of initial contraction forces where one data point corresponds to one cell with a respective track. Both cell types actively pull on the beams when they spread on the scaffolds, which leads to a positive initial contraction force. For U2OS cells in the equilibrium state, the initial contraction forces are (79 ± 50) nN and higher for the NIH 3T3 cells at (121 ± 48) nN.

Compared to previous experiments on flat substrates [168, 169] or dense micropillars [133, 167] these results are somewhat lower but on the same order of magnitude. Moreover, the values are in very good agreement to recent experiments with NIH 3T3 cells in rigid 3D microscaffolds [170]. In this publication, the force scale is defined by the one-dimensional modulus of peripheral stress fibers, which has been estimated from the 3D cell shape to be around 70 nN. For the scaffold design in this work, two arcs pull on one adhesion platform, i.e., one of the four beams of the scaffold. In this situation, forces twice as high are expected, which fits very well to the experimental

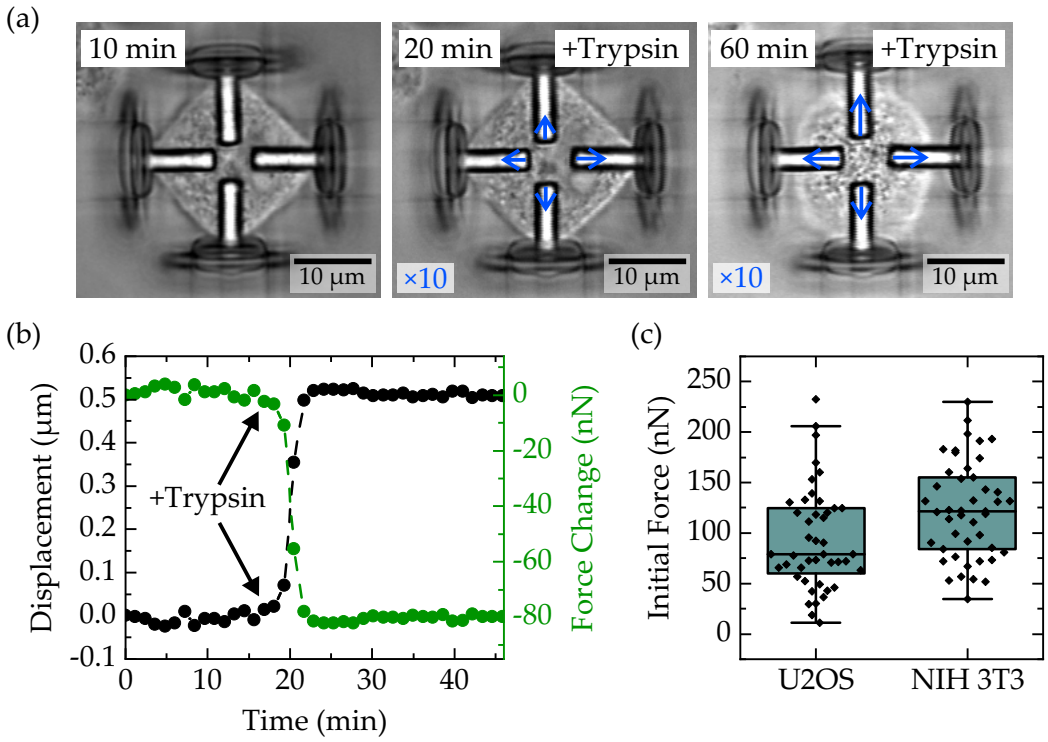

Figure 5.12: Initial contraction force of cells in scaffolds. (a) Exemplary bright-field optical images of a cell in a scaffold at different time points. Blue arrows indicate displacements of the beams (scaled by a factor of 10). After 18 min, trypsin is added to detach the cell. (b) Corresponding displacement (black) and force change (green) as function of time. (c) Quantification of initial contraction forces for U2OS and NIH 3T3 cells. Each data point here and in all subsequent quantifications corresponds to one cell in a scaffold. The solid line denotes the median values with the lower and upper quartile indicated by the box. The whiskers show the maximum an minimum data points which are still within 1.5 times the inter quartile range. Adapted from [34].

observation. The results also fit well to other, more similar approaches like NIH 3T3 cells spreading between cantilever and substrate [145]. Generally, there is a distinct difference between cells in 2D and 3D environments which can be attributed to two effects: First, the cell shape in 3D is more roundish compared to the strongly pinned and flattened cell shape in 2D, leading to larger distribution of the forces [170]. Second, the number of adhesion sites in the 3D scaffolds is limited to the four beams coated with fibronectin. In the following sections, I focus on the results of U2OS cells but additional data for the NIH 3T3 cells can be found in appendix A.1.

5.5 Cellular Reaction to Stimulation

The analysis of initial contraction forces of cells in 3D scaffolds is the basis for further investigations of the cellular response to mechanical stimulation. In this section, I present our results on the tensional homeostasis, i.e., the cellular process to adapt to an external stimulation, of individual cells as a reaction to defined equibiaxial stretches. I discuss the cellular adaptation to a new dynamic setpoint as well as the impact of the stretch in detail. In the last part, I show control experiments to assess the possible influence of 1-AdCA on the cellular behavior.

5.5.1 Tensional Homeostasis after Mechanical Stretching

To investigate the cellular response to mechanical stretches, we used the stimuli-responsive 3D scaffolds with the host-guest hydrogel. After seeding cells on the sample, we incubated them for three hours to give them sufficient time to spread on the structures and build up adhesions on all four beams. In the following steps, we first applied a defined equibiaxial stretch and subsequently released it by exchange between culture media with and without competitive 1-AdCA guest molecules. Over the whole course of the experiments the beam displacements were tracked to analyze the cellular response.

Figure 5.13(a) depicts bright-field optical images of an exemplary cell in a scaffold during different experimental stages. Red and blue arrows indicate individual beam displacements due to the hydrogel stimulation and the cellular reaction, respectively. The track over the complete course of the experiment is depicted in panel (b) with numbers indicating the time points of the corresponding optical image.

After spreading on the scaffold, the cell establishes an initial contraction force (1) as discussed in detail in the previous section. At this point, we started the image acquisition to record the cellular behavior in the steady state. Addition of medium containing 1-AdCA at minute 12 triggered the hydrogel expansion and led to an equibiaxial stretch of 1.5 µm on each beam (2). As a response, the cell actively counteracts this external deformation and starts to pull on the beams. Around 30 min later, the displacement stabilizes again on a new level which is 0.31 µm lower than immediately after the stimulation (3). This behavior can be observed in more detail in

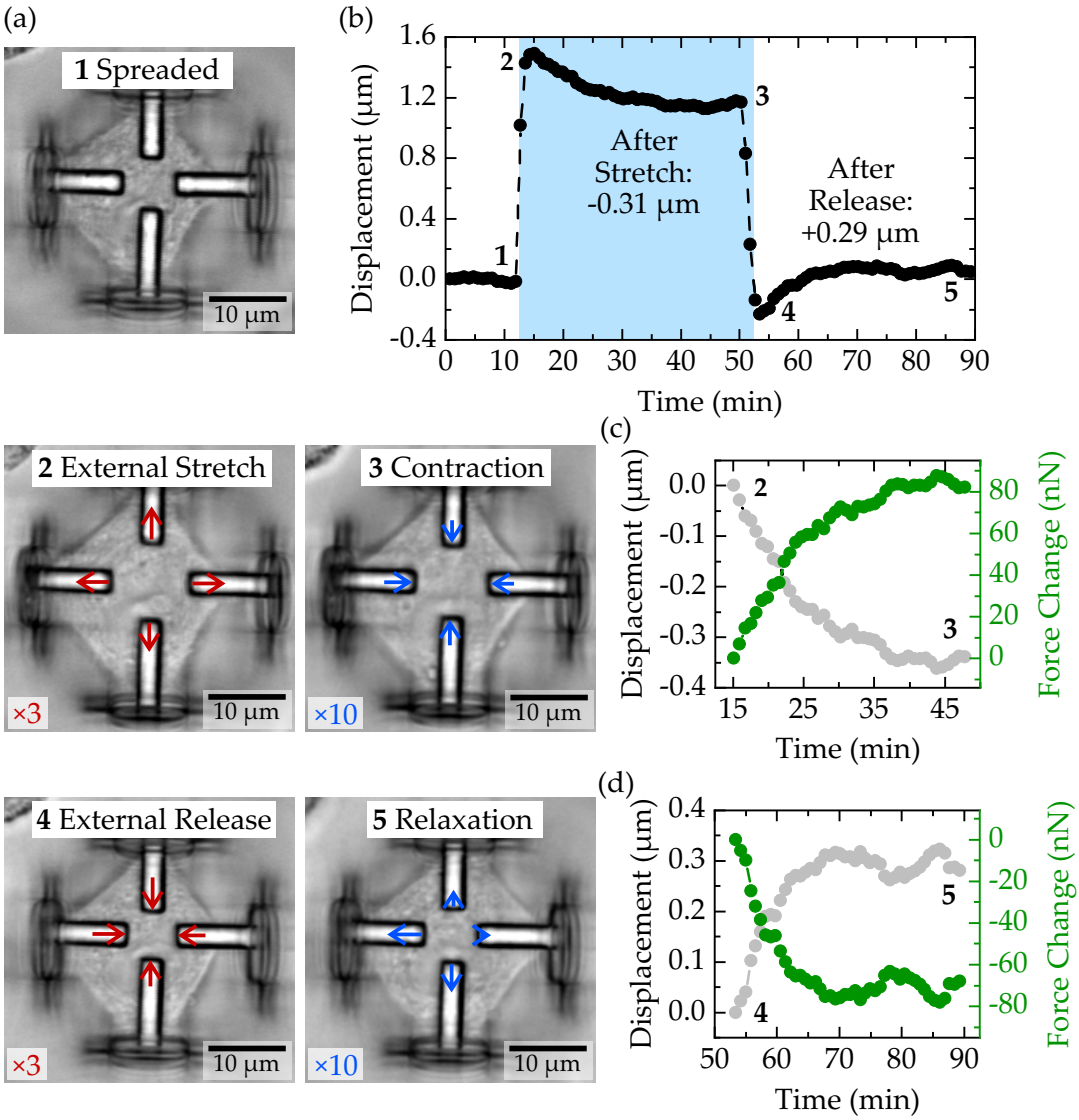

Figure 5.13: Cellular reaction to an external stimulation. (a) Bright-field optical images depict a cell during the different phases of a stimulation experiment. Red arrows denote external displacements of beams by the stimuli-responsive hydrogel and blue arrows displacements by cellular forces, both scaled with the respective factors. First, the cell spreads in the scaffold (1) and is stretched by expansion of the stimuli-responsive hydrogel (2). Next, the cell contracts and pulls the beams back towards to center (3). After release of the external stimulus (4), the cell relaxes and the beams move back to their initial position (5). (b) Corresponding average beam displacement as a function of time. Numbers indicate the corresponding optical images at different time points. (c)-(d) Enlarged sections of the response after the stretch and release with the displacement in gray and the force change in green. Adapted from [34].

Figure 5.13(c) which depicts an enlarged section of this time period. The conversion of displacements to force changes reveals the immediate increase of cellular contraction forces after the stimulation to a new level which is about 80 nN higher than after the stretch.

After the cell established this new equilibrium, we changed to pure cell culture medium to release the external stimulation. Immediately after the stretch is lifted, the beams move back towards the center by 1.5 µm and the measured displacement is lower than at the beginning of the experiment since the cell is still exerting an additional contraction force. Over the course of the next 30 min, however, the cell relaxes and the contraction force decreases again by about 70 nN (see Figure 5.13(d)). As a result, the new steady state at the end of the experiment is very close to the initial value at the beginning.

To quantify this behavior, we analyzed over 100 cells with the results summarized in Figure 5.14(a). Each data point corresponds to one cell which was studied during a stretch-release cycle as introduced in Figure 5.13. The displayed values correspond to the force change 30 min after the stretch and after the release, respectively. In summary, cells counteract the external deformation by actively increasing their tension. They stabilize on a new equilibrium setpoint where contraction forces are increased on average by (74 ± 41) nN compared to the initial level. 30 min after the external stimulation is lifted, cells relax again and the additional contraction forces are relieved. As a result, the average force change after release is negative with (-69 ± 57) nN.

This cellular process to adapt to new situations after external stimulation is known as tensional homeostasis in literature [171, 172]. Our results, however, support recent findings that tensional homeostasis does not necessarily cause cells to return to their initial setpoint [145, 173]. They rather adjust to the changed environment and stabilize around a new, tunable force setpoint. As a consequence, cells keep the new level as long as the external stimulation is active and eventually restore the initial tension when the external stretch is removed. To highlight this aspect, we also analyzed the force deviation of individual cells from the end of the experiment to their respective initial levels. The data points depicted in Figure 5.14(b) show a distribution around zero, thus indicating that cells restore a similar level of contraction forces if confronted with the initial external situation.

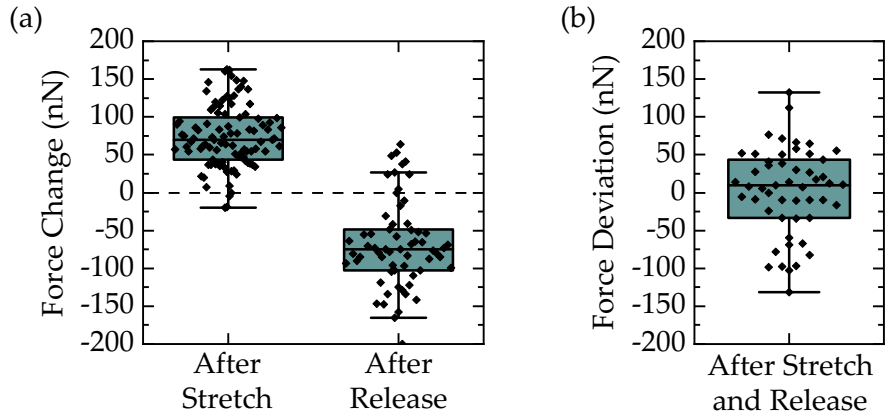

Figure 5.14: Quantification of the cellular response. (a) Change in cellular contraction forces 30 min after the stretch and after the release, respectively. Each data point represents an individual cell analyzed during a stretch and release cycle. (b) Force deviation of individual cells at the end of the experimental cycle from the initial steady state at the beginning of the experiment. Part (a) adapted from [34].

5.5.2 *Stabilization on a New Dynamic Setpoint*

To validate and support the previous findings, we conducted additional experiments to study specific aspects of the cellular response. First, we analyzed cells exposed to an extended stretching period as depicted in Figure 5.15. As discussed previously, the cells counteract the deformation and pull the beams inward by increasing their contraction forces. In this example, the new stable equilibrium level is reached after around 20 min. For the quantifications shown in the previous section, we have chosen the value after 30 min to allow the majority of the cells to reach a steady state.

This new force setpoint is maintained for at least one hour after its establishment. Small fluctuations of the data points around this setpoint indicate the constant readjustments of the cell. Since these variations have an impact on the resulting displacements, we extracted the displacement values from exponential fits to the data as indicated by the red dashed line. Furthermore, we corrected for minor external perturbations of the hydrogel response, by subtracting the track from a reference scaffold. For this reason, we always recorded the response of an empty scaffold without a cell in the same 3×3 fabrication field where the scaffold with the cell was located.

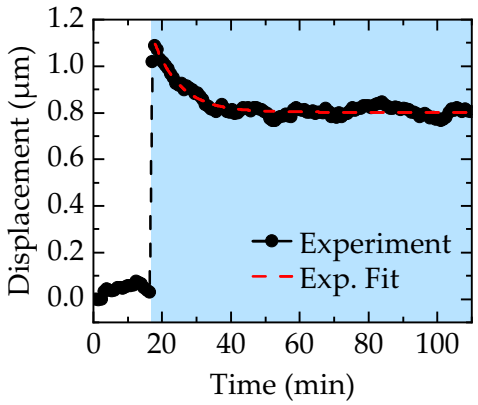

Figure 5.15: Cellular adaptation after the stretch. Average beam displacement as a function of time for a cell which is stretched after 18 min. The cell pulls the beams back as a response and cellular contraction forces increase. After 20 min of stimulation, the forces stabilize with small fluctuations around the new equilibrium level. Adapted from [34].

5.5.3 *Response to Different Stimulation Intensities*

Next, we looked at the reaction of cells to different stretching levels. The data depicted in Figure 5.16 shows the force change 30 min after the stimulation for increasing external deformations from left to right. Here, it is important to note that our stimuli-responsive scaffolds do not stretch cells by constant displacements but rather apply constant forces exerted by the swelling hydrogel. As a consequence, observed displacements due to the external stretch can vary as a function of the cell stiffness. For clarity, we binned the data in groups ranging from 0.5 µm to 3.0 µm per beam, corresponding to 4 % and 24 % equibiaxial stretch, respectively.

In all cases, cells show the tensional homeostasis behavior and stabilize on a new setpoint by increasing their contraction forces. The individual cell responses lead to a variation of the data points within each group. Nevertheless, the median values of each group (black lines) are close to the overall median value of the whole dataset (dashed blue line) with no statistically significant differences. At the same time, the individual tracks show that cells are not able to recover their initial shape, even for the small stretches from $0.5 - 1.0$ µm. This leads to the possible conclusion that the observed changes in contraction forces are the maximum possible adjustments for U2OS cells in the given experimental setting.

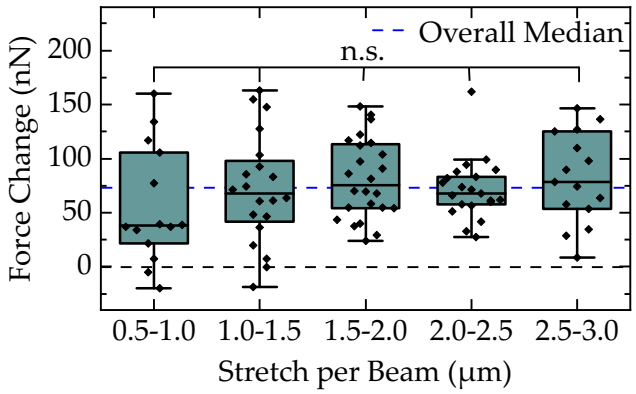

Figure 5.16: Impact of stimulation intensity. Force change of cells after reaction to different levels of stretches. The data was binned in groups from 0.5 µm to 3.0 µm stretch per beam, which corresponds to 4 % and 24 % equibiaxial stretch, respectively. The blue dashed line depicts the median for the complete dataset. The quantification shows no significant (n.s.) impact of the stretch intensity between the studied intervals. Adapted from [34].

5.5.4 *Influence of 1-AdCA on Cellular Response*

Another important aspect is the influence of 1-AdCA on the behavior of cells. As discussed previously, it is very important to suppress unwanted side effects to study cellular mechanisms in detail. For this reason, we performed several control experiments and quantified the results as depicted in Figure 5.17.

In all three experiments, the force change after 30 min compared to the initial level was evaluated. In the first control, we analyzed the cellular response in scaffolds without further external stimulation. The dataset shows a small variation around zero which can be attributed to the dynamic cellular regulation around this setpoint as, for example, observed in the steady state depicted in Figure 5.15. The second data set summarizes the response of cells to the external stretch triggered by addition of medium containing 20 mM 1-AdCA. These results are discussed in section 5.5.1 in detail. However, both the mechanical stretch and the 1-AdCA molecules could have an impact on the observable cellular response. For this reason we performed additional experiments with control scaffolds without the host-guest hydrogel. These scaffolds were placed on the same samples as the stimuli-responsive scaffolds to keep all other experimental parameters

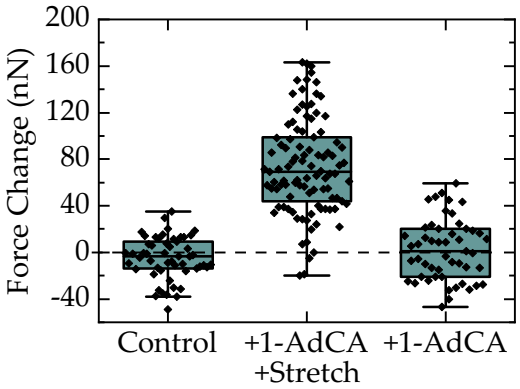

Figure 5.17: Influence of 1-AdCA on cellular behavior. Changes in contraction forces for cells in the scaffolds under different conditions. In the control, cells were tracked for 30 min with no external influences. The second column depicts the cellular reaction after a stretch as presented in Figure 5.14. For the last condition, cells in control scaffolds without the host-guest hydrogel were used to investigate the role of 1-AdCA independent of the mechanical stimulation. The quantification shows no significant influence of the addition of 1-AdCA on the cellular response. Adapted from [34].

constant. As a result, cells were exposed to the 1-AdCA medium but did not experience a mechanical stimulation. The quantification in the third column of Figure 5.17 shows again a variation of the data set around zero, similar to the control experiment without any external influence. Consequently, addition of 1-AdCA in the medium has no significant effect on the cellular response.

In an additional experimental series, we investigated the cell viability in medium containing 1-AdCA over extended periods of time. Therefore, we cultured U2OS cells on glass slides coated with fibronectin in medium with and without 10 mM of 1-AdCA. The concentration was chosen to mimic an experimental setting where cells are alternately stretched and released multiple times. After 24 hours, we fixed the cells and performed a live/dead staining. Exemplary images of both conditions as well as the quantification of the staining are depicted in Figure 5.18. The results show no significant differences between both conditions, further highlighting the viability of cells in the presence of the competitive guests.

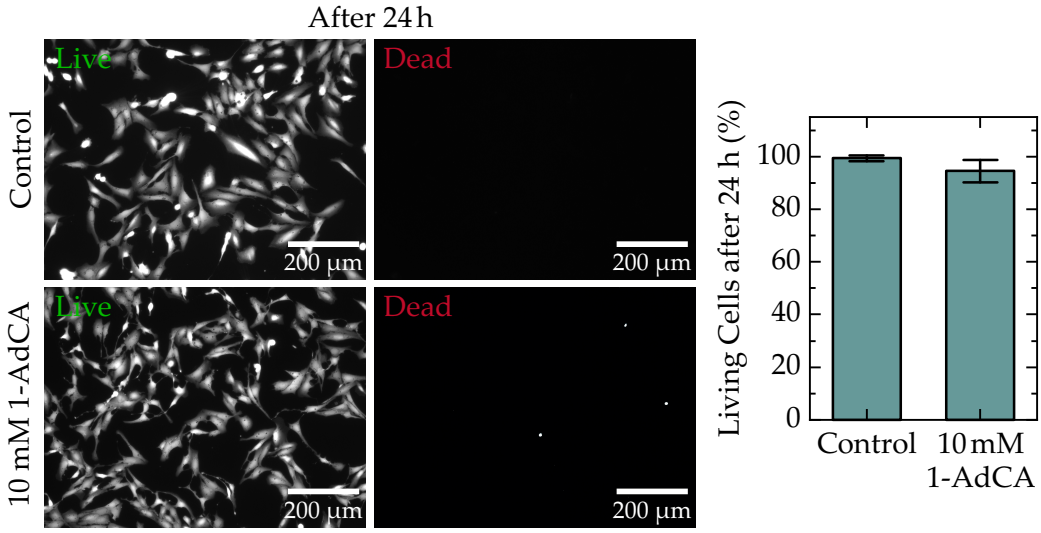

Figure 5.18: Cell viability in medium containing 1-AdCA. Exemplary images of a live/dead staining of U2OS cells, cultured for 24 hours in medium with and without 10 mM 1-AdCA. The quantification shows no significant differences between treated cells ($N = 1930$) and untreated control cells ($N = 2345$). Adapted from [34].

5.6 Inhibition Effects on Cellular Behavior

In the previous section, I have discussed the cellular response to mechanical stretching in stimuli-responsive scaffolds. In the next step, we investigated whether the observed behavior primarily results from actomyosin contractility, from passive elements like cytoskeletal crosslinkers, or a combination of both [174]. To answer this question, we analyzed the impact of ROCK inhibition and additionally repeated the experiments with a U2OS knock-out cell line which lacks the non-muscle myosin IIA (NM2A) protein (see section 3.6.1). We have chosen this approach to distinguish between active actomyosin contractility and passive actin stability. Both, ROCK and its downstream target NM2A are known to be crucial for the generation of cellular contractility in general [46, 175]. The knock-out of NM2A, however, is more specific and solely effects the actomyosin contractility by blocking the corresponding motor activity. On the other hand, the ROCK signaling pathway acts bidirectional, affecting both actomyosin contractility as well as actin stability [176, 177].

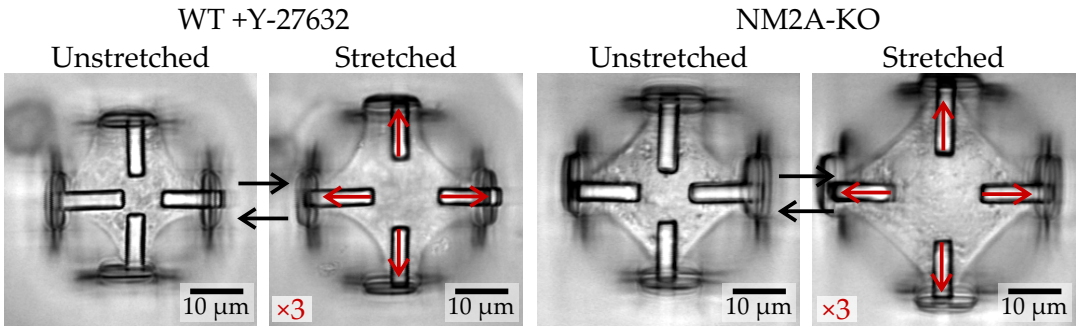

Figure 5.19: Bright-field optical images of U2OS wildtype (WT) cells treated with 50 µM Y-27632 (ROCK inhibitor) and U2OS NM2A-KO cells in the unstretched (left) and stretched (right) state. Red arrows indicate the external stretch scaled by a factor of three. Adapted from [34].

Figure 5.19 shows bright-field optical images of U2OS cells treated with the ROCK inhibitor Y-27632 (left) and NM2A-KO cells (right), both in the unstretched and the stretched state. Even though both conditions have severe effects on the contractility, cells still spread on the four beams and stay attached to them over the course of the experiment.

In a first step, we studied the initial cellular contraction forces in the scaffolds. For the NM2A-KO cells, we followed the same protocol as described in section 5.4 and released the cells by addition of trypsin after they established a steady state. In case of the ROCK inhibition, we first treated cells in the scaffolds with 50 µM Y-27632 and observed their behavior for 15 min. In this time period, we recorded similar time vs. displacement curves as depicted in Figure 5.12 after addition of trypsin. Thus, contraction forces are significantly reduced but the cell stays attached to the four beams of the scaffolds as shown in Figure 5.19. Afterwards, we continued the experiment by adding trypsin to detach the cells from the four beams to measure the remaining contraction forces. Figure 5.20(a) depicts the quantification of these experiments in comparison to U2OS wildtype (WT) cells. In both cases, the initial forces are drastically reduced from (79 ± 50) nN in the WT scenario to (3 ± 3) nN and (11 ± 12) nN for the ROCK inhibition and the NM2A-KO cells, respectively.

In the following experiment, we investigated the response during a stretch-release cycle as introduced in the previous section. Figure 5.20(b) shows a typical beam displacement as a function of time for a NM2A-KO

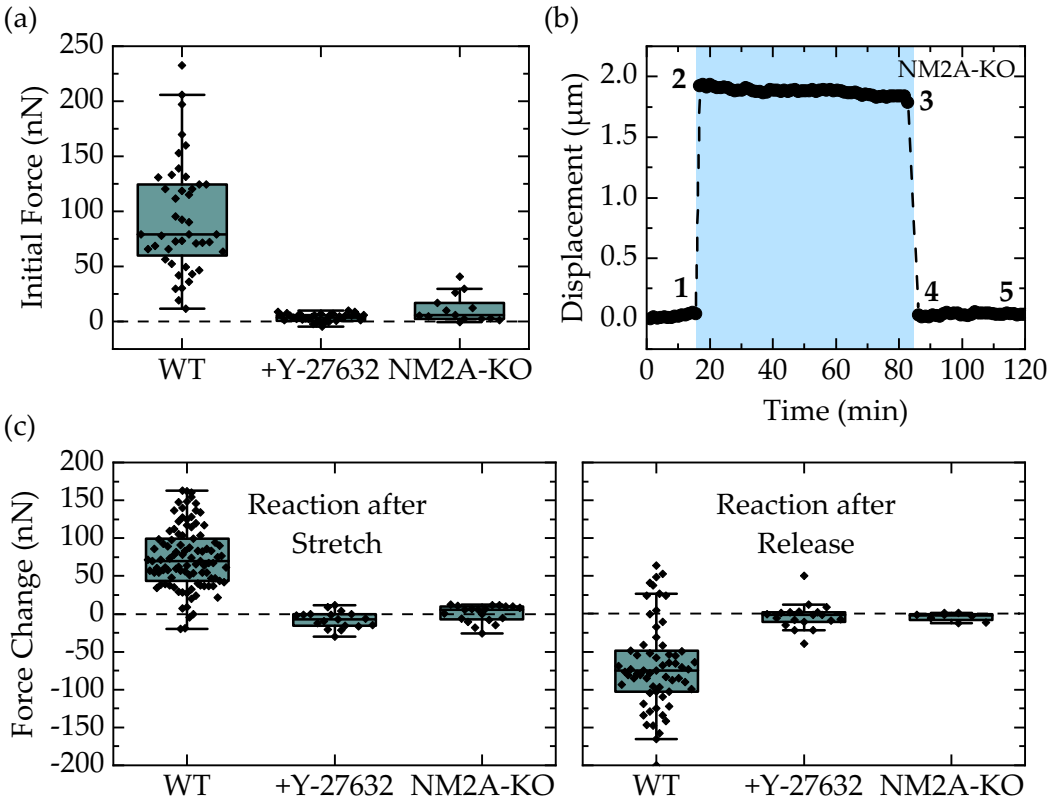

Figure 5.20: Inhibition effects on cellular behavior. (a) Initial contraction forces for different conditions. For both, the ROCK inhibitor Y-27632 treated and the NM2A-KO cells, contraction forces are drastically reduced compared to the WT case. (b) Exemplary displacement as a function of time for a NM2A-KO cell during a stretch-release cycle. The numbers indicate the corresponding time points in Figure 5.13(a) as a comparison. (c) Force change as a reaction after the stretch and after the release for different conditions. Cells treated with the ROCK inhibitor and NM2A-KO cells completely lose their ability to adapt their contraction forces as a response to the external stimulation. Adapted from [34].

cell over the course of the experiment, although the tracks look similar for the ROCK inhibited cells. The numbers correspond to the different phases in the experiment introduced in Figure 5.13 for comparison. After stretching, the displacement is stable at a new level and even over the course of 60 min no significant cellular reaction is observable (2-3). Likewise, after the stretch is lifted, the beams immediately return to their initial position and maintain this state (4-5). Consequently, the ability of the cell to react to this external stimulation is significantly disturbed.

The quantification of this effect is summarized in Figure 5.20(c). Both, the force change after the stretch and after the release are drastically reduced compared to the WT situation and close to zero. Furthermore, there is no statistically significant difference between the two conditions, similar to the evaluation of initial forces.

5.7 Reorganization of the Actomyosin Machinery

In the experiments presented in the previous section, we found a substantially reduced response of ROCK-inhibited and NM2A-KO cells to mechanical stimulation. These results indicate that cellular homeostasis strongly depends on actomyosin contractility. Therefore, we investigated the impact of stretching on the morphology and organization of the actomyosin cytoskeleton. We performed immunocytochemical stainings to study the actin fiber organization and NM2A localization for cells in the unstretched and the stretched state. To achieve this, we added 1-AdCA to all solutions which are required for the fixation and staining protocols (see section 3.6.2). This allowed us to keep the whole system, including hydrogel, scaffold, and cell in the stretched state for further analysis. After this treatment, the sample is stably fixed and can be either imaged in any microscope system without special equipment or stored for later usage.

Figure 5.21 depicts exemplary immunocytochemical stainings of actin, NM2A, and the cell nucleus for U2OS WT cells in the unstretched (top) and stretched (bottom) condition. Furthermore, the walls of the scaffolds are visible in the DAPI channel since TPETA is weakly auto-fluorescent in this wavelength regime. We compared cells on the same sample in control scaffolds without the hydrogel with cells in stimuli-responsive scaffolds. In this way, we were able to keep all further experimental influences constant and cells were exposed to the same medium containing 1-AdCA. The cells were fixed 30 min after the medium containing 1-AdCA was added.

The comparison of both conditions reveals the strong emergence of actin stress fibers after the mechanical stimulation. Furthermore, these new fibers display a high degree of organization and are very well co-localized with NM2A. Stretched U2OS WT cells form new stress fibers along the contour but also in the cell interior to connect opposing beams, which are barely present in the unstretched state. The comparison to NM2A-KO cells as depicted in Figure 5.22 shows, however, that this behavior can no longer be observed if

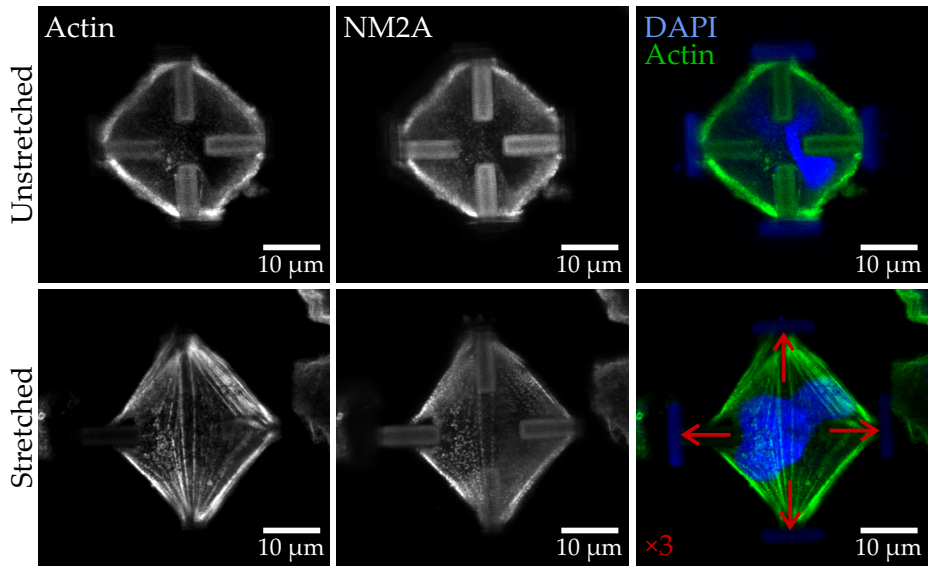

Figure 5.21: Reorganization of actin filaments in U2OS WT cells. The images depict immunocytochemical stainings of actin, the cell nucleus and NM2A in the unstretched and stretched condition. The cells were fixed 30 min after the medium 1-AdCA was added. Red arrows indicate the displacement of individual beams, scaled by a factor of three. After the external stimulation, cells build up a significant amount of actin fibers with a high degree of organization. Adapted from [34].

NM2A is knocked out. These cells show a significantly weaker response to the stimulation. Even though stretching still leads to the emergence of new actin stress fibers, they are shorter and much less organized.

This behavior fits well to the experimental results presented in section 5.5 and 5.6. U2OS WT cells build up new stress fibers to increase their contraction forces and thus counteract the externally imposed deformation. NM2A-KO cells, on the other hand, are no longer able to react to the stretch and can not generate additional contraction forces. These results suggest that cellular homeostasis is primarily generated by actomyosin contractility, rather than by cytoskeletal crosslinkers. These passive elements are apparently not sufficient to generate sufficient forces to counteract the mechanical deformation.

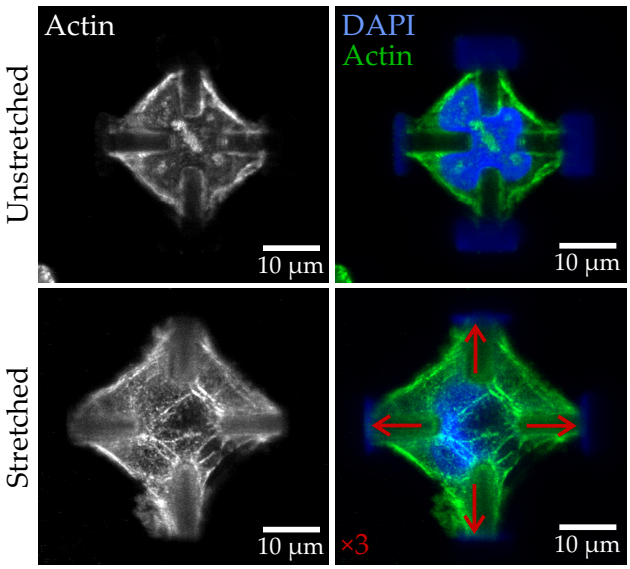

Figure 5.22: Reorganization of actin filaments in U2OS NM2A-KO cells. Immunocytochemical stainings of actin and cell nucleus for the unstretched and stretched condition. Red arrows indicate the displacement of individual beams, scaled by a factor of three. The external stimulation leads to the emergence of short and unorganized actin fibers. Adapted from [34].

5.8 Asymmetric Stimulation on One Side

All experiments so far have been based on the scaffolds introduced in section 5.2.1. The fabrication via 3D laser lithography, however, offers an inherent flexibility to change the design and thus the stimulation experienced by cells. This opens further opportunities to study the cellular response under different conditions. In this section, I present a possible modification to asymmetrically stretch cells on only one adhesion site and discuss the results on the cellular behavior.

Figure 5.23(a) shows the schematic design we used to achieve an asymmetric stretch on the left side. Compared to the previous scaffolds, we increased the thickness of three walls substantially. As a result, they are too stiff to bend significantly and the swelling hydrogel is solely displacing the remaining thin wall on the left-hand side. The resulting track for a cell during this stimulation is depicted in Figure 5.23(b). Here, the individual beam displacement for the four sides are displayed as a function of time. Injection of medium containing 1-AdCA leads to a significant displacement of the left beam, whereas the other four beams only experience a minor response.

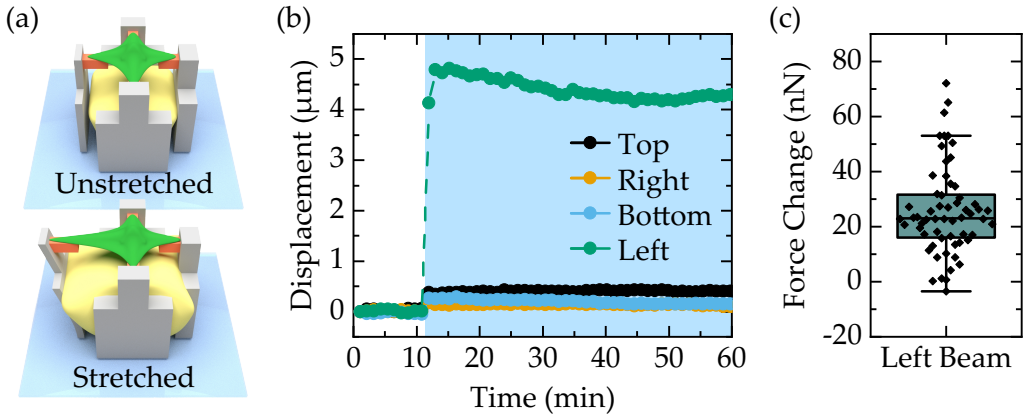

Figure 5.23: Mechanical stretch on one adhesion site. (a) Schematic images of the design with three thick walls and one thin wall on the left-hand side. As a result, the expanding hydrogel only displaces the left wall and stretches the cell asymmetrically. (b) Displacements of the four individual beams as a function of time for a cell which is stimulated by a stretch on the left beam. (c) Change in contraction forces on the left beam after stimulation. Adapted from [34].

Since the confinement by three walls restricts the swelling, the hydrogel exerts a stronger pressure on the remaining thin wall on the left-hand side. As a result, displacements of up to 5 µm on an individual adhesion site are achieved for the same 1-AdCA concentration of 20 mM.

The cellular response can be observed in the displacement after the external stimulation. Similar to a stretch on all four sides, the cell counteracts the stimulation by increasing its contraction forces and stabilizes on a new equilibrium level. In case of the asymmetric stretch on the left-hand side, however, the cellular reaction is focused solely on the left beam. The quantification of force changes in this experimental setting is depicted in 5.23(c). 30 min after the stretch, cellular contraction forces on the left beam increase by (26 ± 16) nN. This value is similar to the force increase per beam of (19 ± 10) nN which we observed for an equibiaxial stretch as discussed in section 5.5.1. Thus, we conclude that this particular design with an asymmetric stimulation does not lead to a significant increase of cellular contraction force, even though it is focused on only one adhesion site of the cell. At the same time, these results are in good accordance with our conclusion in previous sections that the ability of U2OS cells to increase their contraction forces to adapt to the external stimulation is limited.

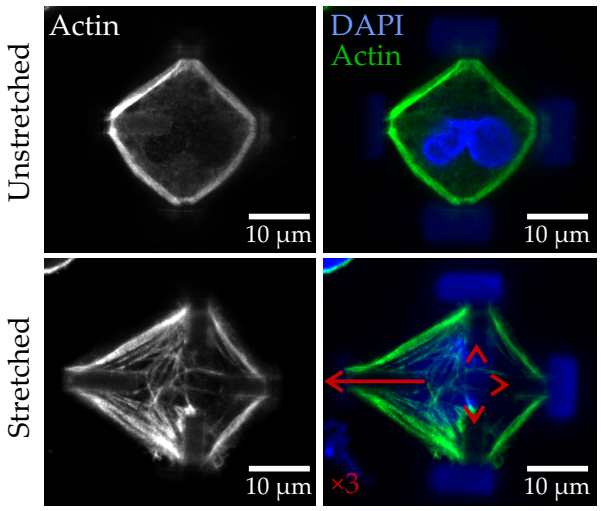

Figure 5.24: Actin reorganization after an asymmetric stretch. The immunocytochemical stainings of actin and the cell nucleus exemplarily show the actin cytoskeleton in the unstretched and stretched condition. Red arrows indicate the displacement of individual beams, scaled by a factor of three. Only the left beam is significantly displaced and new actin fibers dominantly form on this side of the cell as a response to the stretch. Adapted from [34].

Since the cellular response is focused on only one displaced side, we analyzed whether the remodeling of actin fibers also reflects the behavior we found in the previous experiments. Similar to section 5.7, we performed immunocytochemical stainings of actin and the cell nucleus as depicted in Figure 5.24. The comparison of cells in the unstretched and stretched condition clearly shows the emergence of additional stress fibers with a high degree of organization as a response to the stimulation. Compared to the equibiaxial stretch, however, the majority of new actin fibers is now localized on the left side of the cell which has been displaced.

These results highlight the ability of the fabrication process by 3D laser lithography to adapt the scaffold design to enable a variety of different experimental conditions. Moreover, as already demonstrated in previous sections, several different designs can be placed on a single cover slip along with respective controls. This aspect effectively parallelizes the experimental workflows and enables a high throughput four quantitative analysis.

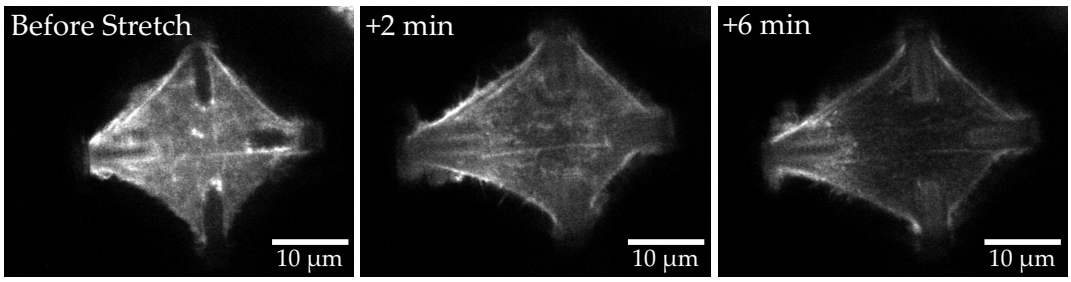

Figure 5.25: Live reorganization of the actin cytoskeleton. Fluorescent images of cells expressing TagGFP labeled β-actin at different time points before and after the external stretch is applied on the left beam at minute 0. The asymmetric stimulation leads to a strong emergence of new fibers on the left-hand side within several minutes.

5.9 Fluorescent Live Cell Imaging

The immunocytochemical stainings presented in the previous sections provide important insights in the reorganization of actin stress fibers after mechanical stimulation. However, they capture only a snapshot of this very dynamic process we observe in the live cell experiments. To take a closer look on the times-scales of the rearrangement process, we used a U2OS cell line, where a fluorescent GFP-Tag is fused to β-actin (see section 3.6.1) and performed fluorescent live cell imaging.

Figure 5.25 shows three exemplary images of the actin signal before and after the mechanical stimulation at 0 min. For these experiments, we used asymmetric scaffolds as introduced in the previous section. By comparison of the stretched region to the rest of the cell, we were able to better distinguish the cellular response to the stretch from additional unwanted effects like bleaching. Two minutes after the stretch, the reorganization of actin fibers is already in process, with new stress fibers forming dominantly in the left, displaced side of the cell. After six minutes, the asymmetry in the GFP signal becomes even stronger. At this point it is important to remember that cells typically need 20 to 30 min to reach a new equilibrium after the stretch (see section 5.5.1). Thus, these results show how the stress fiber formation precedes the generation of additional contraction forces.

Although fluorescent live cell imaging is a powerful tool to investigate these processes, several side effects can influence the results and conclusions have to be drawn with caution. First of all, bleaching of the fluorescent tags

is a significant problem. To capture the dynamic behavior, it is necessary to record images in short time intervals. But even though we have only recorded one image per minute, the GFP signals depicted in Figure 5.25 degrade rapidly. This effect is further accelerated because the signal to background ratio is generally low and thus high excitation laser powers are required. One reason is the GFP tag of the cell line linked to all available actin molecules compared to a staining of fixed cells with phalloidin, which only labels actin filaments assembled to stress fibers. This leads to a significant background staining in the cellular body as shown in the first images before the stretch. Another consequence of applying high excitation laser powers is an increased phototoxicity for cells, resulting in additional stress during the experiment. Therefore, it is important to consider that the cellular behavior in live cell experiments might be altered by the light exposure itself. In summary, although the method is promising to study the fast dynamics of the actin reorganization during the stretch, more work has to be done to extract reliable quantitative results from these experiments.

5.10 Discussion

In this chapter, I have presented a novel stimuli-responsive material system for 3D laser lithography based on host-guest complexes. In combination with conventional, non-responsive materials, we fabricated and characterized 3D microscaffolds for the mechanical stimulation of single cells. Furthermore, we calibrated this system by numerical calculations to establish the correlation between experimental displacements and cellular forces. We applied these scaffolds to study the cellular response to defined mechanical stimulations in a 3D environment.

In a first step, we studied the behavior of cells during the scaffold invasion. By establishing adhesion sites on the four protein coated beams, they build up initial contraction forces of (79 ± 50) nN and (121 ± 48) nN for U2OS and NIH 3T3 cells, respectively. We found that both, inhibition of the ROCK pathway or knock-out of NM2A, lead to a drastic reduction of contraction forces, which is in accordance to previous studies in literature with conventional 2D methods like traction force microscopy [178, 179].

Next, we focused on the dynamic response of cells during mechanical stimulation. We revealed how cells counteract an external stretch by actomyosin generated contractility, an effect which has been described as tensional homeostasis [171, 180]. Although different studies show similar

trends regarding the cellular response, the amplitude is different. Weng *et al.* report that cells completely return to their initial state after the stimulation in their experimental setup [181], whereas Webster *et al.* demonstrate that cells can establish a new steady state after 20–30 min [145]. In our experiments, we find that both, U2OS and NIH 3T3 cells, increase their contraction forces after the stimulation and plateau at a new setpoint. Furthermore, we observed no significant differences in the cellular response after application of equibiaxial stretches between 4–24 %, corresponding to beam displacements of 0.5–3.0 µm on all four sides. Although these results support the findings of Webster *et al.*, the experimental approaches vary and different cell types can respond differently to mechanical stress. Additionally, we were able to study the cellular response after the stretch is released in our system. Cells are able to re-adjust their contractility in a time frame of 30 min and find a new equilibrium which is remarkably close to the initial setpoint. A similar behavior was observed by Ezra *et al.* for tarsal plate fibroblasts [173]. These results highlight the ability of cells to constantly and rapidly adapt their actomyosin machinery to changes in the cellular surrounding. As our scaffold system enables the quantitative analysis with a high throughput, future studies could analyze the transition between these states in more detail.

Another important feature of our approach is the ability to maintain cells in the stretched state for fixation and staining. That way, we were able to reveal a striking reorganization of the actin filaments as a response to the mechanical stimulation. After the stretch, cells build up a significant amount of new actin stress fibers between adhesion sites in the cell contour but also in the cell center. Although the emergence of new stress fibers was observed in both cell types, the actin fibers were shorter in NM2A-KO cells and lacked the clear organization and alignment compared to U2OS WT cells. In combination with our findings that NM2A-KO cells are no longer able to counteract mechanical stretches, these results imply that tensional homeostasis is a process strongly driven by active tension generation of NM2 motor proteins. Previous studies on smooth muscle myosins have shown that these motor proteins adapt their filament size in a load-dependent manner [182]. The different NM2 isoforms, on the other hand, are known to be the main drivers of intracellular forces in non-muscle cells and have a significant influence on the actin stress fiber organization and dynamics [183]. Thus, a similar behavior might arise from NM2B and NM2C. While initial experiments shown in appendix section A.2 indicate a similar but

weaker role of NM2B, a detailed systematic investigation of these isoforms could foster a deeper understanding of the molecular mechanism of cells to regulate tensional homeostasis.

Although our results favor a model in which actomyosin contractility is the most important mechanism behind tensional homeostasis, the passive actin architecture might still contribute to this process in a more subtle way. Theoretical models have shown previously how optimal force configurations are only achieved by balancing active motors and passive crosslinkers [174]. Thus, more detailed investigations of specific crosslinkers like α-actinin could contribute to an even better understanding of the regulating mechanisms of this process.

In one of the last presented experiments, we highlighted the flexibility of the 3D laser lithography approach by demonstrating an alternative design to stretch cells on only one adhesion site. Here, we were able to show that an asymmetric stimulation also leads to an asymmetric response in the force generation as well as the actin filament reorganization. The introduced geometry, however, is only one possible scaffold design which could be used to address various cell biological questions in the context of mechanobiology in the future. The continuous assembly and disassembly of actin stress fibers in response to mechanical stress, for example, is a long-standing topic of interest. The questions whether mesenchymal-like cells also form stress fibers in physiolocigal 3D environments and whether these fibers differ from their counterparts observed on rigid 2D substrates like glass coverslips are still unanswered [184, 185]. Here, our system in combination with fluorescent markers like F-Tractin or Lifeact could provide a powerful platform to study the assembly of stress fibers in a 3D environment as indicated in the last experimental section of this chapter.

Despite the various biological questions that can already be addressed with this method, further optimizations in the fabrication procedure could make it more accessible to potential users. In its current state, the three consecutive writing steps which require partially manual alignments render the whole process complex and time consuming. In this regard, one aspect with potential for large improvements is the host-guest resist composition. The mixture used in the scope of this thesis requires a pre-baking step before it can be effectively polymerized, which could be eliminated by further modifications in the recipe. This would increase the reproducibility of the process since the exact baking time depends on external factors like humidity which are difficult to control. Even more important, however, would be the ability to use a microfluidic device as recently presented by our group [116]

to enable a fully automated sample fabrication and development. Since it would no longer be necessary to remove the sample between the individual processing steps, the alignment becomes obsolete and the whole process could be accelerated significantly.

A second very interesting aspect which looks at the problem from a different perspective is the question of re-usability of the scaffolds. Typically, samples fabricated with simple structures for cell experiments are used for one experiments and afterwards disposed. For the complex multi-material scaffolds we presented in this work, however, it would be worth an additional effort if the samples could be used multiple times. As we have shown in the experiments in this chapter, the stimuli-responsive behavior itself is completely reversible. Furthermore, it is easily possible to remove cells from the scaffolds by treatment with trypsin. The remaining challenge which needs more attention in the future is the repeated surface coating with ECM proteins to provide suitable environments for cellular adhesions on the scaffolds. Here, a chemical or temperature treatment could restore the polymer surface to a state which again allows protein adsorption. Progress in this direction could ultimately allow other groups to effectively use this method without access to a 3D laser lithography setup at all.

Yet another starting point is the optimization of the cell seeding procedure. In the current state, a certain number of cells is dropped over the sample region where the scaffolds are located. Whether a cell actually falls into the scaffold and adheres to it, however, is a random process and could, in principle, be improved by seeding a larger number of cells. On the other hand, if the cell density is too high, more than one cell attaches to a scaffold. As a result, the yield of cells which are attached to all four beams and can be used for further analysis is typically around 5–10 % but considerably varies from experiment to experiment. Although the throughput with the corresponding number of about 25 cells per sample is still high compared to other methods, most of the fabricated scaffolds remain unused. Here, further modifications of the seeding conditions might still significantly increase this number. Thinking one more step ahead, it would even be possible to incorporate cell-printing methods with the ability to automatically place cells in the individual scaffolds. In summary, the most important task in the future development of the method itself are to further exploit its potential by making it more accessible and yet more efficient.

Chapter 6

6 Summary and Outlook

In the scope of this thesis, I have explored new directions for stimuli-responsive hydrogel microstructures fabricated by 3D laser lithography. My main objective was to tackle the most pressing challenges in the field which hinder a further breakthrough of this promising approach to enable yet inaccessible applications. In this last chapter, I summarize the contents of this thesis and give a brief outlook on possible future developments.

In chapter 2, I have given a basic introduction into the topics which were covered in this work. The first section started with an overview of the 3D laser lithography technique with a special focus on the radical photopolymerization procedure as well as the two-photon absorption principle. Next, I have discussed the fabrication of stimuli-responsive hydrogel microstructures. I have compared two cases where the functional groups are either placed in the polymer backbone or in the crosslinks between polymer chains and explained the individual consequences. Furthermore, general challenges in the fabrication of hydrogels via 3D laser lithography were briefly summarized. In the last part of this fundamentals chapter, I have provided a basic introduction to mechanobiology which covered the actin cytoskeleton and class II myosin motors.

The methods which were used throughout the experiments in this thesis have been introduced in chapter 3. The first section covered all aspects regarding the fabrication of hydrogel microstructures via 3D laser lithography. I have explained the fabrication setup along with the sample preparation protocols and provided the necessary recipes for the photoresist compositions. Furthermore, I have described the single steps of the fabrication for the individual structures. In the following section, I have introduced the two methods AFM and LSM which have been extensively used for sample characterization and image acquisition. In this context, I have also presented the two sample holders which have been used in the experiments. Details

about the digital image cross-correlation, which played a crucial role for the tracking of beam displacements, have been summarized in the subsequent section. This methods chapter also included a basic description of the finite element calculations and their application in the two subsequently presented systems. In the last part, I have provided detailed information on the methodical aspects of the cell biological experiments, including cell types, culture conditions, and the protocols which were used for fixation and staining.

Chapter 4 comprised all results concerning thermo-responsive microstructures based on pNIPAM. I have started with a general discussion of the thermodynamic mechanism behind the LCST of NIPAM and its impact on polymerized hydrogel networks. The subsequent section summarized initial characterization results via AFM, which showed a strong change in volume as well as the mechanical properties around the LCST of 33 °C. One promising application was presented in the form of microfluidic valves, which enabled a reversible opening and closing of microchannels as a function of temperature. As a next step, I have discussed the gray-tone lithography approach to fabricate hetero-microstructures from a single resist. These bi-material beam structures exhibited strong, directed actuations upon stimulation and the responses were both robust in the fabrication and completely reversible over multiple cycles. I have also demonstrated basic applications microgrippers which were realized by combination of several bi-material structures. In the next part, I investigated more complex designs and the prediction of their responses via numerical calculations. The spatially controlled exposure dose of 3D laser lithography enabled the fabrication of structures with multiple alternating segments and complex bending behaviors. Furthermore, the implementation of a numerical approach in the spirit of reverse engineering enabled the estimation of these movements with a high accuracy. In contrast to all previous experiments, I was also able to demonstrate a light-induced stimulation. Two-photon absorption and subsequent photothermal conversion of focused laser light led to a localized response of the illuminated structures. Numerical calculations further revealed the timescales of this process and how heat dissipation in the surrounding water bath determines the response of adjacent structures. In the last part of this chapter, I have discussed these results and provided an outlook in future developments of this approach.

In the first part of chapter 5, I have presented stimuli-responsive 3D microscaffolds based on host-guest interactions for the mechanical stimulation of single cells. The first section introduced the mechanisms of the host-guest

complexes which led to a strong, reversible swelling of the hydrogel after addition of competitive guest molecules in solution. Next, this system was combined with several conventional materials to fabricate responsive composite scaffolds. These structures exhibited a well-defined and reversible response upon external stimulation with competitive guest molecules. In the subsequent section, I summarized the numerical calculations, which enabled a direct correlation between experimentally observed beam displacements and cellular forces.

The second part of chapter 5 covered the cell biological experiments which were performed with the introduced microscaffolds. First, I discussed the analysis of initial contraction forces which both, U2OS and NIH-3T3 cells, built up during invasion of the scaffolds. The next section summarized several results regarding the reaction of cells to mechanical stimulation. Cells have shown to exhibit a tensional homeostasis behavior, i.e., they actively pulled against the external stimulation. In this process, they increased their contraction forces and stabilized on a new dynamic setpoint. After releasing the stimulation, cells reduced their contraction forces again and the initial level was restored. In the next step, I highlighted that both, blocking of the ROCK pathway and using a NM2A-KO cell line led to a drastic decrease of the contraction force and the ability to react to the external stimulation. Furthermore, immunocytochemical stainings of the actin cytoskeleton presented in the subsequent section revealed the manifold emergence of new stress fibers upon stimulation. As expected from the previous experiments, this effect was no longer observed in NM2A-KO cells. Along this line, I presented results which show how an asymmetric stretch led to a localized response both in the force generation as well as emergence of new stress fibers. With fluorescent live cell imaging, I also introduced an additional approach to monitor these effects in the future. Finally, I concluded this chapter by discussing the results in the context of related work in literature and highlighted further possible directions for biological experiments as well as improvements of the method itself.

Outlook

With the two approaches presented within this thesis, I was able to overcome current challenges in the field of stimuli-responsive microstructures and enable previously inaccessible applications. Despite the basic similarity of the hydrogel structure, the two systems have various specific properties

like their stimuli and crosslinking mechanisms, which I have discussed in detail. In this context, it is crucial to choose the appropriate material based on its strengths and weaknesses for the particular application. Neither of the two materials in this thesis, for example, would have been able to fulfill the tasks in the respective other project. As discussed at the end of the individual chapters, further development of the methods could yet enhance their abilities to provide even more powerful toolkits.

One generally promising route for the future might be the incorporation of multiple stimuli in the same material. The chemistry community is already working hard to find new and interesting combinations of stimuli which can be conveniently used to provide new functions. In this context, the introduction of light as a stimulus is particularly intriguing because it enables both, remote control and spatial localization of the response. Here, one of the most important pending challenges related to applications in biology and biomedicine is the shift of the stimulation wavelength away from the ultraviolet regime, which is damaging to biological cells and tissue. Furthermore, unwanted side-effects due to an overlap with the fabrication wavelength can thus be avoided.

At the same time, research in the field of stimuli-responsive microstructures should not only be limited to hydrogels. They are often used in demonstrations because of the wide availability of materials and the vast changes in their material properties upon stimulation. However, while the restriction to aqueous environments is ideal for biological and biomedical applications, it is an exclusion criterion in almost all other cases. Thus, research on conceptually different material systems like liquid crystal elastomers or shape memory polymers could open the way to new applications like responsive metamaterials or 3D printed adaptive microoptics.

Future research, however, should also make a transition from pure materials design more towards applications. The adaptation of already available approaches with stimuli-responsive hydrogel microstructures could already contribute to solutions for a multitude of problems, e.g., in cell biology, microfluidics, or soft-robotics. Thus, it is equally important to promote the application of these methods to address current challenges in various research fields. As a consequence, this research area should make the transition away from a purely pushing technology which is only driven by new methodical improvements. One very important aspect in this context is the usability of the methods outside specialized laboratories. As discussed at various points throughout this thesis, the biological and biomedical fields have an enormous potential for the application of such systems. Sophisti-

cated fabrication techniques like 3D laser lithography, however, are typically not accessible in such working groups. For this reason, I am convinced that closer collaborations and an increased awareness of mutual problems between disciplines could evolve the potential of 3D stimuli-responsive hydrogel microstructures.

Appendix A

A Appendix

A.1 Cellular Response of NIH 3T3 Cells

We also investigated the impact of ROCK inhibition on the initial contraction forces of NIH 3T3 cells. In accordance to the procedure described in section 5.4, we waited for the cells to invade the scaffolds and reach an equilibrium state. Afterwards we started the image acquisition and released the cells by addition of trypsin. The differences in displacements thus yield the initial contraction forces built up by cells in the microscaffolds. The results are summarized in Figure A.1(a) in comparison to the data from U2OS cells. In the untreated condition, NIH 3T3 cells show larger contraction forces, as expected from literature and discussed in section 5.4. After addition of Y-27632, a drastic decrease of these forces can be observed in both cases.

In the next step, we wanted to clarify that the observed tensional homeostasis behavior described in section 5.5.1 is a general response and not special for the discussed U2OS cells. Therefore, we repeated the experiments in the stimuli-responsive microscaffolds with NIH 3T3 cells. We applied an equibiaxial stretch for 30 min and analyzed the change of contraction forces during this time period. The quantification is depicted Figure A.1(b) with a direct comparison to U2OS cells. Both cell types increase their contraction forces after the mechanical stimulation and stabilize on a new dynamic setpoint. The new level for NIH 3T3 cells is in a similar range from 70 to 80 nN compared to the U2OS cells.

It has to be noted that the scaffold design was initially optimized to the size of U2OS cells and has not been altered for these experiments. Since NIH 3T3 cells are slightly larger, they might not be able to spread to the fullest extent on the four beams of the scaffold. This could in turn lead to a small reduction in the measured traction forces.

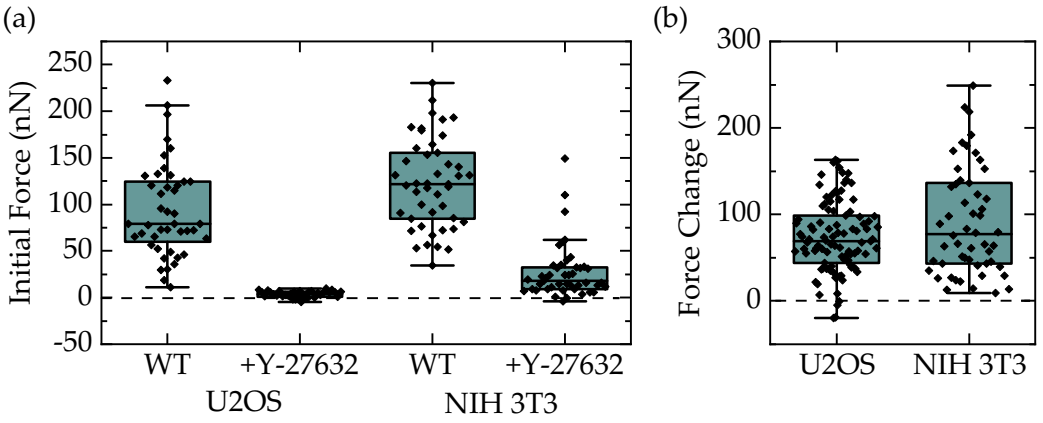

Figure A.1: Contraction forces of U2OS and NIH 3T3 cells. (a) Comparison of initial contraction forces of U2OS and NIH 3T3 cells with and without addition of the ROCK inhibitor Y-27632, respectively. (b) Change in contraction forces of U2OS and NIH 3T3 cells after 30 min of equibiaxial stretch in the stimuli-responsive microscaffolds. Each datapoint corresponds to one cell in a scaffold. Adapted from [34].

A.2 Role of NM2B in Generating Contraction Forces

As introduced in section 2.3.2, the three different non-muscle myosin II isoforms NM2A, NM2B, and NM2C are currently known in literature. In the main experiments of this thesis we focused on experiments with U2OS NM2A-KO cells because NM2A is known to play a crucial role in the maintenance of the actin cytoskeleton and generation of forces. We performed, however, additional experiments with U2OS NM2B-KO cells to study the impact of this isoform on the cellular response. Similar to the experiments presented in section 5.5.1, we performed an equibiaxial stretch and analyzed the change in contraction forces after 30 min.

Figure A.2 shows the quantified results in a comparison between the three investigated cell types. As discussed previously, knock-out of NM2A leads to a drastic decrease of the cellular response upon stimulation. This effect is less pronounced for the NM2B-KO cells, which still counteract the stimulation and stabilize on a new equilibrium level. The dynamic setpoint, however, is lower at around (43 ± 40) nN compared to the WT cells with a force change of (70 ± 41) nN. These experiments show that NM2B also plays an important role in the force generating machinery. Here, the interesting question arises why the NM2A-KO cells completely lose their

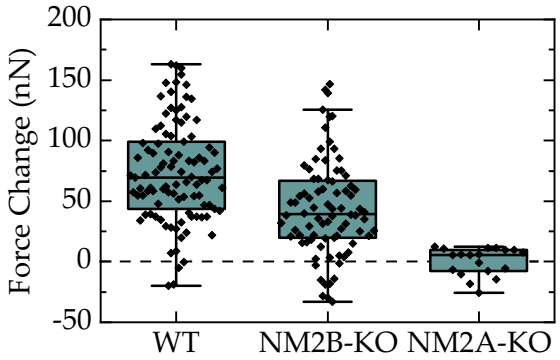

Figure A.2: Response of U2OS WT, NM2B-KO, and NM2A-KO cells to mechanical stimulation in the stimuli-responsive scaffolds. The change in contraction forces were analyzed after 30 min of equibiaxial stretching. Each datapoint corresponds to one cell in a scaffold.

ability to react to an external stimulation, even though NM2B is still present. More experiments investigating this aspect can hopefully shed light on the interaction between these two proteins. Furthermore, the role of NM2C in this whole process remains yet unclear.

A.3 Nanoindentation Experiments

As discussed in section 3.5.2, we performed numerical calculations to determine the relation between cellular forces and experimentally observed beam displacements. The necessary input parameters for the material properties were obtained by AFM nanoindentation (see section 3.2). Figure A.3 shows exemplary indentation experiments of PETA (a), TPETA (b), and the host-guest hydrogel (c). Subsequently, a Hertz fit was applied to these curves to obtain the Young's moduli which are quantified in panel (d) of the figure. For clarity, we only show the host-guest hydrogel in the stiff state without addition of competitive guest molecules in this overview. All measurements were performed in water to closely resemble the real experimental situation.

The resulting mean Young's moduli are $(3.0 \pm 1.6) \times 10^6$ kPa for PETA, $(12.7 \pm 1.2) \times 10^3$ kPa for TPETA, and (22.4 ± 1.8) kPa for the host-guest hydrogel. The comparatively large standard deviation for the PETA measurements is a consequence of the cantilever choice. The NanoWizard (JPK Instruments) AFM we used for our experiment is specialized on soft samples and is not suited to calibrate stiff cantilevers with the thermal noise method.

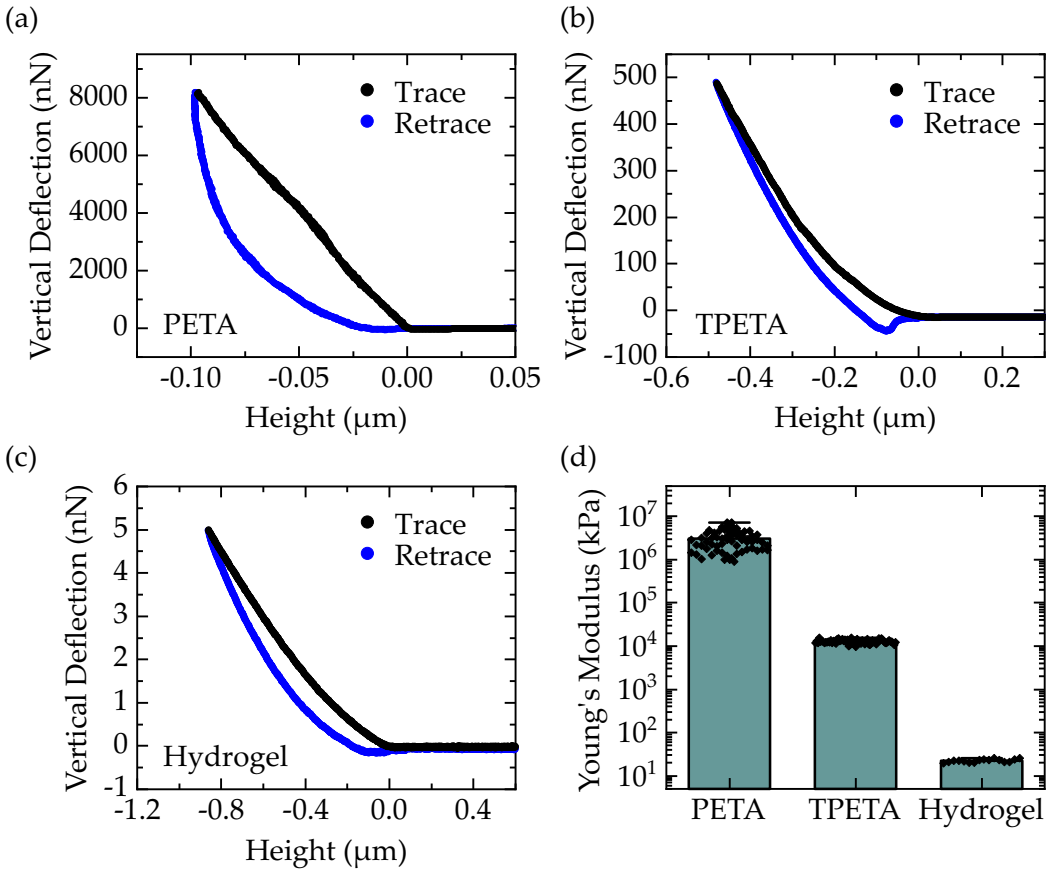

Figure A.3: Young's moduli of different used materials. (a-c) Exemplary indentation experiments for PETA, TPETA and the host-guest hydrogel (stiff state). (d) Quantification of the obtained Young's moduli. All measurements were performed in water. Adapted from [34].

To still be able to perform the calibration we had to use a softer cantilever with a lower resonance frequency. Thus the indentation depth in PETA is only small which leads to larger variations in the resulting fits. These errors, however, are not critical for the numerical calculations presented in section 3.5.2. Since the Young's modulus of PETA is in any case orders of magnitude higher compared to TPETA, the cellular forces only lead to a significant deflection of the TPETA walls and the PETA beams remain rigid.

Bibliography

[1] Alexander R. Todd, "Lord Todd: the state of chemistry", Chemical & Engineering News Archive **58**, 28–33 (1980) (cited on page 5).

[2] Y. Hu, Z. Wang, D. Jin, C. Zhang, R. Sun, Z. Li, K. Hu, J. Ni, Z. Cai, D. Pan, X. Wang, W. Zhu, J. Li, D. Wu, L. Zhang, and J. Chu, "Botanical-Inspired 4D Printing of Hydrogel at the Microscale", Advanced Functional Materials **30**, 1907377 (2020) (cited on page 5).

[3] P. M. Mendes, "Stimuli-responsive surfaces for bio-applications", Chemical Society Reviews **37**, 2512–2529 (2008) (cited on page 5).

[4] J. Hu, H. Meng, G. Li, and S. I. Ibekwe, "A review of stimuli-responsive polymers for smart textile applications", Smart Materials and Structures **21**, 053001 (2012) (cited on page 5).

[5] S. Mura, J. Nicolas, and P. Couvreur, "Stimuli-responsive nanocarriers for drug delivery", Nature Materials **12**, 991–1003 (2013) (cited on page 5).

[6] L. Dong, A. K. Agarwal, D. J. Beebe, and H. Jiang, "Adaptive liquid microlenses activated by stimuli-responsive hydrogels", Nature **442**, 551–554 (2006) (cited on page 6).

[7] K. R. Ryan, M. P. Down, and C. E. Banks, "Future of Additive Manufacturing: Overview of 4D and 3D Printed Smart and Advanced Materials and their Applications", Chemical Engineering Journal, 126162 (2021) (cited on page 6).

[8] X. Le, W. Lu, J. Zhang, and T. Chen, "Recent Progress in Biomimetic Anisotropic Hydrogel Actuators", Advanced Science **44**, 1801584 (2019) (cited on page 6).

[9] H. Zeng, P. Wasylczyk, D. S. Wiersma, and A. Priimagi, "Light Robots: Bridging the Gap between Microrobotics and Photomechanics in Soft Materials", Advanced Materials **30**, e1703554 (2018) (cited on page 6).

[10] C. A. Spiegel, M. Hippler, A. Münchinger, M. Bastmeyer, C. Barner-Kowollik, M. Wegener, and E. Blasco, "4D Printing at the Microscale", Advanced Functional Materials, 1907615 (2019) (cited on pages 6, 56).

[11] T. Watanabe, M. Akiyama, K. Totani, S. M. Kuebler, F. Stellacci, W. Wenseleers, K. Braun, S. R. Marder, and J. W. Perry, "Photoresponsive Hydrogel Microstructure Fabricated by Two-Photon Initiated Polymerization", Advanced Functional Materials **12**, 611–614 (2002) (cited on page 6).

[12] Z. Xiong, M.-L. Zheng, X.-Z. Dong, W.-Q. Chen, F. Jin, Z.-S. Zhao, and X.-M. Duan, "Asymmetric microstructure of hydrogel: two-photon microfabrication and stimuli-responsive behavior", Soft Matter **7**, 10353 (2011) (cited on page 6).

[13] L. D. Zarzar, P. Kim, M. Kolle, C. J. Brinker, J. Aizenberg, and B. Kaehr, "Direct Writing and Actuation of Three-Dimensionally Patterned Hydrogel Pads on Micropillar Supports", Angewandte Chemie International Edition **50**, 9356–9360 (2011) (cited on pages 6, 56).

[14] A. Ovsianikov, J. Stampfl, and R. Liska, eds., *Multiphoton Lithography: Techniques, materials and applications* (John Wiley & Sons, 2016) (cited on page 9).

[15] J. Fischer and M. Wegener, "Three-dimensional optical laser lithography beyond the diffraction limit", Laser & Photonics Reviews **7**, 22–44 (2013) (cited on pages 9, 12, 14, 16, 17).

[16] T. Baldacchini, *Three-Dimensional Microfabrication Using Two-photon Polymerization* (Elsevier, 2016) (cited on page 10).

[17] L. Yang, A. Münchinger, M. Kadic, V. Hahn, F. Mayer, E. Blasco, C. Barner-Kowollik, and M. Wegener, "On the Schwarzschild Effect in 3D Two-Photon Laser Lithography", Advanced Optical Materials **7**, 1901040 (2019) (cited on pages 12, 15).

[18] J. B. Mueller, J. Fischer, F. Mayer, M. Kadic, and M. Wegener, "Polymerization Kinetics in Three-Dimensional Direct Laser Writing", Advanced Materials **26**, 6566–6571 (2014) (cited on page 12).

[19] P. Kiefer, V. Hahn, M. Nardi, L. Yang, E. Blasco, C. Barner-Kowollik, and M. Wegener, "Sensitive Photoresists for Rapid Multiphoton 3D Laser Micro- and Nanoprinting", Advanced Optical Materials, 2000895 (2020) (cited on pages 12, 14).

[20] P. Alexander and B. Nikihita, "Modeling of Polymerization Processes", in *Multiphoton Lithography*, edited by A. Ovsianikov, J. Stampfl, and R. Liska (John Wiley & Sons, 2016), pp. 65–93 (cited on page 12).

[21] B. E. A. Saleh and M. C. Teich, *Fundamentals of Photonics*, Third edition, Wiley Series in Pure and Applied Optics (John Wiley & Sons, 2019) (cited on page 14).

[22] J. K. Hohmann, M. Renner, E. H. Waller, and G. von Freymann, "Three-Dimensional μ-Printing: An Enabling Technology", Advanced Optical Materials **3**, 1488–1507 (2015) (cited on page 15).

[23] A. V. Pikulin and N. M. Bityurin, "Fluctuation Limitations on the Voxel Minimal Size at Laser Nanopolymerization", Technical Physics **57**, 697–705 (2012) (cited on page 15).

[24] A. Wickberg, A. Abass, H.-H. Hsiao, C. Rockstuhl, and M. Wegener, "Second-Harmonic Generation by 3D Laminate Metacrystals", Advanced Optical Materials **7**, 1801235 (2019) (cited on page 15).

[25] E. Abbe, "Beiträge zur Theorie des Mikroskops und der mikroskopischen Wahrnehmung", Archiv für Mikroskopische Anatomie **9**, 413–468 (1873) (cited on page 16).

[26] C. M. Sparrow, "On Spectroscopic Resolving Power", Astrophysical Journal **44**, 76 (1916) (cited on page 16).

[27] Z. Li, J. Torgersen, A. Ajami, S. Mühleder, X. Qin, W. Husinsky, W. Holnthoner, A. Ovsianikov, J. Stampfl, and R. Liska, "Initiation efficiency and cytotoxicity of novel watersoluble two-photon photoinitiators for direct 3D microfabrication of hydrogels", RSC Advances **3**, 15939 (2013) (cited on pages 18, 60).

[28] X. Huang, X. Wang, and Y. Zhao, "Study on a series of water-soluble photoinitiators for fabrication of 3D hydrogels by two-photon polymerization", Dyes and Pigments **141**, 413–419 (2017) (cited on page 18).

[29] W. Tomal and J. Ortyl, "Water-Soluble Photoinitiators in Biomedical Applications", Polymers **12**, 1073 (2020) (cited on page 18).

[30] B. D. Fairbanks, M. P. Schwartz, C. N. Bowman, and K. S. Anseth, "Photoinitiated polymerization of PEG-diacrylate with lithium phenyl-2,4,6trimethylbenzoylphosphinate: polymerization rate and cytocompatibility", Biomaterials **30**, 6702–6707 (2009) (cited on pages 18, 60, 84).

[31] D. E. Fast, A. Lauer, J. P. Menzel, A.-M. Kelterer, G. Gescheidt, and C. Barner-Kowollik, "Wavelength-Dependent Photochemistry of Oxime Ester Photoinitiators", Macromolecules **50**, 1815–1823 (2017) (cited on page 18).

[32] E. Frick, C. Schweigert, B. B. Noble, H. A. Ernst, A. Lauer, Y. Liang, D. Voll, M. L. Coote, A.-N. Unterreiner, and C. Barner-Kowollik, "Toward a Quantitative Description of Radical Photoinitiator Structure–Reactivity Correlations", Macromolecules **49**, 80–89 (2016) (cited on page 18).

[33] M. Hippler, E. Blasco, J. Qu, M. Tanaka, C. Barner-Kowollik, M. Wegener, and M. Bastmeyer, "Controlling the shape of 3D microstructures by temperature and light", Nature Communications **10**, 232 (2019) (cited on pages 18, 61, 64, 66, 67, 69–71, 73, 75, 77, 78).

[34] M. Hippler, K. Weißenbruch, K. Richler, E. D. Lemma, M. Nakahata, B. Richter, C. Barner-Kowollik, Y. Takashima, A. Harada, E. Blasco, M. Wegener, M. Tanaka, and M. Bastmeyer, "Mechanical stimulation of single cells by reversible host-guest interactions in 3D microscaffolds", Science Advances **6**, eabc2648 (2020) (cited on pages 18, 84, 86, 87, 89, 91–96, 99, 101, 103–109, 111–114, 128, 130).

[35] W. Zhang, P. Soman, K. Meggs, X. Qu, and S. Chen, "Tuning the Poisson's Ratio of Biomaterials for Investigating Cellular Response", Advanced Functional Materials **23**, 3226–3232 (2013) (cited on page 18).

[36] O. A. Banda, C. R. Sabanayagam, and J. H. Slater, "Reference-Free Traction Force Microscopy Platform Fabricated via Two-Photon Laser Scanning Lithography Enables Facile Measurement of Cell-Generated Forces", ACS Applied Materials & Interfaces **11**, 18233–18241 (2019) (cited on page 18).

[37] E. D. Lemma, F. Rizzi, T. Dattoma, B. Spagnolo, L. Sileo, A. Qualtieri, M. de Vittorio, and F. Pisanello, "Mechanical properties tunability of threedimensional polymeric structures in two-photon lithography", IEEE Transactions on Nanotechnology, 1 (2016) (cited on page 19).

[38] C.-S. Shin, T.-J. Li, and C.-L. Lin, "Alleviating Distortion and Improving the Young's Modulus in Two-Photon Polymerization Fabrications", Micromachines **9**, 615 (2018) (cited on page 19).

[39] J. Qu, M. Kadic, A. Naber, and M. Wegener, "Micro-Structured Two-Component 3D Metamaterials with Negative Thermal-Expansion Coefficient from Positive Constituents", Scientific Reports **7**, 40643 (2017) (cited on pages 20, 42, 65).

[40] H.-B. Sun, T. Suwa, K. Takada, R. P. Zaccaria, M.-S. Kim, K.-S. Lee, and S. Kawata, "Shape precompensation in two-photon laser nanowriting of photonic lattices", Applied Physics Letters **85**, 3708–3710 (2004) (cited on page 22).

[41] T. Bückmann, N. Stenger, M. Kadic, J. Kaschke, A. Frölich, T. Kennerknecht, C. Eberl, M. Thiel, and M. Wegener, "Tailored 3D mechanical metamaterials made by dip-in direct-laser-writing optical lithography", Advanced Materials **24**, 2710–2714 (2012) (cited on pages 23, 33, 42).

[42] Kai Weißenbruch, *Adaption der Zellmorphologie durch Aktomyosin-Kontraktilität auf mikrostrukturierten Zellkultursubstraten* (2019) (cited on pages 23, 27, 29, 51, 52).

[43] V. Vogel and M. Sheetz, "Local force and geometry sensing regulate cell functions", Nature Reviews Molecular Cell Biology **7**, 265–275 (2006) (cited on page 23).

[44] L. Blanchoin, R. Boujemaa-Paterski, C. Sykes, and J. Plastino, "Actin Dynamics, Architecture, and Mechanics in Cell Motility", Physiological Reviews **94**, 235–263 (2014) (cited on page 23).

[45] B. M. Baker and C. S. Chen, "Deconstructing the third dimension – how 3D culture microenvironments alter cellular cues", Journal of Cell Science **125**, 3015–3024 (2012) (cited on pages 25, 81).

[46] M. Vicente-Manzanares, X. Ma, R. S. Adelstein, and A. R. Horwitz, "Non-muscle myosin II takes centre stage in cell adhesion and migration", Nature Reviews Molecular Cell Biology **10**, 778–790 (2009) (cited on pages 25, 107).

[47] B. Geiger, J. P. Spatz, and A. D. Bershadsky, "Environmental sensing through focal adhesions", Nature Reviews Molecular Cell Biology **10**, 21–33 (2009) (cited on page 25).

[48] E. Papusheva and C.-P. Heisenberg, "Spatial organization of adhesion: force-dependent regulation and function in tissue morphogenesis", The EMBO Journal **29**, 2753–2768 (2010) (cited on page 25).

[49] Q. Wen and P. A. Janmey, "Polymer physics of the cytoskeleton", Current Opinion in Solid State and Materials Science **15**, 177–182 (2011) (cited on page 25).

[50] M. Murrell, P. W. Oakes, M. Lenz, and M. L. Gardel, "Forcing cells into shape: the mechanics of actomyosin contractility", Nature Reviews Molecular Cell Biology **16**, 486–498 (2015) (cited on pages 25, 26).

[51] T. Svitkina, "The Actin Cytoskeleton and Actin-Based Motility", Cold Spring Harbor Perspectives in Biology **10**, a018267 (2018) (cited on page 25).

[52] C. G. Dos Remedios, D. Chhabra, M. Kekic, I. V. Dedova, M. Tsubakihara, D. A. Berry, and N. J. Nosworthy, "Actin binding proteins: regulation of cytoskeletal microfilaments", Physiological Reviews **83**, 433–473 (2003) (cited on page 26).

[53] L. P. Cramer, M. Siebert, and T. J. Mitchison, "Identification of novel graded polarity actin filament bundles in locomoting heart fibroblasts: implications for the generation of motile force", Journal of Cell Biology **136**, 1287–1305 (1997) (cited on page 26).

[54] S. Pellegrin and H. Mellor, "Actin stress fibres", Journal of Cell Science **120**, 3491–3499 (2007) (cited on page 26).

[55] M. Prager-Khoutorsky, A. Lichtenstein, R. Krishnan, K. Rajendran, A. Mayo, Z. Kam, B. Geiger, and A. D. Bershadsky, "Fibroblast polarization is a matrix-rigidity-dependent process controlled by focal adhesion mechanosensing", Nature Cell Biology **13**, 1457–1465 (2011) (cited on page 26).

[56] N. Sandbo and N. Dulin, "Actin cytoskeleton in myofibroblast differentiation: Ultrastructure defining form and driving function", Translational Research **158**, 181–196 (2011) (cited on page 26).

[57] E. Tzima, M. Irani-Tehrani, W. B. Kiosses, E. Dejana, D. A. Schultz, B. Engelhardt, G. Cao, H. DeLisser, and M. A. Schwartz, "A mechanosensory complex that mediates the endothelial cell response to fluid shear stress", Nature **437**, 426–431 (2005) (cited on page 26).

[58] A. J. Wong, T. D. Pollard, and I. M. Herman, "Actin Filament Stress Fibers in Vascular Endothelial Cells in Vivo", Science **219**, 867–869 (1983) (cited on page 26).

[59] J. R. Sellers, "Myosins: a diverse superfamily", Biochimica et Biophysica Acta - Molecular Cell Research **1496**, 3–22 (2000) (cited on page 27).

[60] T. Hasson, "Myosin VI: two distinct roles in endocytosis", Journal of Cell Science **116**, 3453–3461 (2003) (cited on page 27).

[61] J. A. Hammer and J. R. Sellers, "Walking to work: roles for class V myosins as cargo transporters", Nature Reviews Molecular Cell Biology **13**, 13–26 (2011) (cited on page 27).

[62] M. T. Breckenridge, N. G. Dulyaninova, and T. T. Egelhoff, "Multiple regulatory steps control mammalian nonmuscle myosin II assembly in live cells", Molecular Biology of the Cell **20**, 338–347 (2009) (cited on page 27).

[63] R. H. Fitts, "The cross-bridge cycle and skeletal muscle fatigue", Journal of Applied Physiology **104**, 551–558 (2008) (cited on page 27).

[64] A. B. Verkhovsky and G. G. Borisy, "Non-sarcomeric mode of myosin II organization in the fibroblast lamellum", Journal of Cell Biology **123**, 637–652 (1993) (cited on page 28).

[65] N. Billington, A. Wang, J. Mao, R. S. Adelstein, and J. R. Sellers, "Characterization of three full-length human nonmuscle myosin II paralogs", Journal of Biological Chemistry **288**, 33398–33410 (2013) (cited on page 28).

[66] L. Haviv, D. Gillo, F. Backouche, and A. Bernheim-Groswasser, "A Cytoskeletal Demolition Worker: Myosin II Acts as an Actin Depolymerization Agent", Journal of Molecular Biology **375**, 325–330 (2008) (cited on page 28).

[67] J. R. Beach, G. S. Hussey, T. E. Miller, A. Chaudhury, P. Patel, J. Monslow, Q. Zheng, R. A. Keri, O. Reizes, A. R. Bresnick, P. H. Howe, and T. T. Egelhoff, "Myosin II isoform switching mediates invasiveness after TGF-β-induced epithelial-mesenchymal transition", Proceedings of the National Academy of Sciences **108**, 17991–17996 (2011) (cited on page 28).

[68] M. Kovács, F. Wang, A. Hu, Y. Zhang, and J. R. Sellers, "Functional Divergence of Human Cytoplasmic Myosin II", Journal of Biological Chemistry **278**, 38132–38140 (2003) (cited on page 28).

[69] F. Wang, M. Kovács, A. Hu, J. Limouze, E. V. Harvey, and J. R. Sellers, "Kinetic Mechanism of Non-muscle Myosin IIB", Journal of Biological Chemistry **278**, 27439–27448 (2003) (cited on page 28).

[70] O. Milberg, A. Shitara, S. Ebrahim, A. Masedunskas, M. Tora, D. T. Tran, Y. Chen, M. A. Conti, R. S. Adelstein, K. G. ten Hagen, and R. Weigert, "Concerted actions of distinct nonmuscle myosin II isoforms drive intracellular membrane remodeling in live animals", Journal of Cell Biology **216**, 1925–1936 (2017) (cited on page 28).

[71] E. Golomb, X. Ma, S. S. Jana, Y. A. Preston, S. Kawamoto, N. G. Shoham, E. Goldin, M. A. Conti, J. R. Sellers, and R. S. Adelstein, "Identification and Characterization of Nonmuscle Myosin II-C, a New Member of the Myosin II Family", Journal of Biological Chemistry **279**, 2800–2808 (2004) (cited on page 28).

[72] S. Even-Ram, A. D. Doyle, M. A. Conti, K. Matsumoto, R. S. Adelstein, and K. M. Yamada, "Myosin IIA regulates cell motility and actomyosin– microtubule crosstalk", Nature Cell Biology **9**, 299–309 (2007) (cited on page 29).

[73] Y. Cai, N. Biais, G. Giannone, M. Tanase, G. Jiang, J. M. Hofman, C. H. Wiggins, P. Silberzan, A. Buguin, B. Ladoux, and M. P. Sheetz, "Nonmuscle Myosin IIA-Dependent Force Inhibits Cell Spreading and Drives F-Actin Flow", Biophysical Journal **91**, 3907–3920 (2006) (cited on page 29).

[74] D. G. Thomas, A. Yenepalli, C. M. Denais, A. Rape, J. R. Beach, Y.-l. Wang, W. P. Schiemann, H. Baskaran, J. Lammerding, and T. T. Egelhoff, "Non-muscle myosin IIB is critical for nuclear translocation during 3D invasion", Journal of Cell Biology **210**, 583–594 (2015) (cited on page 29).

[75] K. Terpilowski and D. Rymuszka, "Surface Properties of Glass Plates Activated by Air, Oxygen, Nitrogen and Argon Plasma", Glass Physics and Chemistry **42**, 535–541 (2016) (cited on page 34).

[76] A. Harada, R. Kobayashi, Y. Takashima, A. Hashidzume, and H. Yamaguchi, "Macroscopic self-assembly through molecular recognition", Nature Chemistry **3**, 34–37 (2011) (cited on pages 35, 83).

[77] J. L. Hutter and J. Bechhoefer, "Calibration of atomic-force microscope tips", Review of Scientific Instruments **64**, 1868–1873 (1993) (cited on page 40).

[78] B. Pan, K. Qian, H. Xie, and A. Asundi, "Two-dimensional digital image correlation for in-plane displacement and strain measurement: a review", Measurement science & technology **20**, 062001 (2009) (cited on pages 42, 45, 90).

[79] E. Christoph, *Digital Image Correlation and Tracking: MATLAB Central File Exchange*, 2020 (cited on page 42).

[80] J. N. Reddy, *An Introduction to the Finite Element Method*, Third Edition (2005) (cited on page 47).

[81] J. R. Beach, L. Shao, K. Remmert, D. Li, E. Betzig, and J. A. Hammer, "Nonmuscle Myosin II Isoforms Coassemble in Living Cells", Current Biology **24**, 1160–1166 (2014) (cited on page 51).

[82] P. Hotulainen and P. Lappalainen, "Stress fibers are generated by two distinct actin assembly mechanisms in motile cells", Journal of Cell Biology **173**, 383–394 (2006) (cited on page 51).

[83] Kathrin Stricker, *Erzeugung und Charakterisierung einer Nichtmuskulären Myosin IIB Knockout Zelllinie Mittels CRISPR/Cas9* (2017) (cited on pages 51, 52).

[84] Y.-Z. You, K. K. Kalebaila, S. L. Brock, and D. Oupický, "Temperature-Controlled Uptake and Release in PNIPAM-Modified Porous Silica Nanoparticles", Chemistry of Materials **20**, 3354–3359 (2008) (cited on pages 55, 79).

[85] G. Huang, J. Gao, Z. Hu, J. V. St John, B. C. Ponder, and D. Moro, "Controlled drug release from hydrogel nanoparticle networks", Journal of Controlled Release **94**, 303–311 (2004) (cited on pages 55, 79).

[86] S. Schmidt, M. Zeiser, T. Hellweg, C. Duschl, A. Fery, and H. Möhwald, "Adhesion and Mechanical Properties of PNIPAM Microgel Films and Their Potential Use as Switchable Cell Culture Substrates", Advanced Functional Materials **20**, 3235–3243 (2010) (cited on page 55).

[87] W. J. Zheng, N. An, J. H. Yang, J. Zhou, and Y. M. Chen, "Tough Al-alginate/Poly(N-isopropylacrylamide) Hydrogel with Tunable LCST for Soft Robotics", ACS Applied Materials & Interfaces **7**, 1758–1764 (2015) (cited on page 55).

[88] K. Nagase, M. Yamato, H. Kanazawa, and T. Okano, "Poly(N-isopropylacrylamide)-based thermoresponsive surfaces provide new types of biomedical applications", Biomaterials **153**, 27–48 (2017) (cited on page 55).

[89] Y. Guan and Y. Zhang, "PNIPAM microgels for biomedical applications: from dispersed particles to 3D assemblies", Soft Matter **7**, 6375 (2011) (cited on pages 55, 56).

[90] A. Ghosh, C. Yoon, F. Ongaro, S. Scheggi, F. M. Selaru, S. Misra, and D. H. Gracias, "Stimuli-Responsive Soft Untethered Grippers for Drug Delivery and Robotic Surgery", Frontiers in Mechanical Engineering **3**, 7 (2017) (cited on page 55).

[91] S. Schmidt, H. Motschmann, T. Hellweg, and R. von Klitzing, "Thermoresponsive surfaces by spin-coating of PNIPAM-co-PAA microgels: A combined AFM and ellipsometry study", Polymer **49**, 749–756 (2008) (cited on page 55).

[92] L.-Y. Chu, T. Niitsuma, T. Yamaguchi, and S. Nakao, "Thermoresponsive Transport through Porous Membranes with Grafted PNIPAM Gates", AIChE Journal **49**, 896–909 (2003) (cited on page 55).

[93] H. N. Kim, D.-H. Kang, M. S. Kim, A. Jiao, D.-H. Kim, and K.-Y. Suh, "Patterning Methods for Polymers in Cell and Tissue Engineering", Annals of Biomedical Engineering **40**, 1339–1355 (2012) (cited on page 55).

[94] Y. Tsuda, A. Kikuchi, M. Yamato, A. Nakao, Y. Sakurai, M. Umezu, and T. Okano, "The use of patterned dual thermoresponsive surfaces for the collective recovery as co-cultured cell sheets", Biomaterials **26**, 1885–1893 (2005) (cited on page 55).

[95] J. C. Breger, C. Yoon, R. Xiao, H. R. Kwag, M. O. Wang, J. P. Fisher, T. D. Nguyen, and D. H. Gracias, "Self-Folding Thermo-Magnetically Responsive Soft Microgripper", ACS Applied Materials & Interfaces **7**, 3398–3405 (2015) (cited on page 55).

[96] D. Han, Z. Lu, S. A. Chester, and H. Lee, "Micro 3D Printing of a Temperature-Responsive Hydrogel Using Projection Micro-Stereolithography", Scientific Reports **8**, 1963 (2018) (cited on page 55).

[97] A. Nishiguchi, A. Mourran, H. Zhang, and M. Möller, "In-Gel Direct Laser Writing for 3D-Designed Hydrogel Composites That Undergo Complex Self-Shaping", Advanced Science **2**, 1700038 (2017) (cited on page 56).

[98] H. G. Schild, "Poly(N-Isopropylacrylamide): Experiment, Theory and Application", Progress in Polymer Science **17**, 163–249 (1992) (cited on pages 56–58).

[99] J. S. Scarpa, D. D. Mueller, and I. M. Klotz, "Slow Hydrogen-Deuterium Exchange in a Non-α-helical Polyamide", Journal of the American Chemical Society **89**, 6024–6030 (1967) (cited on page 56).

[100] M. Heskins and J. E. Guillet, "Solution Properties of Poly(N-Isopropylacrylamide)", Journal of Macromolecular Science: Part A - Chemistry **2**, 1441–1455 (1968) (cited on page 56).

[101] Y. Hirokawa and T. Tanaka, "Volume phase transition in a nonionic gel", AIP Conference Proceedings **107**, 203–208 (1984) (cited on page 56).

[102] J. S. Walker and C. A. Vause, "Reappearing Phases", Scientific American **256**, 98–105 (1987) (cited on page 57).

[103] H. B. Callen, *Thermodynamics and an Introduction to Thermostatistics, 2nd Edition* (Wiley, 1985) (cited on page 57).

[104] X. Wang, X. Qiu, and C. Wu, "Comparison of the Coil-to-Globule and the Globule-to-Coil Transitions of a Single Poly(N-isopropylacrylamide) Homopolymer Chain in Water", Macromolecules **31**, 2972–2976 (1998) (cited on page 57).

[105] D. Mukherji and K. Kremer, "Coil–Globule–Coil Transition of PNIPAm in Aqueous Methanol: Coupling All-Atom Simulations to Semi-Grand Canonical Coarse-Grained Reservoir", Macromolecules **46**, 9158–9163 (2013) (cited on page 57).

[106] L.-C. Dong and A. S. Hoffman, "Synthesis and application of thermally reversible heterogels for drug delivery", Journal of Controlled Release **13**, 21–31 (1990) (cited on page 58).

[107] R. Pelton, "Poly(N-isopropylacrylamide) (PNIPAM) is never hydrophobic", Journal of Colloid and Interface Science **348**, 673–674 (2010) (cited on page 58).

[108] I. Varga, T. Gilányi, R. Mészáros, G. Filipcsei, and M. Zrínyi, "Effect of Cross-Link Density on the Internal Structure of Poly(N-isopropylacrylamide) Microgels", The Journal of Physical Chemistry B **105**, 9071–9076 (2001) (cited on pages 60, 62).

[109] A. Burmistrova, M. Richter, C. Uzum, and R. v. Klitzing, "Effect of cross-linker density of P(NIPAM-co-AAc) microgels at solid surfaces on the swelling/shrinking behaviour and the Young's modulus", Colloid and Polymer Science **289**, 613–624 (2011) (cited on pages 60, 62).

[110] K. J. Schafer, J. M. Hales, M. Balu, K. D. Belfield, E. W. van Stryland, and D. J. Hagan, "Two-photon absorption cross-sections of common photoinitiators", Journal of Photochemistry and Photobiology A: Chemistry **162**, 497–502 (2004) (cited on page 60).

[111] A. Ovsianikov, V. Mironov, J. Stampf, and R. Liska, "Engineering 3D cell-culture matrices: multiphoton processing technologies for biological & tissue engineering applications", Expert Review of Medical Devices **9**, 613–633 (2012) (cited on page 60).

[112] M. Soreni-Harari, R. St Pierre, C. McCue, K. Moreno, and S. Bergbreiter, "Multimaterial 3D Printing for Microrobotic Mechanisms", Soft Robotics **7**, 59–67 (2020) (cited on page 63).

[113] D. Gräfe, A. Wickberg, M. M. Zieger, M. Wegener, E. Blasco, and C. Barner-Kowollik, "Adding chemically selective subtraction to multimaterial 3D additive manufacturing", Nature Communications **9**, 2788 (2018) (cited on page 63).

[114] A. C. Lamont, M. A. Restaino, M. J. Kim, and R. D. Sochol, "A facile multi-material direct laser writing strategy", Lab on a Chip **19**, 2340–2345 (2019) (cited on page 63).

[115] M. A. Haq, Y. Su, and D. Wang, "Mechanical properties of PNIPAM based hydrogels: A review", Materials Science and Engineering: C **70**, 842–855 (2017) (cited on page 63).

[116] F. Mayer, S. Richter, J. Westhauser, E. Blasco, C. Barner-Kowollik, and M. Wegener, "Multimaterial 3D laser microprinting using an integrated microfluidic system", Science Advances **5**, eaau9160 (2019) (cited on pages 64, 118).

[117] S. Timoshenko, "Analysis of Bi-Metal Thermostats", Journal of the Optical Society of America **11**, 233 (1925) (cited on pages 65, 69).

[118] D. Trivedi, C. D. Rahn, W. M. Kier, and I. D. Walker, "Soft robotics: Biological inspiration, state of the art, and future research", Applied Bionics and Biomechanics **5**, 99–117 (2008) (cited on page 70).

[119] H. K. Yap, H. Y. Ng, and C.-H. Yeow, "High-Force Soft Printable Pneumatics for Soft Robotic Applications", Soft Robotics **3**, 144–158 (2016) (cited on page 70).

[120] J. Abdolahi, M. Baghani, N. Arbabi, and H. Mazaheri, "Analytical and numerical analysis of swelling-induced large bending of thermally-activated hydrogel bilayers", International Journal of Solids and Structures **99**, 1–11 (2016) (cited on page 72).

[121] T. Morimoto and F. Ashida, "Temperature-responsive bending of a bilayer gel", International Journal of Solids and Structures **56-57**, 20–28 (2015) (cited on page 72).

[122] X. Huang, I. H. El-Sayed, W. Qian, and M. A. El-Sayed, "Cancer Cell Imaging and Photothermal Therapy in the Near-Infrared Region by Using Gold Nanorods", Journal of the American Chemical Society **128**, 2115–2120 (2006) (cited on page 74).

[123] M. S. Yavuz, Y. Cheng, J. Chen, C. M. Cobley, Q. Zhang, M. Rycenga, J. Xie, C. Kim, K. H. Song, A. G. Schwartz, L. V. Wang, and Y. Xia, "Gold nanocages covered by smart polymers for controlled release with near-infrared light", Nature Materials **8**, 935–939 (2009) (cited on page 74).

[124] P. Mueller, M. Thiel, and M. Wegener, "3D direct laser writing using a 405 nm diode laser", Optics Letters **39**, 6847–6850 (2014) (cited on page 76).

[125] S. Glatzel, A. Laschewsky, and J.-F. Lutz, "Well-Defined Uncharged Polymers with a Sharp UCST in Water and in Physiological Milieu", Macromolecules **44**, 413–415 (2011) (cited on page 79).

[126] J. Seuring and S. Agarwal, "Polymers with Upper Critical Solution Temperature in Aqueous Solution", Macromolecular Rapid Communications **33**, 1898–1920 (2012) (cited on page 79).

[127] Y. Kotsuchibashi, "Recent advances in multi-temperature-responsive polymeric materials", Polymer Journal **52**, 681–689 (2020) (cited on page 79).

[128] E. Blasco, J. Müller, P. Müller, V. Trouillet, M. Schön, T. Scherer, C. Barner-Kowollik, and M. Wegener, "Fabrication of Conductive 3D Gold-Containing Microstructures via Direct Laser Writing", Advanced Materials **28**, 3592–3595 (2016) (cited on page 79).

[129] X.-M. Duan, H.-B. Sun, K. Kaneko, and S. Kawata, "Two-photon polymerization of metal ions doped acrylate monomers and oligomers for three-dimensional structure fabrication", Thin Solid Films **453-454**, 518–521 (2004) (cited on page 79).

[130] T. Kawano, Y. Niidome, T. Mori, Y. Katayama, and T. Niidome, "PNIPAM Gel-Coated Gold Nanorods for Targeted Delivery Responding to a Near-Infrared Laser", Bioconjugate Chemistry **20**, 209–212 (2009) (cited on page 79).

[131] A. Sutton, T. Shirman, J. V. I. Timonen, G. T. England, P. Kim, M. Kolle, T. Ferrante, L. D. Zarzar, E. Strong, and J. Aizenberg, "Photothermally triggered actuation of hybrid materials as a new platform for in vitro cell manipulation", Nature Communications **8**, 14700 (2017) (cited on page 79).

[132] M. Hippler, E. D. Lemma, S. Bertels, E. Blasco, C. Barner-Kowollik, M. Wegener, and M. Bastmeyer, "3D Scaffolds to Study Basic Cell Biology", Advanced Materials **31**, 1808110 (2019) (cited on pages 80, 82).

[133] L. Trichet, J. Le Digabel, R. J. Hawkins, S. R. K. Vedula, M. Gupta, C. Ribrault, P. Hersen, R. Voituriez, and B. Ladoux, "Evidence of a large-scale mechanosensing mechanism for cellular adaptation to substrate stiffness", Proceedings of the National Academy of Sciences **109**, 6933–6938 (2012) (cited on pages 81, 98).

[134] V. Ruprecht, P. Monzo, A. Ravasio, Z. Yue, E. Makhija, P. O. Strale, N. Gauthier, G. V. Shivashankar, V. Studer, C. Albiges-Rizo, and V. Viasnoff, "How cells respond to environmental cues – insights from bio-functionalized substrates", Journal of Cell Science **130**, 51–61 (2017) (cited on page 81).

[135] B. D. Matthews, D. R. Overby, R. Mannix, and D. E. Ingber, "Cellular adaptation to mechanical stress: role of integrins, Rho, cytoskeletal tension and mechanosensitive ion channels", Journal of Cell Science **119**, 508–518 (2006) (cited on page 81).

[136] S. Dupont, L. Morsut, M. Aragona, E. Enzo, S. Giulitti, M. Cordenonsi, F. Zanconato, J. Le Digabel, M. Forcato, S. Bicciato, N. Elvassore, and S. Piccolo, "Role of YAP/TAZ inmechanotransduction", Nature **474**, 179–183 (2011) (cited on page 81).

[137] Y. Kamotani, T. Bersano-Begey, N. Kato, Y.-C. Tung, D. Huh, J. W. Song, and S. Takayama, "Individually programmable cell stretching microwell arrays actuated by a Braille display", Biomaterials **29**, 2646–2655 (2008) (cited on page 81).

[138] D. Tremblay, S. Chagnon-Lessard, M. Mirzaei, A. E. Pelling, and M. Godin, "A microscale anisotropic biaxial cell stretching device for applications in mechanobiology", Biotechnology Letters **36**, 657–665 (2014) (cited on page 81).

[139] Y. Shao, X. Tan, R. Novitski, M. Muqaddam, P. List, L. Williamson, J. Fu, and A. P. Liu, "Uniaxial cell stretching device for livecell imaging of mechanosensitive cellular functions", Review of Scientific Instruments **84**, 114304 (2013) (cited on page 81).

[140] S. Jungbauer, H. Gao, J. P. Spatz, and R. Kemkemer, "Two Characteristic Regimes in Frequency-Dependent Dynamic Reorientation of Fibroblasts on Cyclically Stretched Substrates", Biophysical Journal **95**, 3470–3478 (2008) (cited on page 81).

[141] U. Faust, N. Hampe, W. Rubner, N. Kirchgessner, S. Safran, B. Hoffmann, and R. Merkel, "Cyclic Stress at mHz Frequencies Aligns Fibroblasts in Direction of Zero Strain", PloS One **6**, e28963 (2011) (cited on page 81).

[142] I. Sraj, C. D. Eggleton, R. Jimenez, E. Hoover, J. Squier, J. Chichester, and D. W. M. Marr, "Cell deformation cytometry using diode-bar optical stretchers", Journal of Biomedical Optics **15**, 047010 (2010) (cited on page 81).

[143] D. Mitrossilis, J. Fouchard, A. Guiroy, N. Desprat, N. Rodriguez, B. Fabry, and A. Asnacios, "Single-cell response to stiffness exhibits muscle-like behavior", Proceedings of the National Academy of Sciences **106**, 18243–18248 (2009) (cited on page 81).

[144] O. Thoumine and A. Ott, "Time scale dependent viscoelastic and contractile regimes in fibroblasts probed by microplate manipulation", Journal of Cell Science **110**, 2109–2116 (1997) (cited on page 81).

[145] K. D. Webster, W. P. Ng, and D. A. Fletcher, "Tensional Homeostasis in Single Fibroblasts", Biophysical Journal **107**, 146–155 (2014) (cited on pages 82, 99, 102, 117).

[146] A. C. Scheiwe, S. C. Frank, T. J. Autenrieth, M. Bastmeyer, and M. Wegener, "Subcellular stretch-induced cytoskeletal response of single fibroblasts within 3D designer scaffolds", Biomaterials **44**, 186–194 (2015) (cited on page 82).

[147] D. Desmaële, M. Boukallel, and S. Régnier, "Actuation means for the mechanical stimulation of living cells via microelectromechanical systems: A critical review", Journal of Biomechanics **44**, 1433–1446 (2011) (cited on page 82).

[148] T. D. Brown, "Techniques for mechanical stimulation of cells in vitro: a review", Journal of Biomechanics **33**, 3–14 (2000) (cited on page 82).

[149] H. Kamble, M. J. Barton, M. Jun, S. Park, and N.-T. Nguyen, "Cell stretching devices as research tools: engineering and biological considerations", Lab on a Chip **16**, 3193–3203 (2016) (cited on page 82).

[150] E. D. Lemma, B. Spagnolo, M. de Vittorio, and F. Pisanello, "Studying Cell Mechanobiology in 3D: The Two-Photon Lithography Approach", Trends in Biotechnology **37**, 358–372 (2019) (cited on page 82).

[151] F. Klein, B. Richter, T. Striebel, C. M. Franz, G. von Freymann, M. Wegener, and M. Bastmeyer, "Two-Component Polymer Scaffolds for Controlled Three-Dimensional Cell Culture", Advanced Materials **23**, 1341–1345 (2011) (cited on page 82).

[152] P. Tayalia, C. R. Mendonca, T. Baldacchini, D. J. Mooney, and E. Mazur, "3D Cell-Migration Studies using Two-Photon Engineered Polymer Scaffolds", Advanced Materials **20**, 4494–4498 (2008) (cited on page 82).

[153] D. Ricci, M. Nava, T. Zandrini, G. Cerullo, M. Raimondi, and R. Osellame, "Scaling-Up Techniques for the Nanofabrication of Cell Culture Substrates via Two-Photon Polymerization for Industrial-Scale Expansion of Stem Cells", Materials **10**, 66 (2017) (cited on page 82).

[154] B. Richter, V. Hahn, S. Bertels, T. K. Claus, M. Wegener, G. Delaittre, C. Barner-Kowollik, and M. Bastmeyer, "Guiding Cell Attachment in 3D Microscaffolds Selectively Functionalized with Two Distinct Adhesion Proteins", Advanced Materials **29**, 1604342 (2017) (cited on page 82).

[155] T. Okano, N. Yamada, M. Okuhara, H. Sakai, and Y. Sakurai, "Mechanism of cell detachment from temperature-modulated, hydrophilic-hydrophobic polymer surfaces", Biomaterials **16**, 297–303 (1995) (cited on page 82).

[156] V. Frank, S. Kaufmann, R. Wright, P. Horn, H. Y. Yoshikawa, P. Wuchter, J. Madsen, A. L. Lewis, S. P. Armes, A. D. Ho, and M. Tanaka, "Frequent mechanical stress suppresses proliferation of mesenchymal stem cells from human bone marrow without loss of multipotency", Scientific Reports **6**, 24264 (2016) (cited on page 82).

[157] M. Guvendiren and J. A. Burdick, "Stiffening hydrogels to probe short- and long-term cellular responses to dynamic mechanics", Nature Communications **3**, 792 (2012) (cited on page 82).

[158] C. Yang, M. W. Tibbitt, L. Basta, and K. S. Anseth, "Mechanical memory and dosing influence stem cell fate", Nature Materials **13**, 645–652 (2014) (cited on page 82).

[159] D. Kulms and T. Schwarz, "Molecular Mechanisms of UV-Induced Apoptosis", Photodermatology, Photoimmunology & Photomedicine **16**, 195–201 (2000) (cited on page 82).

[160] Y. Takashima, S. Hatanaka, M. Otsubo, M. Nakahata, T. Kakuta, A. Hashidzume, H. Yamaguchi, and A. Harada, "Expansion–contraction of photoresponsive artificial muscle regulated by host–guest interactions", Nature Communications **3**, 1270 (2012) (cited on page 82).

[161] A. Harada, Y. Takashima, and M. Nakahata, "Supramolecular Polymeric Materials via Cyclodextrin-Guest Interactions", Accounts of Chemical Research **47**, 2128–2140 (2014) (cited on page 82).

[162] B. V. K. J. Schmidt and C. Barner-Kowollik, "Dynamic Macromolecular Material Design - The Versatility of Cyclodextrin-Based Host-Guest Chemistry", Angewandte Chemie International Edition **56**, 8350–8369 (2017) (cited on page 82).

[163] M. Hörning, M. Nakahata, P. Linke, A. Yamamoto, M. Veschgini, S. Kaufmann, Y. Takashima, A. Harada, and M. Tanaka, "Dynamic Mechano-Regulation of Myoblast Cells on Supramolecular Hydrogels Cross-Linked by Reversible Host-Guest Interactions", Scientific Reports **7**, 7660 (2017) (cited on pages 82, 87, 89).

[164] M. V. Rekharsky and Y. Inoue, "Complexation Thermodynamics of Cyclodextrins", Chemical Reviews **98**, 1875–1918 (1998) (cited on page 83).

[165] C. L. D. Gibb, E. E. Oertling, S. Velaga, and B. C. Gibb, "Thermodynamic Profiles of Salt Effects on a Host-Guest System: New Insight into the Hofmeister Effect", The Journal of Physical Chemistry B **119**, 5624–5638 (2015) (cited on page 85).

[166] M. Ghibaudo, A. Saez, L. Trichet, A. Xayaphoummine, J. Browaeys, P. Silberzan, A. Buguin, and B. Ladoux, "Traction forces and rigidity sensing regulate cell functions", Soft Matter **4**, 1836 (2008) (cited on page 87).

[167] John L. Tan, Joe Tien, Dana M. Pirone, Darren S. Gray, Kiran Bhadriraju, and Christopher S. Chen, "Cells lying on a bed of microneedles: An approach to isolate mechanical force", Proceedings of the National Academy of Sciences **100**, 1484–1489 (2003) (cited on pages 97, 98).

[168] N. Q. Balaban, U. S. Schwarz, D. Riveline, P. Goichberg, G. Tzur, I. Sabanay, D. Mahalu, S. Safran, A. Bershadsky, L. Addadi, and B. Geiger, "Force and focal adhesion assembly: a close relationship studied using elastic micropatterned substrates", Nature Cell Biology **3**, 466–472 (2001) (cited on pages 97, 98).

[169] J. R. D. Soiné, C. A. Brand, J. Stricker, P. W. Oakes, M. L. Gardel, and U. S. Schwarz, "Model-based traction force microscopy reveals differential tension in cellular actin bundles", PLOS Computational Biology **11**, e1004076 (2015) (cited on page 98).

[170] C. A. Brand, M. Linke, K. Weißenbruch, B. Richter, M. Bastmeyer, and U. S. Schwarz, "Tension and Elasticity Contribute to Fibroblast Cell Shape in Three Dimensions", Biophysical Journal **113**, 770–774 (2017) (cited on pages 98, 99).

[171] R. A. Brown, R. Prajapati, D. A. McGrouther, I. V. Yannas, and M. Eastwood, "Tensional Homeostasis in Dermal Fibroblasts: Mechanical Responses to Mechanical Loading in Three-Dimensional Substrates", Journal of Cellular Physiology **175**, 323–332 (1998) (cited on pages 102, 116).

[172] T. Mizutani, H. Haga, and K. Kawabata, "Cellular Stiffness Response to External Deformation: Tensional Homeostasis in a Single Fibroblas", Cell Motility and the Cytoskeleton **59**, 242–248 (2004) (cited on page 102).

[173] Daniel G. Ezra, James S. Ellis, Michèle Beaconsfield, Richard Collin, and and Maryse Bailly, "Changes in Fibroblast Mechanostat Set Point and Mechanosensitivity: An Adaptive Response to Mechanical Stress in Floppy Eyelid Syndrome", Investigative Ophthalmology & Visual Science **51**, 3853–3863 (2010) (cited on pages 102, 117).

[174] J. M. Belmonte, M. Leptin, and F. Nédélec, "A theory that predicts behaviors of disordered cytoskeletal networks", Molecular Systems Biology **13**, 941 (2017) (cited on pages 107, 118).

[175] M. Amano, M. Nakayama, and K. Kaibuchi, "Rho-Kinase/ROCK: A Key Regulator of the Cytoskeleton and Cell Polarity", Cytoskeleton **67**, 545–554 (2010) (cited on page 107).

[176] K. Kimura, M. Ito, M. Amano, K. Chihara, Y. Fukata, M. Nakafuku, B. Yamamori, J. Feng, T. Nakano, K. Okawa, A. Iwamatsu, and K. Kaibuchi, "Regulation of Myosin Phosphatase by Rho and Rho-Associated Kinase (Rho-Kinase)", Science **273**, 245–248 (1996) (cited on page 107).

[177] J. Shao, W. J. Welch, N. A. DiProspero, and M. I. Diamond, "Phosphorylation of Profilin by ROCK1 Regulates Polyglutamine Aggregation", Molecular and Cellular Biology **28**, 5196–5208 (2008) (cited on page 107).

[178] M. S. Shutova, S. B. Asokan, S. Talwar, R. K. Assoian, J. E. Bear, and T. M. Svitkina, "Self-sorting of nonmuscle myosins IIA and IIB polarizes the cytoskeleton and modulates cell motility", Journal of Cell Biology **216**, 2877–2889 (2017) (cited on page 116).

[179] K. A. Beningo, K. Hamao, M. Dembo, Y.-l. Wang, and H. Hosoya, "raction Forces of Fibroblasts are Regulated by the Rho- Dependent Kinase but not by the Myosin Light Chain Kinase", Archives of Biochemistry and Biophysics **456**, 224–231 (2006) (cited on page 116).

[180] A. J. Banes, M. Tsuzaki, J. Yamamoto, T. Fischer, B. Brigman, T. Brown, and L. Miller, "Mechanoreception at the cellular level: the detection, interpretation, and diversity of responses to mechanical signals", Biochemistry and Cell Biology **73**, 349–365 (1995) (cited on page 116).

[181] S. Weng, Y. Shao, W. Chen, and J. Fu, "Mechanosensitive subcellular rheostasis drives emergent single-cell mechanical homeostasis", Nature Materials **15**, 961–967 (2016) (cited on page 117).

[182] C. Veigel, J. E. Molloy, S. Schmitz, and J. Kendrick-Jones, "Load-dependent kinetics of force production by smooth muscle myosin measured with optical tweezers", Nature Cell Biology **5**, 980–986 (2003) (cited on page 117).

[183] N. Hundt, W. Steffen, S. Pathan-Chhatbar, M. H. Taft, and D. J. Manstein, "Load-dependent modulation of non-muscle myosin-2A function by tropomyosin 4.2", Scientific Reports **6**, 20554 (2016) (cited on page 117).

[184] A. Livne and B. Geiger, "The inner workings of stress fibers - from contractile machinery to focal adhesions and back", Journal of Cell Science **129**, 1293–1304 (2016) (cited on page 118).

[185] K. Burridge and E. S. Wittchen, "The tension mounts: Stress fibers as force-generating mechanotransducers", Journal of Cell Biology **200**, 9–19 (2013) (cited on page 118).

Acknowledgments

At this point, it is my pleasure to thank all the people that have contributed in various ways to this thesis and supported me along the way.

First of all, I would like to thank Prof. Dr. Martin Wegener and Prof. Dr. Martin Bastmeyer for the opportunity to work on this fascinating topic. I am very thankful for their excellent guidance and input, as well as the freedom to develop and realize my own ideas. Working on challenges in this interdisciplinary research field has broadened my view and I learned a lot during this time.

As a physicist working between physics and biology, I am very grateful to Dr. Kai Weißenbruch for all the biological questions he answered and the time and ideas he has invested in our project. I have always enjoyed the discussions and work together. Here, I would also like to thank Kai Richler, who took over the cell culture at an important time and helped me to continue the experiments.

This work would not have been possible without excellent collaboration partners in chemistry. In this context, I would like to particularly highlight Dr. Eva Blasco who substantially contributed to all of my projects and shared countless discussions with me. I am also grateful to Prof. Dr. Christopher Barner-Kowollik and Prof. Dr. Motomu Tanaka who provided valuable input along the way of my thesis. I also want to thank my collaborators in Japan, including Prof. Dr. Akira Harada, Prof. Dr. Yoshinori Takashima, and Dr. Masaki Nakahata who synthesized and provided the host-guest materials and shared their knowledge about the system. The working atmosphere in this collaboration was always supportive and constructive.

I would like to thank all my former and present colleagues of both, the Wegener and the Bastmeyer group. It was great experience to work in this extraordinary inspiring, supportive and helpful environment. I want to specifically mention Dr. Benjamin Richter, whose related work provided the foundation for the projects in my thesis. I also want to acknowledge Vincent Hahn for taking scanning electron micrographs of my samples and Tobias Frenzel and Dr. Jingyuan Qu for their help with the numerical calculations.

I am also very thankful for all those who have worked in the background. I would like to especially thank our technician Johann Westhauser as well as Werner Gilde, Michael Hippe, and Helmuth Lay from the electronic workshop. Furthermore, I am grateful to the staff of the mechanical workshop as well as to the secretaries and to the administrative staff of the Institute of Applied Physics, the Zoological Institute, and the Nanostructure Service Laboratory.

I would also like to thank the Karlsruhe School of Optics and Photonics for financial support with a scholarship and the Cluster of Excellence 3D Matter Made to Order. Both graduate schools offered an interesting, interdisciplinary research environment with many opportunities to learn new skills and make new contacts.

I also thank all the readers who helped me to minimize the number of errors in my thesis and asked critical questions: Pascal Kiefer, Frederik Mayer, Dr. Kai Weißenbruch, Tobias Messer, Julian Köpfler, Vincent Hahn, Alexander Münchinger, Regina Hippler, Dr. Eva Blasco, Dr. Sarah Bertels, and Dr. Enrico Lemma,

Finally, I would like thank my family who has supported me throughout the years. Most of all, I thank my wonderful wife Regina, who is always there for me, and my son Lukas, who quickly manages to divert my thoughts from work once I come home. I am very fortunate to have them in my life.